

**DETERMINATION OF REGIONAL SCALE CROP COEFFICIENTS FOR CROP  
WATER REQUIREMENT CALCULATIONS:  
A REMOTE SENSING PERSPECTIVE**

(A Case Study of the Lake Naivasha Basin, Kenya)

**Mekonnen Gebremichael Woldemariam**

**April, 1999**

**DETERMINATION OF REGIONAL SCALE CROP COEFFICIENTS FOR CROP  
WATER REQUIREMENT CALCULATIONS:  
A REMOTE SENSING PERSPECTIVE**

(A Case Study of the Lake Naivasha Basin, Kenya)

By

**Mekonnen Gebremichael Woldemariam**

Thesis submitted to the International Institute for Aerospace Survey and Earth Sciences in partial fulfilment of the requirements for the degree of Master of Science in Water Resources Surveys with emphasis on Watershed Management.

**Examination Board:**

Prof. Dr. A.M.J. Meijerink (chairman of the examination board, and supervisor)

Dr. H.A.R. de Bruin (external examiner)

Dr. W.G.M. Bastiaanssen (supervisor)

Ir. J.A.M. de Brouwer (director of studies)



**INTERNATIONAL INSTITUTE FOR AEROSPACE SURVEY AND EARTH SCIENCES**

**ENSCHEDA, THE NETHERLANDS**

**This thesis is dedicated to the two persons I love most on earth:**

**My father, Ato GEBREMICHAEL WOLDEMARIAM, and**

**My mother, Woizero LETEBERHAN AREGAWI**

## **Acknowledgements**

I wish to express my gratitude to the Commission for Sustainable Agriculture and Environmental Rehabilitation in Tigray, and the Netherlands Government for granting me the opportunity to pursue this course of study.

I am very grateful to my supervisor, Prof. Dr. A.M.J. Meijerink, for his kind guidance and support throughout the study period.

I feel deeply indebted to my supervisor, Dr. W.G.M. Bastiaanssen, who initiated this study and guided me through the various stages of the study period. His continuing support and stimulating enthusiasm, and critical comments have been and still are of great importance to me.

I also owe much to my supervisor, Ir. A.M. van Lieshout, for his assistance and encouragement during the entire course work and thesis preparatory period. My special thanks are extended to Dr. A.G. Gieske for his critical review of the manuscript; and the entire staff of the division of water resources survey in ITC for their lectures and cooperation. Thanks are also addressed to the WRAP (Water Resources Assessment Project) and KNWTP (Kenya Netherlands Wetlands Training Programme) personnel for their fruitful help in data collection and logistics provision.

I am forever grateful to my beloved parents, Ato Gebremichael Woldemariam and W/o Leteberhan Aregawi, who taught me the principles of life. My parents have always been the constant source of my strength and hope in every aspect of life. Their continuing guidance, caring support, and deep love is greatly appreciated. My special heartfelt gratitude also goes to my sisters, Alemtsehay, Meaza, Sara, Helen, Bethelhem, Selamawit, Zufan, and my brothers, Yemane and Mesfin, for their warm affection and continuous encouragement.

I would like to take this opportunity to express my sincere thanks to my best colleagues, Fekadu Kassa, Zemichael Kidanemariam, and Kidane Yitbarek, for their precious friendship and kind help. In fact, they have shown me that friendship is not just another word.

The company of my classmates, particularly Mrs. Zhenxu (China) and Mr. Behar (Ethiopia), is appreciated. I also wish to thank the ITC Christian fellowship for providing an environment for spiritual growth.

But above all, praise be to God for His wonderful Grace without which nothing is possible.

## Abstract

Since the publication of FAO booklets in the late seventies (Doorenbos and Pruitt, 1977), the calculation of crop potential evapotranspiration ( $ET_c$ ) through a combination of reference evapotranspiration ( $ET_{ref}$ ) with appropriate crop coefficients ( $K_c$ ) has become increasingly popular among practicing irrigation engineers and water managers. This study investigates the application of satellite data to obtain regional scale  $K_c$  analytically without the prior knowledge of crop type and stage of growth.

During approximately 10 days, a field campaign was held in the Lake Naivasha Vineyard Farm, Kenya to collect data on surface energy variables. Using the relevant field data,  $ET_c$  values have been calculated using an energy balance residual- and Priestley Taylor equations in Squash, Bean, and Chilli fields. The latter equation, with the Priestley-Taylor  $\alpha$  parameter = 1.26, has yielded  $ET_c$  values that are compatible with those obtained using the former equation. An empirical equation has also been developed to calculate  $ET_c$  using only incoming solar radiation and surface temperature data.  $ET_{ref}$  can be calculated using the same Priestley-Taylor equation, with surface albedo = 0.23.

By taking the quotient between Priestley-Taylor equations for  $ET_c$  and  $ET_{ref}$ , the formulation for  $K_c$  is stated, both on instantaneous and daily temporal scales. Attempts are also made to further simplify  $K_c$  input parameters.  $K_c$  values calculated using the  $K_c$  equation are compared to those derived from the FAO Table.

The  $K_c$  equations are then applied to satellite data. The resulting  $K_c$  and  $ET_c$  maps, based on the LANDSAT-TM data, are displayed. For small scale irrigated areas, like that of the study area, the spatial resolution of NOAA-AVHRR imagery is found to be unsuitable for the calculation of  $K_c$  using the derived equations. However, the procedure which ought to be followed while applying the derived  $K_c$  equations to NOAA-AVHRR data acquired over large-scale irrigated areas is outlined.

## List of Abbreviations and Symbols

Symbols which are not frequently encountered are defined in the text only. Whenever symbols take units different from those mentioned in this list, the new units are stated in the text.

### Abbreviations

---

ET	EvapoTranspiration
ET <sub>c</sub>	Crop Potential EvapoTranspiration
ET <sub>ref</sub>	Grass reference EvapoTranspiration
P-T	Priestley Taylor
E-R	Energy Balance Residual
FAO	Food and Agricultural Organization
LAI	Leaf Area Index
NIR	Near Infrared Radiation
NDVI	Normalized Difference Vegetation Index
PVI	Perpendicular Vegetation Index
SAVI	Soil Adjusted Vegetation Index
LANDSAT	LAND remote sensing SATellite
TM	Thematic Mapper
AVHRR	A Very High Resolution Radiometer
NOAA	National Oceanic and Atmospheric Administration

Symbol (General)	Description	Units
------------------	-------------	-------

K <sub>c</sub>	Crop Coefficient	[-]
λE or LE	Latent heat flux	[W m <sup>-2</sup> ]
H	Sensible heat flux	[W m <sup>-2</sup> ]
G	Soil heat flux	[W m <sup>-2</sup> ]
α	The Priestley-Taylor coefficient	[-]
n	Bright sunshine hours in a day	[hours]
N	Total daytime hours in a day	[hours]
R <sup>2</sup>	Coefficient of regression	[-]
R <sub>o</sub> <sup>2</sup>	Coefficient of determination	[-]
E	Efficiency factor	[-]
t	Calculated t-statistic value	[-]
t-critical	Critical t-statistic value	[-]
Z	Number of data pairs	[-]
∇	Level of significance	[-]
a	Slope of regression line forced to pass through origin	[-]
V <sub>c</sub>	Fractional vegetation cover	[-]
A	Land surface altitude	[km]

Symbol (Radiation)	Description	Units
--------------------	-------------	-------

$R_n$	Net radiation flux	$[W m^{-2}]$
$K_{\downarrow}^{TOA}$	Incoming extraterrestrial shortwave radiation flux	$[W m^{-2}]$
$K_{\downarrow}$	Incoming shortwave radiation flux	$[W m^{-2}]$
$L_{\downarrow}$	Incoming longwave radiation flux	$[W m^{-2}]$
$K_{\uparrow}$	Outgoing shortwave radiation flux	$[W m^{-2}]$
$L_{\uparrow}$	Outgoing longwave radiation flux	$[W m^{-2}]$
$K_n$	Net shortwave radiation	$[W m^{-2}]$
$L_n$	Net longwave radiation	$[W m^{-2}]$
$R_{n24}$	Net radiation flux per day	$[W m^{-2}]$
$K_{\downarrow 24}$	Incoming shortwave radiation flux per day	$[W m^{-2}]$
$K_{\downarrow 24}^{TOA}$	Incoming extraterrestrial shortwave radiation per day	$[W m^{-2}]$
$L_{n24}$	Net longwave radiation flux per day	$[W m^{-2}]$
$\tau'_{sw}$	Single-way transmittance in the shortwave range	[-]
$\tau''_{sw}$	Two-way transmittance in the shortwave range	[-]
$\tau'_{sw24}$	Single-way daily transmittance in the shortwave range	[-]
$\tau_6$	Single-way transmittance in the longwave range	[-]
$T_o$	Surface temperature	[K]
$T_a$	Air temperature at reference height	[K]
$T_{mean}$	Mean daily air temperature	[K]
$T_{max}$	Maximum daily air temperature	[K]
$T_{min}$	Minimum daily air temperature	[K]
$\alpha_o$	Daily surface albedo	[-]
$\alpha_{inst}$	Instantaneous surface albedo	[-]
$\epsilon_o$	Surface broadband emissivity	[-]
$\epsilon'$	Net broadband emissivity between atmosphere and surface	[-]
$\epsilon_a$	Atmosphere broadband emissivity	[-]
$\sigma$	Stefan-Boltzmann Constant ( $5.67 \cdot 10^{-8}$ )	$[W m^{-2} K^{-4}]$
EF	Evaporative fraction	[-]
$I_{sc}$	The solar constant (1367)	$[W m^{-2}]$
$\Gamma$	Day angle	[rad]
$E_o$	Eccentricity	[-]
$\omega$	Hour angle	[rad]
H	Altitude of satellite	[km]
R	Radius of earth (6370)	[km]

### Symbol (Meteorological) Description

### Units

$\lambda_v$	Latent heat of vaporization	$[MJ kg^{-1}]$
$P_a$	Atmospheric vapor pressure	[k Pa]
$\rho_a$	Density of air	$[Kg m^{-3}]$
$c_p$	Specific heat of air at constant pressure	$[J kg^{-1} K^{-1}]$
d	Zero plane displacement	[m]
k	Von Karman's constant (0.41)	[-]
$e_a$	Atmospheric water vapor pressure at reference height	[k Pa]
$e_{a,sat}$	Saturation vapor pressure of air at reference height	[k Pa]
$e_{o,sat}$	Saturation vapor pressure near surface	[k Pa]

D	Vapor pressure deficit at reference height ( $e_{a,sat} - e_a$ )	[k Pa]
RH	Relative humidity	[%]
$r_{ah}$	Aerodynamic resistance to heat transport	[s m <sup>-1</sup> ]
$r_{av}$	Aerodynamic resistance to water vapor transport	[s m <sup>-1</sup> ]
$r_a$	Aerodynamic resistance ( $r_{ah} \approx r_{av}$ )	[s m <sup>-1</sup> ]
$\Delta$	Slope of saturation vapor pressure	[k Pa °C <sup>-1</sup> ]
u	Wind speed at reference height	[m s <sup>-1</sup> ]
$Z_{oh}$	Roughness length for heat transport	[m]
$Z_{om}$	Roughness length for momentum transport	[m]
$\gamma$	Psychrometric constant	[k Pa °C <sup>-1</sup> ]
$\Psi_m$	Intergrated stability function for momentum transfer	[-]
$\Psi_h$	Intergrated stability function for heat transfer	[-]
d	Displacement height	[m]
Z	Reference height (1.75)	[m]

<b>Symbol (Soil) Description</b>		<b>Units</b>
d	Soil depth	[cm]
$\theta_d$	Soil moisture content (by volume) at depth d	[%]

<b>Symbol (Plant) Description</b>		<b>Units</b>
$r_s$	Stomatal resistance	[s m <sup>-1</sup> ]
h	Crop height	[m]

<b>Symbol (Geometry) Description</b>		<b>Units</b>
$\theta_z$	Solar zenith angle, incidence angle on a horizontal plane	[deg]
$\phi_z$	Satellite zenith angle	[deg]
$\phi_{view}$	Off-nadir angle	[deg]

## Table of Contents

<b>Acknowledgements.....</b>	<b>iv</b>
<b>Abstract.....</b>	<b>v</b>
<b>List of Abbreviations and Symbols.....</b>	<b>vi</b>
<b>1 Introduction.....</b>	<b>1</b>
1.1 General Problem Definition.....	1
1.2 Objectives.....	1
1.3 General Approach.....	2
1.4 Outline of the Thesis.....	2
<b>2 Theoretical Background.....</b>	<b>3</b>
2.1 Definitions.....	3
2.2 Literature Review of Crop Coefficients.....	3
2.3 Analytical Solution of $K_c$ .....	4
2.3.1 Grass Reference Evapotranspiration ( $ET_{ref}$ ).....	5
2.3.2 Crop Potential Evapotranspiration ( $ET_c$ ).....	6
<b>3 Description of Field Measurements.....</b>	<b>10</b>
3.1 Introduction.....	10
3.2 The Study Area.....	10
3.3 Lake Naivasha Vineyard Data Set.....	12
3.3.1 Site Description.....	12
3.3.2 Field Measurements and Data.....	14
3.4 The Ndabibi Data Set.....	15
<b>4 Calibration and Validation of Evapotranspiration equations, using field data.....</b>	<b>17</b>
4.1 Introduction.....	17
4.2 Instantaneous Time Scale.....	17
4.2.1 Crop Potential Evapotranspiration ( $ET_c$ ) Equations.....	17
4.2.2 Grass Reference Evapotranspiration ( $ET_{ref}$ ) Equations.....	23
4.2.3 Validated $K_c$ Equation, on an instantaneous time scale.....	23
4.3 Daily Time Scale.....	24
4.4 Testing Parameterizations of $K_c$ parameters.....	24
4.4.1 Instantaneous Time Scale.....	25
4.4.2 Daily Time Scale.....	26
4.5 Comparison of $K_c$ values estimated using the validated $K_c$ equation and FAO $K_c$ Table.....	28
4.6 Conditions under which the validated $K_c$ and $ET_c$ equations are expected to work.....	29
4.7 Sensitivity Analysis of $K_c$ Parameters, on a daily scale.....	29
4.8 Comparison of $ET_{ref}$ Equations: P-T vs. Simplified Empirical Equations.....	31

<b>5</b>	<b>LANDSAT-TM and NOAA-AVHRR Applications.....</b>	<b>33</b>
5.1	LANDSAT-TM Application.....	33
5.1.1	Data Acquisition.....	33
5.1.2	Delineating Irrigated Areas.....	33
5.1.3	Estimating $K_c$ and $ET_c$ Parameters, on an instantaneous time scale	34
5.1.4	Estimating $K_c$ and $ET_c$ Parameters, on a daily time scale.....	42
5.1.5	Comparison of Instantaneous and Daily Estimates.....	43
5.2	NOAA-AVHRR Application.....	45
5.2.1	Introduction.....	45
5.2.2	Proportion of Irrigated Areas within the Pixel Size of NOAA-AVHRR.....	46
5.2.3	NOAA-AVHRR Application to Large Scale Irrigation Schemes...	48
<b>6</b>	<b>Conclusions and Recommendations.....</b>	<b>53</b>
	<b>References.....</b>	<b>55</b>

## Annexes

A	Statistical Methods used for Assessing Association.....	61
B	Derivation of a Simplified Empirical Equation for Estimating Crop Potential Evapotranspiration.....	62
C	Testing Transmittance Models.....	64
D	Derivation of an Empirical Equation for Estimating Daily Net Longwave Radiation.....	66
E	Extraterrestrial Solar Radiation.....	67
F	LANDSAT-TM Image Preprocessing.....	69
F.1	Characteristics of the LANDSAT System.....	69
F.2	Radiometric Correction.....	69
F.3	Atmospheric Correction, Visible and Infrared.....	70
G	NOAA-AVHRR Image Preprocessing.....	72
G.1	Characteristics of the NOAA System.....	72
G.2	AVHRR Data.....	72
G.3	Cloud Detection.....	73
G.4	Atmospheric Correction, Visible and Near Infrared.....	76
H	Temporal Variability and Interrelationships between Variables.....	79
H.1	Temporal Variation of Micro-meteorological Variables.....	79
H.2	Soil Moisture Profile.....	80
H.3	Empirical Relationships between Soil Moisture and Land surface Properties.....	81
I	Openfield vs. Greenhouse.....	84
J	File Locations.....	86
K	Field Data.....	89

## Table of Figures

Fig. 3.1	The study area in international, national, and regional contexts. ....	10
Fig. 3.2	Mean monthly values of meteorological observations for the Lake Naivasha area .....	11
Fig. 3.3	Schematic Plan view of the study sites. ....	13
Fig. 3.4	Comparison of incoming solar radiation ( $K_{\downarrow}$ or $K_{inc.}$ ) and the difference between maximum- and minimum daily air temperature ( $T_{max} - T_{min}$ ) trends. ....	15
Fig. 3.5	Cumulative histogram plots for daily averages of (a) $K_{inc.}$ ( $K_{\downarrow}$ ), (b) $T_a$ , and (c) RH. ....	16
Fig. 4.1	Comparison of instantaneous $ET_c$ estimated using Energy balance Residual and Priestley- Taylor .....	20
Fig. 4.2	Comparison of net longwave radiation measured on site and estimated using the Slob's approach. ....	25
Fig. 4.3	Comparison of atmospheric emissivity estimated using Stefan-Boltzmann equation and (a) Idso-Jackson, and (b) Swinbank equations. ....	26
Fig. 4.4	(a) Comparison of $\epsilon'$ estimated using Eqs.(4.30) and (4.31), and (b) Scattergram between $L_{n24}$ estimates made by Eqs. (4.29) and (4.32). ....	27
Fig. 4.5	Comparison between $ET_{ref}$ estimates made using the Priestley-Taylor (P-T) and (a) Modified Makkink (b) Jensen-Haise, (c) Turc, and (d) Hargreaves equations. ....	32
Fig. 4.6	Comparison between $ET_{ref}$ estimates made using P-T and Eq. (4.45) .....	32
Fig. 5.1	Spectral feature space of multibands .....	33
Fig. 5.2	A False color composite image corresponding to the study area. ....	35
Fig. 5.3	Map showing the irrigated areas .....	35
Fig. 5.4	Crop coefficient ( $K_c$ ) map corresponding to the 9:45 hour local time of 21 January 1995. ....	40
Fig. 5.5	Crop potential evapotranspiration ( $ET_c$ ) map corresponding to the LANDSAT-TM data acquired at 9:45 hour local time of 21 January 1995. ....	40
Fig. 5.6	Histogram of $K_c$ on an instantaneous time scale, based on the LANDSAT-TM data of 9: 45 hour local time of 21 January 1995. ....	41
Fig. 5.7	Comparison of $\tau'_{sw}$ at 9:45 and $\tau'_{sw24}$ .....	42
Fig. 5.8	Crop coefficient ( $K_c$ ) map on a daily scale .....	44
Fig. 5.9	Crop potential evapotranspiration for 21 January 1995 .....	44
Fig. 5.10	Daytime variation of transmittance, for average condition of May. ....	50
Fig. B.1	Comparison of instantaneous $ET_c$ estimates made by Energy balance Residual equation and Eq. (B.4) over (a) Squash, (b) Bean, and (c) Chilli fields. ....	63
Fig. C.1	Comparison of transmittance values calculated from Eq. (C.1) and modelled using (a) Hottel's model, and (b) Bolsenga's model. ....	64
Fig. G.1	The Saunders cloud detection algorithm. ....	74
Fig. G.2	Results of the cloud detection scheme applied on the imagery of the last decade of May 1995 .....	76
Fig. G.3	Channel 1 and channel 2 reflectances as a function of satellite zenith angle .....	79
Fig. H.1	Typical diurnal variation of (a) incoming shortwave radiation $K_{\downarrow}$ ( $K_{inc.}$ ), (b) windspeed $u$ , (c) surface radiant temperature $T_o$ , and (d) $T_o - T_a$ , measured on October 8, 1998. ....	79
Fig. H.2	Soil moisture profile at (a) Squash, (b) Bean, (c) Chilli, and (d) bare sites after little rain (expressed as percentage of volume). ....	80
Fig. H.3	Soil moisture profile at (a) Bean, and (b) Chilli sites in the absence of rain (expressed as percentage of volume). ....	81
Fig. H.4	Relations between soil surface albedo and soil moisture (expressed as percentage of volume) at (a) 1cm depth, (b) 5cm depth, and (c) integrated 16cm. ....	82
Fig. H.5	Relation between soil infrared temperature and (a) 5cm soil moisture (b) soil surface albedo. ....	82
Fig. I.1	Plan and side views of the greenhouse setup. ....	84
Fig. I.2	Comparison of incoming shortwave radiation inside and outside greenhouse .....	85

## Table of Tables

Table 2.1	Equations for computing $ET_{ref}$ .....	6
Table 2.2	Empirical equations relating $G/R_n$ to remotely sensed dependent variables .....	8
Table 2.3	A small selection of empirical equations for estimating $Z_{om}$ and $d$ .....	9
Table 3.1	Site characteristics .....	13
Table 3.2	In-situ measured hydro-meteorological parameters and instrumentation .....	14
Table 3.3	Quartile values for the distribution of some atmospheric state variables .....	16
Table 4.1	Methods of assigning values to the variables/parameters involved in $ET_c$ equations .....	18
Table 4.2	Estimated input values.....	19
Table 4.3	Proportion of land cover components, $f_i$ , within a site (in fraction).....	19
Table 4.4	Values of statistical indicators of $ET_c$ values estimated using P-T and E-R equations over different cover types.....	20
Table 4.5	Values of statistical indicators of $ET_c$ estimated using P-T and E-R equations over different cover types and under different assumptions.....	22
Table 4.6	Comparison of Eq. (4.32) against Eq. (4.29).....	28
Table 4.7	Daily $K_c$ values obtained using the validated $K_c$ equation and FAO $K_c$ Table.....	28
Table 4.8	Sensitivity of $K_c$ to various variables.....	29
Table 4.9	Values of statistical indicators of $ET_{ref}$ values estimated using P-T and other simplified equations.....	31
Table 5.1	Error matrix of classification .....	34
Table 5.2	Calculated radiation parameters for LANDSAT-TM image dated 21 Jan '95.....	37
Table 5.3	NDVI atmospheric correction coefficients .....	37
Table 5.4	Correlation ( $r$ ) between $K_c$ and other state variables.....	41
Table 5.5	Results of the confusion matrices comparing $K_c$ at 9:45 with daily value for two cases of $K_c$ class widths: (a) 0.05, and (b) 0.10 .....	45
Table 5.6	The satellite-target geometry under clear sky conditions.....	47
Table 5.7	Narrow- to broadband albedo conversion constants.....	49
Table 5.8	A summary of the statistics of the resulting surface broadband albedo values computed using different algorithms.....	49
Table 5.9	Summary of Split-Window Algorithms.....	51
Table 5.10	Summary of statistics of surface temperature, computed using various split window algorithms.....	52
Table E.1	Recommended average days for months and values of $J$ by months .....	68
Table E.2	Monthly average daily extraterrestrial radiation, $W m^{-2}$ .....	68
Table F.1	LANDSAT 5 characteristics .....	69
Table F.2	Radiance values in $mW cm^{-2} Sr^{-1}$ (for date 21 January, 1995).....	69
Table F.3	Bandwidths in micron .....	70
Table F.4	$E_{sun\lambda_i}$ values in $mW cm^{-2} Sr^{-1}$ .....	70
Table F.5	Weights of TM bands as per $E_{sun\lambda_i}$ .....	71
Table F.6	Albedos of known surfaces.....	71
Table G.1	NOAA-14 Characteristics.....	72
Table G.2	AVHRR data description .....	72
Table G.3	Parameters required for unscaling AVHRR data .....	73
Table G.4	Temperature thresholds $T_{diff}$ (K) for, Channel 4 – Channel 5, cloud Detection test at mid-latitudes (after Saunders and Kriebel, 1988).....	75
Table G.5	$Q_1$ as a function of $\Theta$ .....	80
Table G.6	Functions $g(m)$ and $Q_0(m)$ .....	77
Table G.7	Mean reflectance values before- and after atmospheric correction using the paltridge and mitchell model, in percentages .....	78
Table H.1	Soil moisture profile data ( $\Theta_d$ ) for 4 samplepoints in different landcovers.....	80
Table I.1	Site characteristics .....	84

# 1.

## Introduction

### 1.1 General Problem Definition

The quantitative estimation of crop water requirement must be accurately known for irrigation scheduling and design of irrigation infrastructure. Under unstressed crop growth conditions, the crop water requirement is defined as crop potential evapotranspiration ( $ET_c$ ). The practical estimation of  $ET_c$  frequently involves calculating a reference evapotranspiration ( $ET_{ref}$ ) and then applying suitable crop coefficients ( $K_c$ ). The practicing irrigation- or agricultural engineers, and water managers often use this approach to estimate  $ET_c$  in light of its simplicity and simple input data requirement.

In the crop-coefficient approach,  $ET_{ref}$  characterizes the influence of climatic variables on  $ET_c$ , while  $K_c$  expresses the influence of the crop. The calculation of  $ET_{ref}$  only requires meteorological data. Usually, the determination of  $K_c$  involves the knowledge of crop type and stage of growth. These values are given in Tables (e.g. *Doorenbos and Pruitt, 1977*). However, for heterogeneous regional land surfaces comprising different crops and crop development stages, it is difficult to assign appropriate  $K_c$  values from Tables. Hence, there is a need to develop a methodology to determine areally-integrated  $K_c$ , which does not require information regarding crop type and its stage of growth.

Fortunately, the spatial variability of a number of crop biophysical properties can be observed by means of satellites. Remote sensing by satellite has the advantage of repetitivity, areal integration, and pixel scale discretization. Important developments have been made in the calculation of actual evapotranspiration using satellite data. Some researchers (e.g. *Caselles and Delegido, 1987*) have also attempted to calculate  $ET_{ref}$  using satellite data. As  $K_c$  is by definition related to  $ET_c$  and  $ET_{ref}$ , if the latter two can be solved from remote sensing then regional scale  $K_c$  can be directly calculated from them. This study will investigate this new approach of calculating regional scale  $K_c$  from remote sensing.

### 1.2 Objectives

The objectives of this study are:

- To test a new methodology for determining regional scale  $K_c$  analytically from remote sensing, without the prior knowledge of crop type and its stage of growth;
- To generate regional scale  $K_c$  values for the Lake Naivasha basin.

### 1.3 General Approach

An analytical solution of regional scale crop coefficient by means of remotely sensed data is investigated. In this approach, the determination of crop coefficient requires an independent estimation of crop potential evapotranspiration and reference evapotranspiration. Proper evapotranspiration estimates can be carried out using physical models, which take into account all relevant parameters. These models require remotely sensed data and extensive ground-based data at the time of satellite overpass. However, the application of these models in the “real world” is limited in view of the fact that most of the required spatially representative ground-based data are difficult to obtain. In other words, the feasibility of remote sensing technique to determine  $K_c$  in this approach is determined by its capability to meet the demands for the calculation of  $ET_c$  and  $ET_{ref}$ . So, the general approach of this study is geared towards solving the question: *How can regional scale crop coefficient be properly estimated from remote sensing using limited ground-based data for reference evapotranspiration and crop potential evapotranspiration?*

Simple evapotranspiration equations, which utilize limited ground-based data, are available in the literature (e.g. Allen *et al.*, 1996a). However, since these equations rely on empirical relations to varying levels, they can introduce errors when they are used in environments different from those under which they were developed. Hence, field validation of these equations, prior to their application, remains imperative.

This study is executed in two phases. In the first phase, data on surface energy variables are acquired from an intensive field campaign in the Lake Naivasha area and an experimental meteorological station. These data are then used to calibrate and validate evapotranspiration equations, which mainly use remotely sensed data. In the second phase, the validated evapotranspiration equations are applied to satellite images, after which maps of regional scale  $K_c$  and  $ET_c$  are obtained.

### 1.4 Outline of the Thesis

This thesis firstly presents the theoretical basis of crop coefficients. Crop coefficients are shown to be determined by the magnitudes of crop potential evapotranspiration ( $ET_c$ ) and reference evapotranspiration ( $ET_{ref}$ ). The concepts of the latter two terms are explicitly provided. An overview of some of the methods for estimating  $ET_c$  and  $ET_{ref}$  is given (Chapter 2). In chapter 3, attention is drawn to the location of the study area and the description of the data sets used in this study.

This study concentrates on the field scale estimation of  $ET_c$  and  $ET_{ref}$ , whereby remote sensing approaches are tested and parameterized, by using field data (chapter 4). Ample attention is given to the validation of simple and adequate remote sensing approaches of estimating  $ET_c$  and  $ET_{ref}$ , both on instantaneous and daily temporal scales. The sensitivity analysis of daily  $K_c$  value to changes in different parameters is also presented. Chapter 5 addresses the application of the validated  $K_c$  and  $ET_c$  equations to LANDSAT-TM and NOAA-AVHRR data, both on instantaneous and daily temporal scales. Chapter 6 contains a brief summary of the conclusions raised in the preceding Chapters, and a short recommendation.

## 2.

### Theoretical Background

#### 2.1 Definitions

*Crop potential evapotranspiration*: the depth of water needed to meet the water loss through evapotranspiration of a disease-free crop, growing in large fields under non-restricting soil conditions including soil water and fertility and achieving full production potential under the given environment.

*Grass reference evapotranspiration*: the rate of evapotranspiration from a hypothetical reference crop with an assumed crop height of 12 cm, a fixed crop resistance of  $70 \text{ s m}^{-1}$ , and an albedo of 0.23, closely resembling the evapotranspiration from an extensive surface of a uniform height of 12 cm, actively growing, completely shading the ground and not short of water.

*Crop coefficient*: the ratio of crop potential evapotranspiration to the evapotranspiration of a reference crop, usually grass or alfalfa.

#### 2.2 Literature Review of Crop Coefficients

##### Crop coefficients

The crop coefficient ( $K_c$ ) is a traditional concept that relates the water need of a particular crop to those of a reference crop (*Doorenbos and Pruitt, 1977*). Most often  $K_c$  accounts for the combined effects of crop canopy, phenological development, and soil evaporation (*Saxton and McGuinness, 1982; Slack et al., 1996*). Because of the two widely used reference crops, alfalfa and grass, two families of  $K_c$  curves for agricultural crops have been developed over the years. Applications of  $K_c$  values should be made with caution not to mix grass-based  $K_c$ 's with an alfalfa reference and vice versa (*Allen et al., 1996*). Besides, the effect of a certain calculation methodology on  $K_c$  can be significant.

##### Conventional method – the FAO approach of determining $K_c$

The conventional method for determining grass-based  $K_c$  refers to the method used in the FAO irrigation and Drainage Papers no. 24 (*Doorenbos and Pruitt, 1977*) and no. 33 (*Doorenbos and Kassam, 1986*). In these papers, "mean"  $K_c$  values that represented "time-averaged" effects are presented. These values are shown to vary with the type of crop, its stage of growth, and the prevailing weather conditions. *Doorenbos and Kassam* (1986) pointed out that this approach allows the prediction of crop potential evapotranspiration to within 10 to 20 percent accuracy provided that reliable meteorological data from a representative agricultural environment are obtained, and the total growth period and the lengths of development stages are known. FAO experts and researchers have reviewed these values recently (*Allen et al., 1996a*). They splitted  $K_c$  into two terms: the basal crop coefficient and the coefficient for

evaporation from the surface soil layer, and by doing so they were able to provide equations of  $K_c$  on a daily basis. The required input data to solve these equations are: tabulated  $K_c$  value, mean daily wind speed, mean daily minimum relative humidity, and mean plant height during the stage of growth.

### **The Normalization method of determining $K_c$**

*Slack et al.* (1996) argue that when  $K_c$  is expressed on the basis of a time variable, like days after planting (as used in the FAO approach), this coefficient can not adequately account for the effects of climatic variability on crop growth and development. Some methods, like the growing-degree-days and the soil-thermal units, have been proposed to normalize  $K_c$  for climatic variability (*Bausch*, 1995; *Hla et al.*, 1996; *Slack et al.*, 1996).

In general, both the FAO and the Normalization methods yield  $K_c$  values that are applicable only at the local scale. Over the past few years, some methods based on the use of remotely sensed data have been developed in order to determine  $K_c$  at the regional scale.

### **Remote sensing approach of determining $K_c$**

Two categories of determining  $K_c$  can be distinguished in the remote sensing approach: (1) Extrapolation of tabulated  $K_c$  values, and (2) Analytical solution of  $K_c$ .

*Extrapolation of tabulated  $K_c$  values.* *Tanner and Jury* (1976) showed that the terms, "stage of growth" and "days after planting", in the FAO approach can be expressed by vegetation indices, which can be derived from remote sensing. Based on this idea, tabulated  $K_c$  values have been related to vegetation indices such as PVI (*Jackson et al.*, 1980; *Heilman et al.*, 1982), NDVI (*Bausch and Neale et al.*, 1987; *Neale et al.*, 1989), and SAVI (*Choudhury*, 1994; *Bausch*, 1995; *Neale et al.*, 1996). The advantage of these methods is that they express  $K_c$  independent of the time variable. However, these methods rely on spatial interpretation of tabulated and, hence, prefixed  $K_c$  values (*Bastiaanssen*, 1998).

*Analytical solution of  $K_c$ .* In this category, crop potential evapotranspiration and reference evapotranspiration are calculated using remote sensing approach, and  $K_c$  is analytically solved from the two evapotranspiration estimates. This approach deserves more attention because indications are growing that tabulated  $K_c$  values give biased crop potential evapotranspiration estimates for large areas, such as heterogeneous command areas (*Bastiaanssen*, 1998).

## **2.3 Analytical Solution of $K_c$**

The crop coefficient ( $K_c$ ) relates the water needs of a particular crop to those of a reference crop in the form of Eq. (2.1). To visualize the variables which determine  $K_c$ , both  $ET_c$  and  $ET_{ref}$  have been expressed using the Penman-Monteith equation:

$$K_c = \frac{ET_c}{ET_{ref}} = \frac{\frac{\Delta(R_{nc} - G_c) + \rho_a c_p (e_{a,satc} - e_{oc}) / r_{ac}}{\Delta + \gamma \left(1 + \frac{r_{sc}}{r_{ac}}\right)}}{\frac{\Delta(R_{nref} - G_{ref}) + \rho_a c_p (e_{a,satref} - e_{oref}) / r_{aref}}{\Delta + \gamma \left(1 + \frac{r_{sref}}{r_{aref}}\right)}} \quad [-] \quad (2.1)$$

The description of the symbols is given in the list of symbols. The additional  $c$  subscripts represent characteristic values for the actual crop and the additional  $ref$  subscripts represent the same for the reference crop.

It is evident from Eq. (2.1) that although  $K_c$  depends mainly on the crop parameters (roughness height, leaf area index, albedo, and surface resistance), it also depends to some extent on the relative proportions of climatic variables (vapor pressure deficit, and temperature difference). The analytical computation of  $K_c$  is carried out in a two-step procedure: (1) estimating  $ET_{ref}$ , and (2) estimating  $ET_c$ .

### 2.3.1 Grass Reference Evapotranspiration ( $ET_{ref}$ )

#### The Concept

Since the relevant crop parameters of the reference crop are known, differences in reference evapotranspiration are mainly attributed to differences in climatological conditions. Hence, the use of  $ET_{ref}$  permits a physically realistic characterization of the effect of the microclimate of a field on the evaporative transfer of water from the soil-plant system to the atmosphere air layers overlying the field (*Doorenbos and Pruitt, 1977; Shuttleworth, 1993*).

The widely proposed reference crops are grass and alfalfa (*Doorenbos and Pruitt, 1977; Smith et al., 1996*). However, since alfalfa is not grown in many areas of the world, practically grass is used as the major reference crop (*Wright, 1996*). *Doorenbos and Pruitt (1977)* gave a physical definition to the specific type of the reference grass, while recently a more accurate bio-physical definition was provided by the FAO experts consultation (*Smith et al., 1996*), which has been stated in Section (2.1). Henceforth, the term “reference evapotranspiration” is replaced by the term “grass reference evapotranspiration”.

#### Estimating Grass Reference Evapotranspiration

There are more than 80 methods to calculate  $ET_{ref}$  (*Molina, 1996*). The choice of the appropriate method depends on the climate data available and the precision of the crop water requirement calculation required.  $ET_{ref}$  methods can be basically categorized into four: combination-based, radiation-based, pan-based, and temperature-based. An overview of some of the equations is presented in Table 2.1.

Table 2.1 Equations for computing  $ET_{ref}$

<b>Combination-based</b>	
Shuttleworth	$\frac{0.408\Delta(R_n - G) + \gamma \frac{900}{T_a} u(e_{a,sat} - e_a)}{\Delta + \gamma(1 + 0.34u)}$
<b>Radiation-based</b>	
Priestley-Taylor	$\frac{\alpha\Delta(R_n - G)}{\Delta + \gamma}$
Modified Makkink	$\frac{\beta\Delta K_{\downarrow}}{\Delta + \gamma}$ ' $\beta$ ' $\cong$ 0.63 - 0.65
Simplified	$a(R_n - G)$ ' $a$ ' is constant for a certain environment.
Jensen-Haise	$(0.025(T_{mean}-273) + 0.08)K_{\downarrow}$
Casselles	$A T_{max} K_{\downarrow} + B K_{\downarrow} + C$ 'A', 'B', and 'C' are to be computed using meteorological data.
<b>Pan-based</b>	
FAO-24 Pan	$k_p[\text{Pan reading}]$ ' $k_p$ ' is a pan coefficient. FAO-24 provided recommended values depending on long-term average of mean relative humidity, wind speed and distance of windward side of green crop.
<b>Temperature-based</b>	
Hargreaves	$0.0023 K_{\downarrow}^{TOA} (T_{mean}-255.2) (T_{max}-T_{min})^{0.50}$

Note:- The above listed equations yield  $ET_{ref}$  in different units.

### 2.3.2 Crop Potential Evapotranspiration ( $ET_c$ )

#### The Concept

The second step in estimating  $K_c$  involves the estimation of crop potential evapotranspiration ( $ET_c$ ). Various authors have given different definitions to the term "crop potential evapotranspiration", so one has to avoid using this term without explicitly stating the definition used. For instance, *Thornthwaite* (1948) defined it as if it depends solely on the available energy, *Penman* (1948) defined it as  $ET_{ref}$ , *Jensen* (1968) defined it in relation to aerodynamically rough surfaces. In the current study, the definition given by *Doorenbos and Pruitt* (1977), as stated in Section (2.1), is adopted. Another concern about the definition of  $ET_c$  is that its magnitude is often calculated from meteorological data collected under conditions in which the actual evapotranspiration rate is less than the potential rate. However, if evapotranspiration had been occurring at the potential rate, the air temperature and humidity might have been different (*Brutsaert*, 1982).

## Estimating Crop Potential Evapotranspiration

There exist a multitude of methods for the estimation of crop potential evapotranspiration ( $ET_c$ ). Overviews of many of these methods are found in review papers or books (e.g. *Brutsaert*, 1982). Some of the well known methods are addressed briefly.

*The Penman-Monteith method.* This method, as formulated in Eq. (2.2), is a combination of the surface energy balance equation and the bulk aerodynamic equation. It is essentially the result of a one-layer vegetation approach which is known as the “big leaf” model, of which the “big leaf” has the same surface roughness and albedo as the actual crop (*De Bruin*, 1987). To this leaf, a canopy resistance or surface resistance is assigned that accounts for the fact that the water vapor has to escape from the “stomata” of the big leaf to the surrounding air. One of the difficulties in applying this method is posed by the problem of quantifying bulk surface resistance for complex canopies (*Allen et al.*, 1996a).

$$ET_c = \frac{\Delta(R_n - G) + (\rho_a c_p D) / r_a}{\Delta + \gamma(1 + r_s / r_a)} \quad [\text{W m}^{-2}] \quad (2.2)$$

*The Priestley-Taylor method.* A well-known simplification of the Penman-Monteith equation is the equation proposed by *Priestley and Taylor* (1972). They found that the evapotranspiration from well-watered surfaces is rather well described by:

$$ET_c = \alpha \frac{\Delta}{\Delta + \gamma} (R_n - G) \quad [\text{W m}^{-2}] \quad (2.3)$$

Where,  $\alpha$  is the Priestley-Taylor coefficient. Under conditions of zero advection and no boundary layer growth, the air above a free water surface of large spatial scale becomes saturated under continued evaporation, and the aerodynamic term in Eq. (2.2) vanishes, consequently  $\alpha$  becomes unity. However, the air above even very extensive wet surfaces such as the oceans hardly ever becomes saturated (*De Bruin*, 1983). An explanation for this is the entrainment of dry air at the top of the atmospheric boundary layer, which is usually at the first inversion (*De Bruin*, 1983). *Priestley and Taylor* (1972) and many others after them found that  $\alpha \cong 1.26$  (*Kim and Entekhabi*, 1997).

### Field Methods of estimating $ET_c$

Surface energy balance parameters were measured over well-irrigated areas in the field. Hence, the field methods of computing  $ET_c$  make use of surface energy elements. The following two field methods are used in the current study: Energy balance Residual, and Priestley-Taylor. The Priestley-Taylor equation has just been described in the foregoing section.

#### *The Energy Balance Residual equation*

In this method,  $ET_c$  is solved as a residual component of the energy balance equation:

$$ET_c = R_n - G - H \quad [\text{W m}^{-2}] \quad (2.4)$$

Where,  $R_n$  is net radiation,  $H$  is sensible heat flux, and  $G$  is soil heat flux. The sign convention of this equation is that  $R_n$  is considered positive when radiation is directed towards the land surface, while all the rest terms in the equation are considered positive when directed away from the land surface.

#### Net Radiation ( $R_n$ )

The net radiation ( $R_n$ ) available at the evapotranspiring surface can be described as the algebraic sum of the incoming and the outgoing radiation fluxes:

$$R_n = K_n - L_n = K_{\downarrow} - K_{\uparrow} + L_{\downarrow} - L_{\uparrow} \quad [\text{W m}^{-2}] \quad (2.5)$$

Where  $K$  and  $L$  signify solar (shortwave) radiation (0.10 - 4  $\mu\text{m}$ ) and longwave radiation (> 4  $\mu\text{m}$ ) components, respectively. The arrows indicate the flux direction ( $\downarrow$  = incoming,  $\uparrow$  = outgoing), and the subscript 'n' stands for the net difference (between incoming and outgoing). All the terms at the right hand side of Eq. (2.5) were measured in the field.

#### Soil Heat Flux ( $G$ )

The soil heat flux ( $G$ ) is defined as the product of thermal conductivity and the temperature gradient at the soil surface. Results from empirical studies have shown that the daytime ratio of  $G/R_n$  can be related to parameters that can be derived from satellite data (Table 2.1).  $G$  may be ignored for time integration longer than a day.

Table 2.2 Empirical equations relating  $G/R_n$  to remotely sensed dependent variables

Reference	$G/R_n$
Jackson et al. (1987)	$0.58 \exp^{-2.13\text{NDVI}}$
Kustas and Daughtry (1990)	$0.325 - 0.208\text{NDVI}$
Clothier et al. (1986)	$0.295 - 0.0133(\text{NIR}/\text{RED})$
Bastiaanssen and Roebeling (1993)	$T_o(0.0032(\alpha_o) + 0.0062(\alpha_o)^2)(1 - 0.98\text{NDVI}^4)/(\alpha_{\text{inst}})$
Jacobsen and Hansen (1999)	$-0.27\text{NDVI} + 0.39$

Where,  $\alpha_{\text{inst}}$  and  $\alpha_o$  are instantaneous- and daily surface albedos respectively,  $T_o$  [ $^{\circ}\text{C}$ ] is surface temperature, and NDVI is a spectral index that estimates the amount of vegetation present based on the normalized difference between near-infrared (NIR) and red (RED) reflectance:  $\text{NDVI} = (\text{NIR} - \text{RED})/(\text{NIR} + \text{RED})$ .

#### Sensible Heat Flux ( $H$ )

A standard resistance model for the transfer of sensible heat is given by:

$$H = \rho_a c_p \frac{T_o - T_a}{r_{ah}} \quad [\text{W m}^{-2}] \quad (2.6)$$

Where,  $r_{ah}$  is the resistance to the transport of heat in the air layer between the surface and the air at the reference height,  $\rho_a$  is the density of moist air, and  $c_p$  is the specific heat of dry air at a constant pressure.

$r_{ah}$  is given as (Brutsaert, 1982):

$$r_{ah} = \frac{1}{k^2 u} \left[ \ln \left( \frac{Z-d}{Z_{om}} \right) - \psi_m \right] \left[ \ln \left( \frac{Z-d}{Z_{oh}} \right) - \psi_h \right] \quad [\text{s m}^{-1}] \quad (2.7)$$

Where  $k$  ( $= 0.41$ ) is Von Karman's constant,  $Z$  is the height of the reference level above the surface,  $d$  is the displacement height,  $Z_{om}$  is the momentum roughness length,  $Z_{oh}$  is the heat roughness length,  $\psi_m$  is the stability correction function for the momentum transfer, and  $\psi_h$  is the stability correction function for the heat transfer.  $Z_{om}$  and  $d$  can be computed from windspeed profile measurements, or when such data are lacking, they can be estimated using the empirical equations given in Table 2.2.

Table 2.3 A small selection of empirical equations for estimating  $Z_{om}$  and  $d$

Equations	Reference
$Z_{om} = 0.123 h$ $d = 0.67 h$	Shuttleworth (1993)
$Z_{om} = 0.20 h$	Pereira et al. (1996)
$Z_{om} = 0.14 h$	Brutsaert (1982)
$Z_{om} = \exp(0.1021+0.1484(\text{NIR/RED}))$	Moran (1990)
$Z_{om} = -0.173 + 1.168 \text{ NDVI} - 1.125 \text{ NDVI}^2$ , if $\text{NDVI} < 0.6$ $Z_{om} = 0.1$ , if $\text{NDVI} > 0.6$ $d = -0.015 + 0.029 (\text{NIR/RED})$	Hatfield (1988)
$Z_{om} = h \exp(-\text{LAI}/2)(1-\exp(-\text{LAI}/2))$ , for $\text{LAI} > 0.5$ $d = h [1-2(1-\exp(-\text{LAI}/2))/\text{LAI}]$	Pereira et al. (1996)

Where, LAI is the leaf area index, and  $h$  is the height of crop.

$Z_{om} \neq Z_{oh}$  (e.g. *Koshiek et al.*, 1993). Usually  $Z_{om}$  and  $Z_{oh}$  are compared in the equation:

$$\frac{k}{B} = \ln \left( \frac{Z_{om}}{Z_{oh}} \right) \quad [-] \quad (2.8)$$

Where,  $B$  is a function of a temperature profile. *Garrat* (1978) demonstrated that  $Z_{oh}$  can be one-seventh of  $Z_{om}$  ( $k/B = 2$ ). *Brutsaert* (1982) indicated that  $Z_{oh}$  is one or more orders of magnitude smaller than  $Z_{om}$  ( $k/B > 2.3$ ). For "permeable-rough" surfaces such as uniform canopies, *Choudhury* (1989) showed that  $k/B$  is approximately 2 to 3. However for heterogeneous surfaces,  $k/B$  can hardly be practically solved (*Blyth and Dolman*, 1995). To correct for the effects of (in)stability conditions, which may result in buoyancy or damping effects, the (in)stability correction factors are included in Eq. (2.7). The parameterizations of the stability functions are discussed at length by *Brutsaert* (1982). Under neutral conditions with  $T_o - T_a = 0$ ,  $\psi_h = \psi_m = 0$ . It has been shown (e.g. *Kohsiek et al.*, 1993) that the effect of the stability functions on the sensible heat flux is small and that the effect of the roughness lengths is relatively large.

## 3.

### Description of Field Measurements

#### 3.1 Introduction

Two field data sets have been used in the current study: Lake Naivasha Vineyard data set, and Ndabibi data set. The Lake Naivasha Vineyard data set was collected in a field campaign, which was conducted during October 3 – 13, 1998 at the Lake Naivasha Vineyard Farm. The Ndabibi data set was provided by Farah, who opened a new experimental meteorological station at Ndabibi. The Lake Naivasha Vineyard- and the Ndabibi data sets are mainly used to calibrate and validate evapotranspiration equations (Chapter 4). The description of these data sets is the main issue of this chapter.

#### 3.2 The Study Area

##### *Location*

The Lake Naivasha basin, stretching over an area of 3200 Km<sup>2</sup>, lies in the East African Rift Valley, about 100 km Northwest of Nairobi. Its geographical coordinates are 0<sup>0</sup> 00' to 1<sup>0</sup> 00' S and 36<sup>0</sup> 00' to 36<sup>0</sup> 45' E. Administratively, it is situated in the Naivasha division, Nakuru district, Rift Valley province of Kenya.

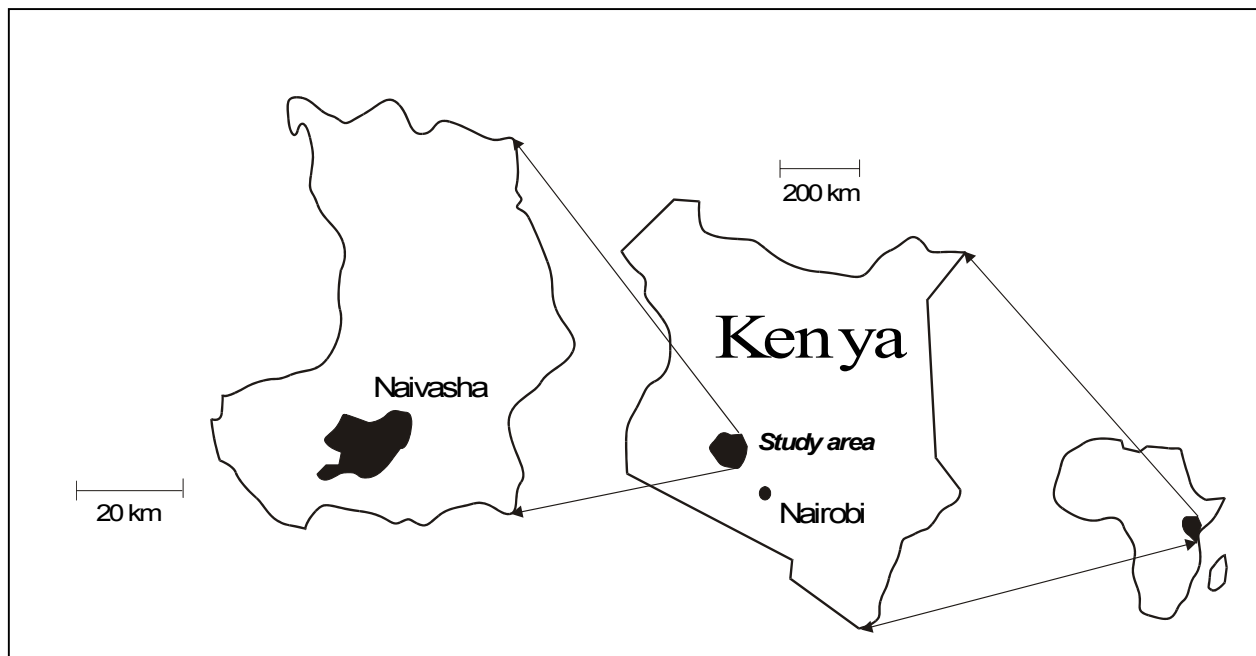
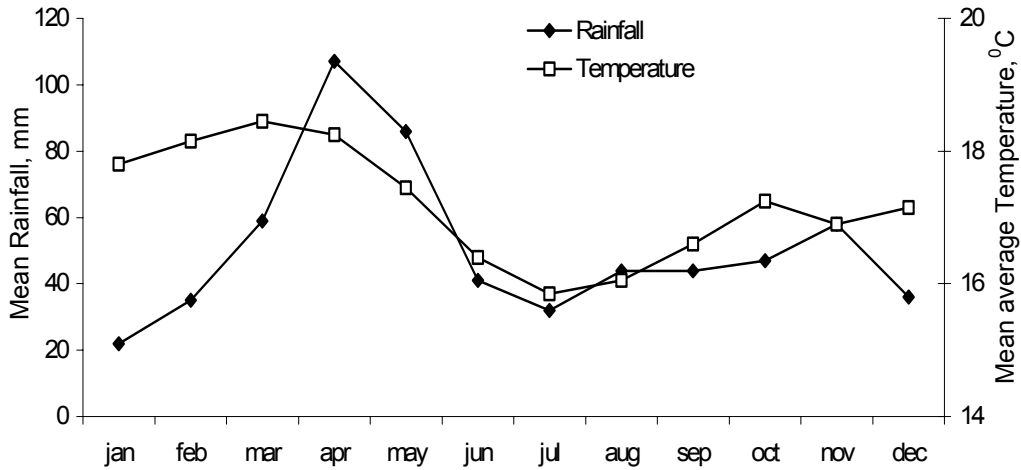


Fig. 3.1 The study area in international, national, and regional contexts.

Climate

Two rainy seasons and large diurnal temperature variations are typical characteristics of the climate in the area. The aridity index (precipitation / potential evapotranspiration), around the lake, is about 0.3 - 0.5. The mean monthly values of some meteorological state variables are shown in Fig. 3.2.



Mean Rainfall, mm	22	35	59	107	86	41	32	44	44	47	58	36
Maximum Temperature, °C	17.8	18.1	18.5	18.3	17.5	16.4	15.9	16.1	16.6	17.3	16.9	17.2
Minimum temperature, °C	8	8.1	9.7	11.5	11.2	9.8	9.2	9.3	8.7	9.0	9.2	8.6
Relative Humidity, %	62	61	65	75	80	79	77	76	74	72	77	72
Windspeed, km day <sup>-1</sup>	104	104	104	104	121	121	121	130	130	130	104	104
Sunshine, hours	5.9	5.9	5.3	4.7	4.9	4.8	4.2	4.7	5.4	5.5	4.4	4.2
Solar Radiation, W m <sup>-2</sup>	171	186	179	164	157	150	143	159	177	179	158	152

Fig. 3.2 Mean monthly values of meteorological observations for the Lake Naivasha area (recorded in Naivasha Meteorological Station). Source: FAO's CROPWAT database.

Geology and soils

In general, the study area is covered by two types of quaternary deposits: lacustrine, and volcanic origin. The deposits contain largely clay, silt, and volcanic materials. The soils can also be grouped into two: soils developed on the lacustrine plain, and soils developed on the volcanic plain. Soils developed on the lacustrine plain are moderately to well drained, very deep, silty clay to clay loam. Soils developed on the volcanic plain are well drained, moderately deep to very deep, with noncalcareous to moderately calcareous topsoil.

### *Landuse*

There are four major landuse/landcover units in the area: agriculture, natural vegetation, settlements, and game sanctuaries. The agriculture sector, which includes cereal growing, horticulture, floriculture, viticulture, and dairy farming, is mainly concentrated around the lake. Most of the floriculture takes place inside greenhouses. The natural vegetation cover surrounding the lake is mainly papyrus swamp vegetation while outside of the lake surrounding, shrub, acacia, and cactus trees are the main natural vegetation covers. Settlement is mainly concentrated in Naivasha town although scattered homes and villages can also be found within the study area. Game sanctuaries are mainly present in the west of the study area.

### *Irrigation Practice*

Most of the irrigation schemes lie around the periphery of the lake. Efficient irrigation systems are employed: sprinkler (mainly for openfield) and drip (mainly for greenhouse). In either case, irrigation water is pumped from the lake, and stored temporarily in a reservoir until it is withdrawn for irrigation purpose. In the greenhouses, flowers (typically roses) are grown for export purpose. Whereas, vegetables (squash, chilli and others), cereals (bean, maize and others), and flowers are grown in openfields. Irrigation scheduling is not properly practiced in the area. Some farmers irrigate when they feel the soil gets dry, while others do on some traditional basis. The size of individual farms varies from 3 to 6400 acre.

## **3.3 Lake Naivasha Vineyard Data Set**

### **3.3.1 Site Description**

A number of factors had to be considered in selecting suitable sites for the study. Targets were irrigated sites. Besides, individual sites must be homogeneous and reasonably large to minimize the effect of advection. As a group, all the sites must be close to each other, and must bear different types of dominant crops including bare soil. Following these criteria, four sites were selected as shown in Fig. 3.3.

The mean daily air temperature during the field campaign was about 22 °C with an average relative humidity of 80 %. The daily maximum temperature was 24.5 °C. The afternoons were usually cloudy. A few heavy downpours were also observed during the last week of the campaign period. The characteristics of the sites are shown in Table 3.1.

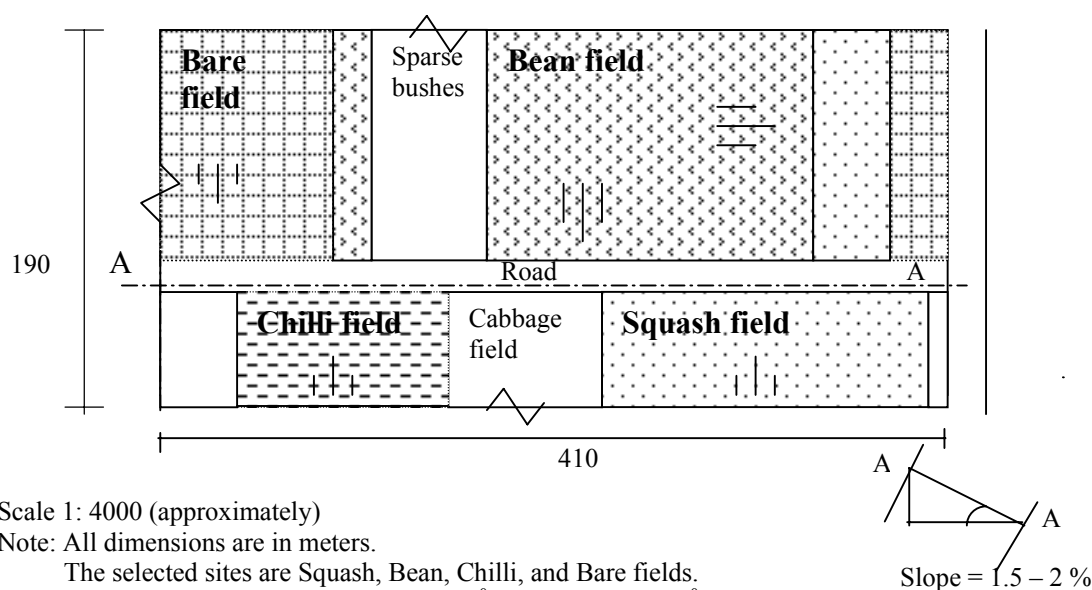


Fig. 3.3 Schematic Plan view of the study sites.

Table 3.1 Site characteristics

Parameter	Characteristics		
	Squash field	Bean field	Chilli field
<b>Crop parameters</b>			
Type of crop	Squash (Courgette)	Bean (Phaseolus Nulgaries)	Chilli
Root depth (cm)	20	15	18
Crop height (cm)	50	38	37
Canopy width (cm)	125	30	40
Weed infestation	Present	Absent	Absent
Ground vegetal cover fraction	0.76	0.65	0.35
Length of growing days	75	61	105
<b>Soil parameters</b>			
Soil texture	Sandy loam	Sandy loam	Sandy loam
Soil structure	Angular to subangular blocks	Angular to subangular blocks	Angular to subangular blocks
PH	7 - 7.8	7 - 7.8	7 - 7.8
<b>Irrigation practice</b>			
Irrigation type	Sprinkler	Sprinkler	Sprinkler
Irrigation interval (days)	7	4	14
Irrigation duration (hours)	3	3	3
Duty ( $l \text{ sec}^{-1} \text{ ha}^{-1}$ )	unknown	unknown	Unknown
Drainage problem	Absent	Absent	Absent
Salinity problem	Absent	Absent	Absent
<b>Topographic features</b>			
Average slope (%)	1.5-2	1.5-2	1.5-2
Slope length	Moderate	Moderate	Moderate
Aspect	North	South	South/East

### 3.3.2 Field Measurements and Data

The fieldwork was directed towards the assessment of the surface energy transfer parameters of the four types of land covers. Hence, it was focused on:

- Acquisition of micro-meteorological data;
- Observation of surface parameters; and
- Collection of soil moisture data.

The parameters measured and their instrumentation are listed in Table 3.2. All the employed instruments were hand-held. The micro-meteorological parameters were routinely measured during daytime. The approximate time required to take a consecutive measurement at the same spot was about one hour. Owing to logistical difficulties, the solarimeter was available only for a few days.

Table 3.2 *In-situ measured hydro-meteorological parameters and instrumentation*

Parameter	Symbol	Instrument	Elevation above surface level (cm)	No. of nearly instantaneous measurement spots per one site
<b>Micro-meteorological</b>				
Shortwave incoming radiation	$K_{\downarrow}$	Solarimeter	10	1
Shortwave reflected radiation	$K_{\uparrow}$	Solarimeter	10, 70	8 – 12
Longwave incoming radiation	$L_{\downarrow}$	Thermal infrared radiometer	175	4
Longwave reflected radiation	$L_{\uparrow}$	Thermal infrared radiometer	10, 70, 175	12 -16
Air temperature	$T_a$	Thermocouple	175	4
Air relative humidity	RH	Psychrometer	175	4
Wind speed	u	Anemometer	175	4
<b>Soil</b>				
Soil moisture content	$\theta$	Time domain reflectrometry	-5, -10, -15, -30, -45, -60, -100, -120, -140, -150	1 and more depending on the purpose

#### *Reliability of Data*

The reliability of data was examined by comparing measurements taken simultaneously by the employed instrument and another instrument. The relative humidity (RH) readings, taken directly by the psychrometer, and obtained through calculation using the wet and dry bulb temperatures, deviated unsystematically and significantly. Hence, the RH readings are not used in any of the calculations. The infrared radiometer and a thermometer took simultaneous measurements over tap water. The temperature of the tap water was varying from 20 to 40 °C. In this range, both readings, taken by the radiometer and the thermometer, were exactly the same. Hence, the emissivity, at which the radiometer was set, was considered as one. The air temperature readings taken by the thermocouple and a thermometer were the same. The windspeed measured using the employed anemometer and another anemometer were also the same.

### 3.4 The Ndabibi Data Set

This data set consists of meteorological data extending on a continuous basis from May 1998 to January 1998. The Ndabibi meteorological station, which has become operational since May 1998, is located about 6 km Northwest of the Lake Naivasha Vineyard site. In this station, solar radiation, air temperature and relative humidity are measured every 20 minutes on a routine basis.

#### Reliability of Data

The proper way of assessing the accuracy of data is to compare measurements taken simultaneously by the employed instrument and another reliable instrument. But this was not done for the current data set. However, instead of taking the reliability of the data for granted, a rough assessment is made as follows. The incoming solar radiation is mainly influenced by the cloudiness condition. The latter can be assessed from the difference of the maximum- and minimum daily air temperatures ( $T_{\max} - T_{\min}$ ), a cloudy day resulting in low  $T_{\max} - T_{\min}$  value than does a clear sky. Hence, the relationship between the trends of  $T_{\max} - T_{\min}$  and  $K_{\downarrow}$  can be exploited to gain an indication whether the data are relatively acceptable or not. It is emphasized here that this type of comparison can only give a rough indication, and it is used here in lack of any other better alternative. Fig. 3.4 shows that, generally speaking, the trends of  $T_{\max} - T_{\min}$  and  $K_{\downarrow}$  (or  $K_{\text{inc.}}$ ) are similar to each other, and hence, these data can be used for further analysis.

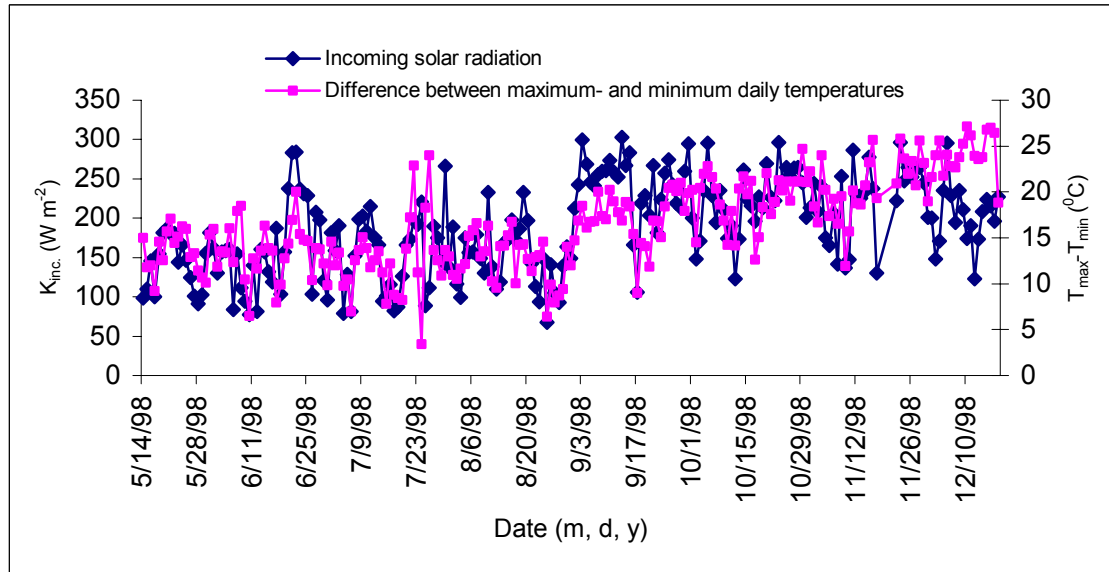


Fig. 3.4 Comparison of incoming solar radiation ( $K_{\downarrow}$  or  $K_{\text{inc.}}$ ) and the difference between maximum- and minimum daily air temperature ( $T_{\max} - T_{\min}$ ) trends.

### Frequency of Occurrence

The daily average values of relative humidity (RH), incoming solar radiation ( $K_{\downarrow}$  or  $K_{inc.}$ ), and air temperature at 2m height ( $T_a$ ) are calculated for a period of eight months. The temporal variability of these values is studied using cumulative frequency plots and some statistical measures.

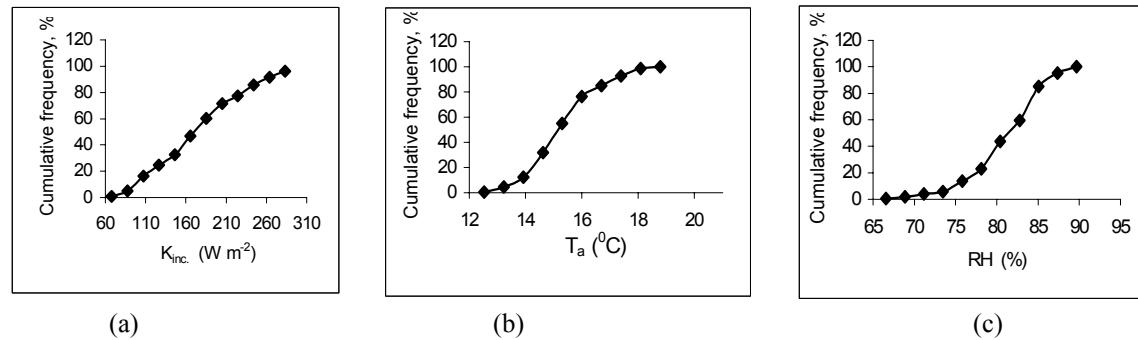


Fig. 3.5 Cumulative histogram plots for daily averages of (a)  $K_{inc.}$  ( $K_{\downarrow}$ ), (b)  $T_a$ , and (c) RH.

Table 3.3 Quartile values for the distribution of some atmospheric state variables

State variables	Quartile values		
	Q1	Q2	Q3
$K_{\downarrow}$ ( $W m^{-2}$ )	128.94	171.75	217.89
$T_a$ ( $^{\circ}C$ )	14.45	15.16	15.97
RH (%)	78.51	81.43	84.05

It can be seen from Fig. 3.5 that large frequencies of  $K_{\downarrow}$  occur a wide range of data (about 110 to 310  $W m^{-2}$ ), while the largest frequencies of both  $T_a$  and RH are limited over a smaller range. The quartile values in Table 3.3 show that 50 % of the population of  $K_{\downarrow}$  values lie between 129 and 218  $W m^{-2}$  (a span of 69 % difference in magnitude), while in  $T_a$  and RH, the span of the difference incurred by 50 % of the population amount to only 10 % and 7 %, respectively. It becomes clear from the above analysis that the deviations in  $T_a$  and RH are small and hence, reasonable estimates of these data can be made in the absence of measured values. However, since the deviations in  $K_{\downarrow}$  are considerable, estimation of this variable in its absence may result in significant error.

## 4.

### Calibration and Validation of Evapotranspiration Equations, using field data

#### 4.1 Introduction

*Purpose:* Remote sensing approaches of estimating  $ET_c$  and  $ET_{ref}$  contain some empirical elements. Hence, they should be calibrated and validated before they become operational.

*Scale :* The calibration and validation of evapotranspiration equations is carried out at the field scale. Instantaneous- and daily temporal scales are considered. The Lake Naivasha Vineyard data set is used in the instantaneous scale analysis, while the Ndabibi data set in the daily scale analysis.

The statistical methods used for assessing association are described in Annex A. While reading through this Chapter, the reader is advised to note the time scale used in the analysis.

#### 4.2 Instantaneous Time Scale

##### 4.2.1 Crop Potential Evapotranspiration ( $ET_c$ ) equations

The crops involved in the study (Squash, Bean, and Chilli) were irrigated by sprinklers. The calculated day time ( $R_n > 0$ ) average of the sensible heat flux was found to be close to zero. It would therefore seem reasonable to assume that the crops were able to transpire freely at an energy rate equal to the available energy. The balance of energy always holds true.

*Equation to be validated:* Priestley-Taylor (Eq. 2.3), with  $\alpha = 1.26$ . As  $\alpha$  has been mostly found out to be 1.26 (e.g. Brutsaert, 1982), direct validation of this method, without calibration, is preferred.

#### Involved equations

The Energy balance Residual (E-R) equation (Eq. 2.4) is used to validate the Priestley-Taylor (P-T) equation. A brief description of the energy balance terms and their parameterizations is given in Chapter 2. Further formulations required to solve these equations are enumerated below:

$$T_o = \left( \frac{L_{\uparrow} - (1 - \epsilon_o)L_{\downarrow}}{\epsilon_o \sigma} \right)^{0.25} \quad [K] \quad (4.1)$$

$$\rho_a = \frac{P_a}{0.287(T_a - 273)} \quad [kg \ m^{-3}] \quad (4.2)$$

$$P_a = 101.3 \left( \frac{T_a - 0.0065A}{T_a} \right)^{5.256} \quad [\text{k Pa}] \quad (4.3)$$

$$G = R_n T_o (0.0032\alpha_o + 0.0062(\alpha_o)^2)(1 - 0.98(\text{NDVI})^4) / \alpha_{inst} \quad [\text{W m}^{-2}] \quad (4.4)$$

$$\alpha_{inst} = \frac{K_{\uparrow}}{K_{\downarrow}} \quad [-] \quad (4.5)$$

$$\alpha_o = \frac{\sum_{j=1}^{j=j_d} K_{\downarrow j} \alpha_{instj}}{\sum_{j=1}^{j=j_d} K_{\downarrow j}} \quad [-] \quad (4.6)$$

$$\Delta = \frac{4098e_{a,sat}}{(237.3 + (T_a - 273))^2} \quad [\text{k Pa } ^\circ\text{C}^{-1}] \quad (4.7)$$

$$e_{a,sat} = 0.6108 \exp\left( \frac{17.27(T_a - 273)}{237.3 + (T_a - 273)} \right) \quad [\text{k Pa}] \quad (4.8)$$

$$\gamma = \frac{0.0016286P_a}{\lambda_v} \quad [\text{k Pa } ^\circ\text{C}^{-1}] \quad (4.9)$$

$$\lambda_v = 2.501 - 0.002361(T_a - 273) \quad [\text{MJ kg}^{-1}] \quad (4.10)$$

Note: See the list of symbols for description. In Eq. (4.6), j refers to instantaneous time at which solar radiation measurements were performed, and j<sub>d</sub> refers to the number of j's in one day. T<sub>o</sub> in Eq. (4.4) is expressed in <sup>o</sup>C. The above equations are compiled from *Bastiaanssen and Roebeling* (1993), *Bos et. al.* (1996), and *Dingman* (1994).

### Assigning input values

Although most of the dominant variables that are required to calculate ET<sub>c</sub> were measured in the field, there were some variables which had to be estimated. Table 4.1 describes the method of assigning value to each variable involved in ET<sub>c</sub> calculation. Furthermore, Table 4.2 shows the estimated values, with the reasons behind them.

Table 4.1 Methods of assigning values to the variables/parameters involved in ET<sub>c</sub> equations

Measured	Estimated	Calculated	Calculated	Constants
L <sub>↓</sub>	ε <sub>o</sub>	T <sub>o</sub>	Z <sub>oh</sub>	δ [W m <sup>-2</sup> K <sup>-4</sup> ] = 5.67*10 <sup>-8</sup>
L <sub>↑</sub>	ψ <sub>m</sub>	ρ <sub>a</sub>	α <sub>inst</sub>	c <sub>p</sub> [J kg <sup>-1</sup> K <sup>-1</sup> ] = 1004
T <sub>a</sub>	ψ <sub>h</sub>	P <sub>a</sub>	α <sub>o</sub>	A [m] = 2000
u	Z <sub>om</sub>	r <sub>ah</sub>	Δ	k [-] = 0.41
K <sub>↓</sub>	d	Rn	γ	Z [m] = 1.75
K <sub>↑</sub>	NDVI	G	λ <sub>v</sub>	
	kB <sup>-1</sup>	H	e <sub>assat</sub>	

Table 4.2 Estimated input values

State Variable	Estimated Value/equation/condition	Ground for estimation
Z <sub>om</sub> [m] (canopy)	0.10	For NDVI > 0.6, Z <sub>om</sub> = 0.1, Moran and Jackson (1991)
Z <sub>om</sub> [m] (soil)	0.0064	As used by Peters (1995) for similar soil type in semi-arid environment.
kB <sup>-1</sup> [-] (canopy)	2.3	Brutsaert (1982)
kB <sup>-1</sup> [-] (soil)	10	Peters (1995)
d [m] (canopy)	0.067	Moran and Jackson (1991), and Allen et al. (1996)
d [m] (soil)	0	
ε <sub>o</sub>	0.96	
Thermal Condition	Neutral (ψ <sub>h</sub> = ψ <sub>m</sub> = 0)	Field experience
NDVI	f (LAI)	A graph showing NDVI as a function of LAI, in Meijerink et al. (1994).

### Scaling up fluxes

The sites under study had without exception partial vegetation cover, hence theory of sparse canopies should be applied. The energy fluxes are calculated for each component of the land surface using the formulations stated in relevant sections, and then they are scaled up to a site level. The evapotranspiration equations are computed for field scale conditions. An approach, which is felt to be feasible within the boundary conditions of this study, is to regard the site energy fluxes as a weighted average of energy fluxes coming from bare soil, crop, and weed components. The amount of energy fluxes welling up from an inhomogeneous site with a crop fraction (f<sub>1</sub>), a bare soil fraction (f<sub>2</sub>), and a weed fraction (f<sub>3</sub> = 1 - f<sub>2</sub> - f<sub>1</sub>) is given by:

$$R_n = f_1 R_{n,crop} + f_2 R_{n,baresoil} + f_3 R_{n,weed} \quad [\text{W m}^{-2}] \quad (4.11)$$

$$G = f_1 G_{crop} + f_2 G_{baresoil} + f_3 G_{weed} \quad [\text{W m}^{-2}] \quad (4.12)$$

$$H = f_1 H_{crop} + f_2 H_{baresoil} + f_3 H_{weed} \quad [\text{W m}^{-2}] \quad (4.13)$$

Table 4.3 Proportion of land cover components, f<sub>i</sub>, within a site (in fraction)

	f <sub>1</sub> (crop)	f <sub>2</sub> (soil)	f <sub>3</sub> (weed)
Squash field	0.585	0.241	0.174
Bean field	0.65	0.35	0
Chilli field	0.35	0.65	0

### Analyses of results

The plots in Fig. 4.1 compare the instantaneous ET<sub>c</sub> values estimated using Energy balance Residual (E-R) and Priestley-Taylor (P-T) (with α = 1.26) equations. Furthermore, Table 4.4 summarizes the regression constant (a), the coefficient of determination (R<sub>o</sub><sup>2</sup>), the efficiency factor (E), and the t-statistic, for the two equations.

The fact that R<sub>o</sub><sup>2</sup> is high (in excess of 0.94 for all the fields) shows that the ET<sub>c</sub> values computed by the two equations are highly correlated. The slopes of the regression lines for all the fields are between 0.94 and 1.03, which are close to one. The high

values of E (above 0.92 for all the fields) confirm that the two estimates are close to each other.

The P-T equation yields estimates that are statistically significant at the particular confidence level, i.e.,  $1 - \alpha = 99.5\%$ , as the calculated  $t$  values are less than the critical  $t$  values. The small statistically insignificant differences between the two estimates can be attributed to many uncertainties inherent in this type of study. Some could be described as: instrumental accuracy, assumption of neutral thermal condition, and use of a non-calibrated empirical equation to determine G.

Based on the foregoing discussion, it can be concluded that there is a high degree of agreement between the  $ET_c$  estimates made by E-R and P-T equations. This means that  $ET_c$  can be adequately estimated using P-T equation with  $\alpha = 1.26$ . This result is very encouraging because the variables involved in P-T equation can be retrieved from satellite data.

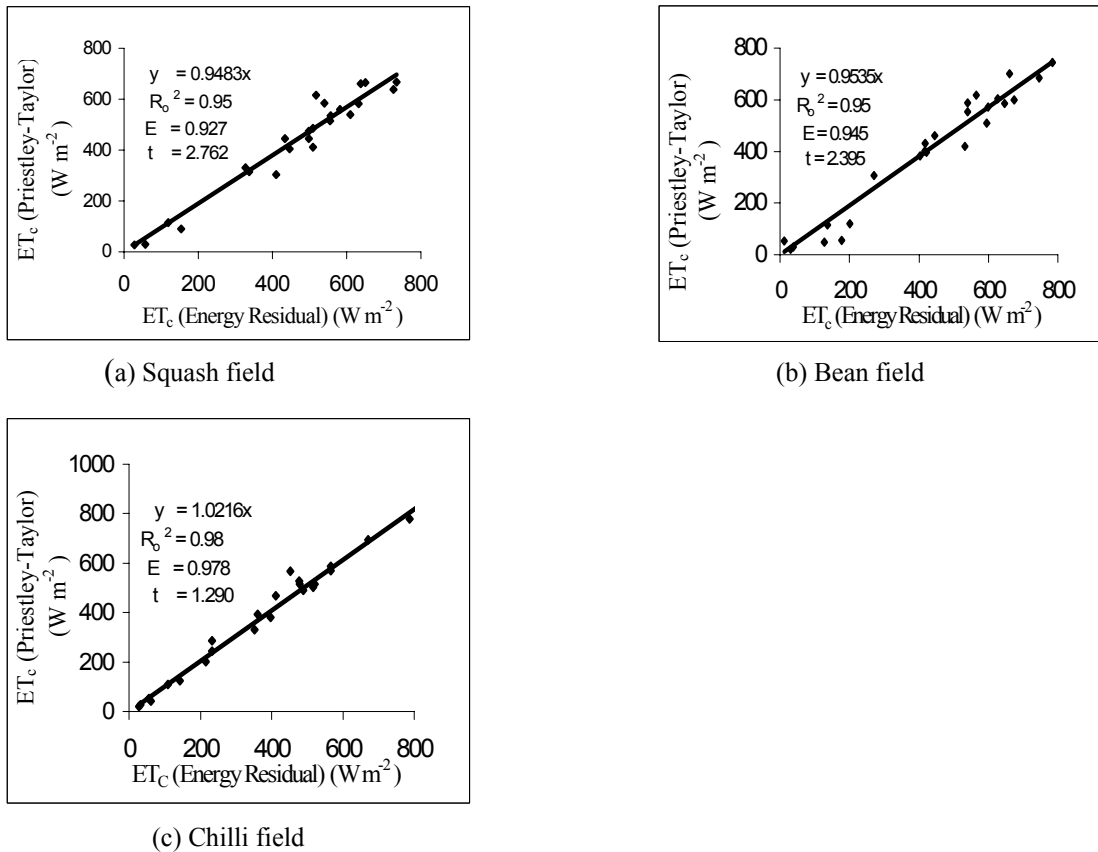


Fig. 4.1 Comparison of instantaneous  $ET_c$  estimated using Energy balance Residual and Priestley-Taylor equations over (a) Squash, (b) Bean, and (c) Chilli fields.

Table 4.4 Values of statistical indicators of  $ET_c$  values estimated using P-T and E-R equations over different cover types

Cover type	a	$R_o^2$	E	t	t-critical
Squash	0.9483	0.95	0.927	2.762	2.807
Bean	0.9535	0.95	0.945	2.395	2.797
Chilli	1.0216	0.98	0.978	1.290	2.807

Note: 'a' and ' $R_o$ ' refer to the slope- and regression coefficient of the equation that is forced to pass through the origin, see Annex A for formulations.

Table 4.4 shows that the E-R and P-T  $ET_c$  estimates are very close to each other over the chilli field than the other fields. This would not necessarily mean that P-T equation is more reliable for the chilli field than for the other fields. It simply means that the assumptions and the empirical equations involved in E-R equation may not be equally valid for the three land cover types. The reason is explained below.

The term  $ET_c$  implies that the plant is transpiring at the potential rate but it doesn't mean that the bare soil between the plants is evaporating potentially. Consequently, during daytime, the surface of the bare soil tends to be warmer than the canopy. Warmer soil surface introduces unstable condition, which amplifies the vertical motion of the eddies thereby influencing  $ET_c$ . The higher the proportion of bare soil, the higher will be the effect of the eddy amplification. As no correction has been made for these effects in the calculation of  $ET_c$ , the degree of correlation between the two estimates could be different from one field to the other. The other reason for the difference could be attributed to the empirical equation used to calculate the soil heat flux. There is no any clue that guarantees the empirical equation used to estimate the soil heat flux works well for the NDVI range from nearly 0 to 0.75 (as used in the current analysis). One way to verify consistency is to calculate the surface resistance from latent heat flux, but this is not done in lack of reliable vapor pressure data.

Another issue worth consideration is: *Does the correlation between  $ET_c$  values estimated using E-R and P-T equations deviate significantly if the assumptions involved, as shown in Table 4.2, are altered?* This is studied using the sensitivity analysis, which is discussed in the next section.

### Sensitivity analysis of soil- and sensible heat fluxes

The sensitivity of the correlation between  $ET_c$  estimates, made by E-R and P-T equations, to various assumptions is studied by varying each assumed value within the reasonable limits while holding all others constant. This technique ignores the feedback consequences.

Using the originally assumed values (Table 4.2), the following regression equation has already been established between E-R and P-T  $ET_c$  estimates:

$$ET_{c(P-T)} = a_c ET_{c(E-R)}$$

Where,  $a_c$  refers to the slope of the regression line forced to pass through origin when the originally assumed values are used in the analysis, the subscripts P-T and E-R refer to P-T and E-R equations, respectively, used to calculate  $ET_c$ .

To conduct sensitivity analysis, each assumed value mentioned in Table 4.2 is altered, one at a time, to a new value shown in Table 4.5. Except the changed parameter, all the rest will take the originally assumed values. Using this new data combination,  $ET_c$  values are calculated using E-R and P-T equations, and then the regression equation of the following form is established between the two  $ET_c$  estimates:

$$ET_{c(P-T)} = a_e ET_{c(E-R)}$$

Where,  $a_e$  refers to the slope of the regression line forced to pass through origin, when one of the originally assumed values is changed.  $a_e$  is calculated for each set of value listed in Table 4.5.

To study the difference between  $a_c$  and  $a_e$  values, a new term called ‘relative deviation ( $\epsilon_a$ )’, is introduced:

$$\epsilon_a = \left( \frac{a_e - a_c}{a_c} \right) * 100 \quad [\%] \quad (4.14)$$

For each set of parameter given in Table 4.5, the corresponding  $\epsilon_a$  value is calculated. The maximum  $\epsilon_a$ , among all the calculated  $\epsilon_a$  values, obtained for each cover type is shown below:

<u>Cover type</u>	<u>maximum <math>\epsilon_a</math> (%)</u>
Squash	0.92 (+)
Bean	1.10 (+)
Chilli	2.53 (-)

Table 4.5 Values of statistical indicators of  $ET_c$  estimated using P-T and E-R equations over different cover types and under different assumptions

Parameter considered	Assumed value, or equation	Cover type					
		Squash		Bean		Chilli	
		$a_e$	$R_o^2$	$a_e$	$R_o^2$	$a_e$	$R_o^2$
$Z_{om}$ [m] (canopy)	0.07	0.953	0.960	0.959	0.954	1.021	0.982
	0.10	0.948	0.945	0.954	0.954	1.022	0.980
	0.15	0.940	0.919	0.945	0.934	1.023	0.976
d [m] (canopy)	0.0	0.949	0.947	0.954	0.956	1.022	0.980
	0.67	0.948	0.945	0.954	0.954	1.022	0.980
	0.10	0.948	0.944	0.953	0.953	1.022	0.980
$kB^{-1}$ (canopy)	2.3	0.948	0.945	0.954	0.954	1.022	0.980
	5.0	0.957	0.972	0.964	0.975	1.020	0.984
$kB^{-1}$ (soil)	10.0	0.948	0.945	0.954	0.954	1.022	0.980
	20.0	0.944	0.948	0.945	0.959	1.000	0.988
G ( $W m^{-2}$ )	Jackson et al. (1987)	0.946	0.921	0.953	0.928	1.024	0.973
	Bastiaanssen and Roebeling (1993)	0.948	0.945	0.954	0.954	1.022	0.980
	Kustas and Daughtry (1990)	0.947	0.927	0.954	0.938	1.012	0.983

Note:- ‘ $a_e$ ’ refers to the slope of the regression line forced to pass through the origin, that is,

$$ET_{c(P-T)} = a_e ET_{c(E-R)}$$

As shown above, the maximum deviation in the slope of the regression line between P-T and E-R  $ET_c$  estimates, which can be introduced due to change in the assumed values of some of the variables, is insignificant. *This implies that irrespective of the magnitude of the assumed values (as long as they lie within the acceptable limits), the agreement between E-R and P-T  $ET_c$  estimates remains satisfactory.*

### Another alternative ?

In the preceding section, it has been shown that P-T equation can yield reasonable estimates of  $ET_c$ . The inputs of P-T equation consist of air temperature, net radiation, and soil heat flux from saturated surface. As a possible alternative, it was tried to

relate all these input variables to only surface temperature and incoming radiation, which are easy to retrieve from satellite data. The following daytime instantaneous empirical equation has been developed in a sort of trial-and-error procedure, as described in Annex B.

$$ET_c = AT_o^2 + BT_oK_{\downarrow} + CT_o + DK_{\downarrow} + E \quad [\text{W m}^{-2}] \quad (4.15)$$

$T_o$  is expressed in  $^{\circ}\text{C}$ . For the current data set,  $A = 0.04$ ,  $B = -0.0052$ ,  $C = -8.65$ ,  $D = 0.882$ , and  $E = 123.571$  has been calculated for all the three crops.

In Fig. B.1, the results of the above equation are compared with those estimates made using E-R equation. It can be seen that the agreement between the two estimates is very good. For practical applications, this result is of great importance. The developed equation has also been tested for Lake evaporation using the field data collected by *Ashfaq* (1999), the result is found to be very encouraging. However, it should be noted that the coefficients involved in Eq. (4.15) only apply to the conditions encountered in Kenya during October.

#### 4.2.2 Grass Reference Evapotranspiration ( $ET_{ref}$ ) Equations

Since no physical measurements over the "reference grass" were performed in the study area, E-R equation can not be directly used here. However, since the aerodynamic characteristics of the reference grass are close to the crops under study, the P-T equation which has been validated in Section (4.2.1) can be used (with albedo = 0.23) to calculate  $ET_{ref}$ .

All the variables involved in P-T equation, except  $G$ , can be solved using the formulations stated in the preceding Sections. Since the height of the reference grass is fixed, the equation proposed by *Reginato et al.* (1985) is used to estimate  $G$ :

$$G = R_n(0.1 - 0.042h) \quad [\text{W m}^{-2}] \quad (4.16)$$

Where,  $h$  is the height of crop. For the reference grass,  $h = 0.12$  m, Eq. (4.16) then reduces to,  $G = 0.1R_n$ .

The P-T equation can thus be rewritten as:

$$ET_{ref} = 1.134 \frac{\Delta}{\Delta + \gamma} R_n \quad [\text{W m}^{-2}] \quad (4.17)$$

#### 4.2.3 Validated $K_c$ equation, on an instantaneous time scale

The validated  $ET_c$  and  $ET_{ref}$  equations are depicted in Eqs. (2.3) and (4.17), respectively. Applying these two equations,  $K_c$  on an instantaneous time scale can be written as:

$$K_c = \frac{K_n + L_n - G}{0.693K_{\downarrow} + 0.9L_n} \quad [-] \quad (4.18)$$

### 4.3 Daily Time Scale

#### *Crop Potential Evapotranspiration ( $ET_c$ ) equations*

Jackson *et al.* (1983), Shuttleworth *et al.* (1989), Choudhury *et al.* (1994), and others have shown that various ratios of the energy budget components often vary little during daytime. The invariance of the flux ratios has been exploited to extrapolate an instantaneous flux to a daily flux. The application of the evaporative fraction (EF) approach in USA by Kustas and Norman (1996), in France by Zhang and Lemeur (1995), in Spain and Egypt by Bastiaanssen (1995), and in Niger by Stewart (1996) yielded proper estimates of daily total evapotranspiration. This study utilizes the EF approach to convert instantaneous evapotranspiration to a daily time scale.

$$EF = \frac{ET_c}{ET_c + H} = \frac{ET_c}{R_n - G} \quad [-] \quad (4.19)$$

For a cycle of a day,  $G \approx 0$ , implying that:

$$ET_c = EFR_{n24} \quad [W \text{ m}^{-2}] \quad (4.20)$$

Combining Eq. (4.20) with Priestley-Taylor equation, and rearranging yields the following expression for EF:

$$EF = \alpha \frac{\Delta}{\Delta + \gamma} \quad [-] \quad (4.21)$$

#### *Grass Reference Evapotranspiration ( $ET_{ref}$ ) Equations*

In the preceding section, a formulation for  $ET_c$  on a daily scale has been stated. The same  $ET_c$  equation can be used to estimate  $ET_{ref}$  (with albedo = 0.23).

#### **Validated $K_c$ equation, on a daily scale**

Applying the validated P-T equation for  $ET_c$  and  $ET_{ref}$ ,  $K_c$  on a daily scale can be written as:

$$K_c = \frac{K_{n24} + L_{n24}}{0.77K_{\downarrow 24} + L_{n24}} \quad [-] \quad (4.22)$$

Eq. (4.22) shows that  $K_c$  is mainly a function of albedo, among crop parameters.

### 4.4 Testing Parameterizations of $K_c$ parameters

The  $K_c$  parameters, which are required to solve  $K_c$  as per the validated equations, can be calculated using appropriate ground-based data. However, empirical equations which require simple inputs are reported in the literature to estimate these  $K_c$  parameters. In this section, the reliability of these empirical equations will be investigated.

#### 4.4.1 Instantaneous Time Scale

$L_n$ ,  $K_{\downarrow}$ ,  $\alpha_{\text{inst}}$ , and  $G$  are the parameters, which are required to calculate  $K_c$  on an instantaneous time scale, as per Eq. (4.18).

*Net longwave radiation ( $L_n$ )*

From the Stefan-Boltzmann and continuity equations,  $L_n$  can be written as:

$$L_n = \varepsilon_a \sigma T_a^4 - (1 - \varepsilon_0) \varepsilon_a \sigma T_a^4 - \varepsilon_0 \sigma T_0^4 \quad [\text{W m}^{-2}] \quad (4.23)$$

The above equation requires many ground-based input data. To the author's knowledge, there are no simple empirical equations reported so far to estimate  $L_n$  on an instantaneous time scale. Can the empirical equations reported to estimate  $L_n$  on a daily scale be successfully applied to an instantaneous time scale?

*Slob*, as cited by *De Bruin* (1987), suggested that, on the daily scale:

$$L_n = -110 \frac{K_{\downarrow}}{K_{\downarrow}^{\text{TOA}}} \quad [\text{W m}^{-2}] \quad (4.24)$$

The applicability of this equation to an instantaneous time scale is studied by comparing the modelled  $L_n$  values with the corresponding measured  $L_n$  values. It can be seen from Fig. 4.2 that the measured  $L_n$  values are by far lower than the modelled ones, and more over, there is no good association between the two estimates.

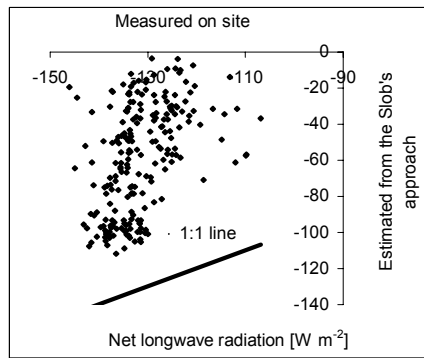


Fig. 4.2 Comparison of net longwave radiation measured on site and estimated using the Slob's approach.

If Eq. (4.23) is employed to compute  $L_n$ ,  $\varepsilon_a$  is relatively more difficult to estimate than the rest variables. Some of the reported equations for estimating  $\varepsilon_a$  are investigated below. Since accurate vapor pressure data was not collected in the field, only equations that do not require this data are considered. Here again, it is emphasized that these equations are reported for a daily scale, but they are applied here to an instantaneous scale.

Equations to be tested:

(1) Swinbank's equation:  $\varepsilon_a = 0.92 * 10^{-5} T_a^2$  [-] (4.25)

(2) Idso-Jackson' equation:  $\varepsilon_a = 1 - 0.261 \exp[-7.77 * 10^{-4} (273 - T_a)^2]$  [-] (4.26)

Equation used for testing:

$$\text{Inversion of Stefan-Boltzmann equation: } \varepsilon_a = \frac{L_{\downarrow}}{\delta T_a^4} \quad [-] \quad (4.27)$$

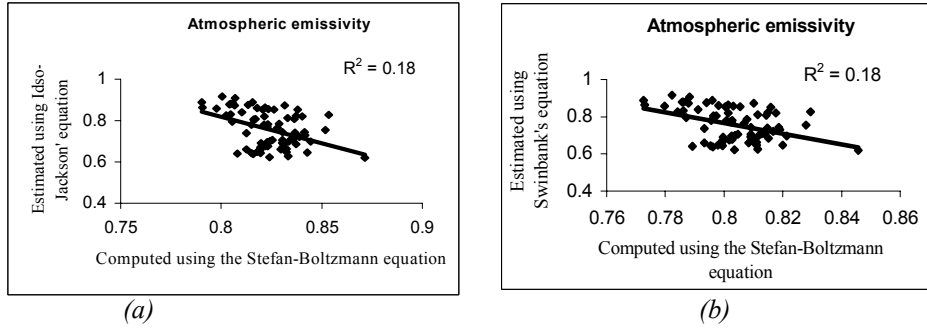


Fig. 4.3 Comparison of atmospheric emissivity estimated using Stefan-Boltzmann equation and (a) Idso-Jackson, and (b) Swinbank equations.

Fig. 4.3 displays the comparison of  $\varepsilon_a$  estimates made by Idso-Jackson and Swinbank equations with those obtained through the inversion of Stefan-Boltzmann equation. The plots in this figure reveal that there is no good association between  $\varepsilon_a$  estimates made by Stefan-Boltzmann and the other equations. From the above discussion, it can be concluded that neither Slob nor Idso-Jackson and Swinbank equations yield reasonable net longwave radiation on an instantaneous time scale.

#### Incoming solar radiation ( $K_{\downarrow}$ )

$K_{\downarrow}$  can be computed from extraterrestrial solar radiation and transmittance in the shortwave range, the latter being difficult to estimate. However, simple models, which require only solar zenith angle and air temperature data as inputs, are available in the literature for transmittance estimation. The reliability of these models is tested using meteorological data, as described in Annex C, which shows that it is hardly possible to obtain reasonable transmittance values from such type of models.

#### 4.4.2 Daily Time Scale

$K_{\downarrow 24}$ ,  $\alpha_0$ , and  $L_{n24}$  are the parameters, which are required to calculate  $K_c$  on a daily time scale, as per Eq. (4.22).

#### Daily incoming solar radiation ( $K_{\downarrow 24}$ )

It can be measured in specialized agrometeorological stations; however, owing to its careful calibration and maintenance, it is not usually available at standard stations (Shuttleworth, 1993). If sunshine hour data is available, it can adequately yield  $K_{\downarrow 24}$  using empirical relations available in the literature (e.g. Dorrenbos and Pruitt, 1977).

In the absence of sunshine hours data, Hargreaves *et al.* (1985) suggest the following empirical equation, which utilizes maximum- and minimum daily air temperatures:

$$K_{\downarrow 24} = a_0 K_{\downarrow 24}^{TOA} (t_{\max} - t_{\min})^{0.5} + a_1 \quad [\text{W m}^{-2}] \quad (4.28)$$

Where,  $a_0$  and  $a_1$  are empirical coefficients. Using the Ndabibi data set,  $a_0$  and  $a_1$  are computed to be  $0.1319 \text{ } ^\circ\text{C}^{-0.5}$  and  $-34.91 \text{ W m}^{-2}$  respectively; however, a wide scatter is observed between the modelled and the measured  $K_{\downarrow 24}$  values,  $R^2$  being 0.45. Hence, Eq. (4.28) is not recommended here.

#### Daily net longwave radiation ( $L_{n24}$ )

It can be estimated using Eq. (4.29). The derivation of the equation is described in Annex D.

$$L_{n24} = -\left(0.165 + 0.835 \frac{n}{N}\right) \varepsilon' \sigma T_a^4 \quad [\text{W m}^{-2}] \quad (4.29)$$

$$\varepsilon' = \left(0.34 - 0.14 \sqrt{e_a}\right) \quad [-] \quad (4.30)$$

Where,  $\varepsilon'$  is the net emissivity between the atmosphere and the ground, and  $e_a$  is the actual vapor pressure.

The above equations utilize  $n$ ,  $e_a$  and  $T_a$ , which are basically ground-based data. Since the purpose of this section is to minimize the dependency of formulations on ground-based data, other ways of formulating  $L_{n24}$  have been investigated as follows.

*Idso and Jackson* (1969) proposed that  $\varepsilon'$  can be directly solved from  $T_a$  using the following empirical relationship:

$$\varepsilon' = -0.02 + 0.261 \exp(-7.77 * 10^{-4} (T_a - 273)^2) \quad [-] \quad (4.31)$$

Comparison of Eq. (4.31) with Eq. (4.30) has been made in Fig. (4.4).

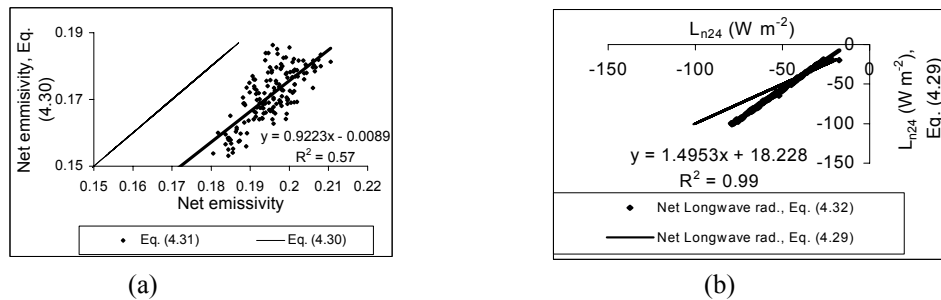


Fig. 4.4 (a) Comparison of  $\varepsilon'$  estimated using Eqs.(4.30) and (4.31), and (b) Scattergram between  $L_{n24}$  estimates made by Eqs. (4.29) and (4.32).

Fig. 4.4(a) shows that there is no a single intersection between  $\varepsilon'$  estimates made using Eqs. (4.30) and (4.31). Linear regression analysis has also been conducted between the two estimates, however, 43 % of the variation between the two estimates can not be statistically explained. Hence, it can be concluded that the Eq. (4.31) does not serve the purpose of Eq. (4.30).

Another empirical relationship which greatly reduces the need for ground-based data is that proposed by Slob (De Bruin, 1987):

$$L_{n24(slob)} = -110 \frac{K_{\downarrow 24}}{K_{\downarrow 24}^{TOA}} \quad [\text{W m}^{-2}] \quad (4.32)$$

Fig. 4.4(b) and Table 4.6 illustrate that  $L_{n24}$  values computed by the Slob equation are not in good agreement with the corresponding values obtained using Eq. (4.29). However, a linear regression between the two values yields  $L_{n24}$  estimates that are compatible with those obtained using Eq. (4.29). Using the obtained regression equation, the Slob equation has been modified as follows:

$$L_{n24} = -164.483 \frac{K_{\downarrow 24}}{K_{\downarrow 24}^{TOA}} + 18.228 \quad [\text{W m}^{-2}] \quad (4.33)$$

Table 4.6 Comparison of Eq. (4.32) against Eq. (4.29)

Statistical indicators	Slob's	Regression equation relating Eqs. (4.32) and (4.29)
	equation, Eq. (4.32)	$L_{n24} = 1.4953L_{n24(slob)} + 18.228$
E	0.84	-na-
R <sup>2</sup>	-na-	0.99
RMSE (W m <sup>-2</sup> )	10.38	1.55
MBE (W m <sup>-2</sup> )	-7.15	-0.10

RMSE and MBE refer to Root Mean Square Error and Mean Bias Error, respectively. See Annex A for formulations.

#### 4.5 Comparison of $K_c$ values estimated using the validated $K_c$ equation and FAO $K_c$ Table

Using the field data collected from 7 to 10<sup>th</sup> of October, the daily  $K_c$  values for the crops under study (squash, bean, and chilli) are calculated using the validated  $K_c$  equation, Eq. (4.22). For the same crop and atmospheric conditions, the tabulated  $K_c$  values are also taken from the FAO Table presented in Allen *et al.* (1996a). It is clear from Table 4.7 that the daily  $K_c$  values are almost constant over the considered four days, and the calculated  $K_c$  values over the bean field are close to the corresponding FAO  $K_c$  values, while over the squash and chilli fields, the calculated  $K_c$  values exceed the corresponding FAO values by about 15%.

Table 4.7 Daily  $K_c$  values obtained using the validated  $K_c$  equation and FAO  $K_c$  Table

Date	Squash		Bean		Chilli	
	Calculated $K_c$	FAO $K_c$	Calculated $K_c$	FAO $K_c$	Calculated $K_c$	FAO $K_c$
7-10-'98	1.10	0.95	1.12	1.15	1.21	0.80
8-10-'98	1.10	0.95	1.13	1.15	1.22	0.80
9-10-'98	1.10	0.95	1.12	1.15	0.88	0.80
10-10-'98	1.09	0.95	1.12	1.15	1.05	0.80

#### 4.6 Conditions under which the validated $K_c$ and $ET_c$ equations are expected to work

Based on limited spatial and temporal data, this study has come up with field validated  $K_c$  and  $ET_c$  equations. Some of the main prerequisite conditions under which the validated equations are expected to work are outlined below:

- i. The irrigated areas must be large enough so that the horizontal transfer of sensible heat is minimal. When irrigated small fields are surrounded by dry vegetation, the  $K_c$  and  $ET_c$  equations validated in this study are expected to fail;
- ii. The validated equations should be applied only to well-watered crops. If the crops are suffering from water deficit, the validated equations are not applicable. To envisage one of the possible reasons, Priestley-Taylor and Penman-Monteith equations are combined to yield the following formulation for the Priestley-Taylor  $\alpha$  parameter:

$$\alpha = \frac{1}{r_s + r_{av}} \left\{ \frac{\rho_a c_p (e_{a,sat} - e_a)(\Delta + \gamma)}{\Delta \gamma (R_n - G)} \right\} \quad [-] \quad (4.34)$$

In this study, the value of  $\alpha$  has been computed for minimal  $r_s$  (which holds true for well-watered crops), however, when plants are suffering from water shortage,  $r_s$  rises consequently affecting  $\alpha$ . The other reason is attributed to the fact that the radiation terms calculated for dry surface conditions are quite different from wet conditions, and therefore, they can not be used to estimate potential evapotranspiration.

#### 4.7 Sensitivity Analysis of $K_c$ parameters, on a daily scale

The sensitivity of  $K_c$  to various atmospheric and surface variables is studied by varying one of the variables, while keeping all the rest terms constant. The assumed reference values of these variables are:  $K_{\downarrow 24} = 150$  [ $W m^{-2}$ ],  $L_{n24} = -43.453$  [ $W m^{-2}$ ],  $\alpha_0 = 0.15$ . These values are taken from one of the daily field measurements. The variables have been changed by  $\pm 5\%$ ,  $\pm 15\%$ , and  $\pm 25\%$ . The sensitivities are computed using the equation:

$$S_x = \frac{(K_c - K_c^{ref})}{K_c^{ref}} * 100\% \quad [-] \quad (4.35)$$

Where,  $K_c$  is computed using the newly assumed values, and  $k_c^{ref}$  using the reference values.

Table 4.8 Sensitivity of  $K_c$  to various variables

Variable	Sensitivity of $K_c$ to variables with different changes					
	-25%	-15%	-5%	5%	15%	25%
$K_{\downarrow 24}$	3.59	1.70	0.47	-0.40	-1.04	-1.54
$\alpha_0$	6.69	4.02	1.34	-1.34	-4.02	-6.69
$L_{n24}$	2.54	1.42	0.44	-0.42	-1.18	-1.87

Table 4.8 shows that  $K_c$  is relatively more sensitive to changes in crop albedo. This reflects the fact that  $K_c$  depends more on crop parameters than on climatic variables. In general,  $K_c$  is fairly insensitive to the climatic variables. It should be noted here, however, that in such type of sensitivity study, surface and atmospheric layer feedback consequences are neglected.

Another noteworthy consideration is: the concept of varying a single variable, while keeping the rest terms constant, may give the impression that the constant values do not influence the sensitivity. However, this is not necessarily true. For instance, the sensitivity of  $K_c$  to  $\alpha_o$  changes when the constant  $K_{\downarrow 24}$  is kept low or high, whereas the sensitivity of  $K_c$  to  $K_{\downarrow 24}$  has nothing to do with the magnitude of the constant  $\alpha_o$ . Following are the arguments.

### Variables affecting sensitivity

Since sensitivity is a measure of the change in the dependent variable due to a change in one of the independent variables, it can be expressed in the form of a partial differential equation. Based on this idea, the following sensitivity equations are derived. Most of the equations show that the sensitivity of  $K_c$  to one of the variables is determined by the magnitudes of the so-called “constant terms”.

#### *Sensitivity of $K_c$ to $K_{\downarrow 24}$*

The sensitivity of  $K_c$  to  $K_{\downarrow 24}$ ,  $S_{K_{\downarrow 24}}$ , can be written as:

$$S_{K_{\downarrow}} = \frac{\partial K_c}{\partial K_{\downarrow}} = \frac{0.23L_{n24}}{(0.77K_{\downarrow 24} + L_{n24})^2} \quad [W^{-1} m^2] \quad (4.36)$$

From Eq. (4.36), it can be seen that the sensitivity is determined by  $L_{n24}$  and  $K_{\downarrow 24}$ . This means that the sensitivity of  $K_c$  to  $K_{\downarrow 24}$  is not actually the same when the constant  $L_{n24}$  is kept low or high.

#### *Sensitivity of $K_c$ to $\alpha_o$*

The sensitivity of  $K_c$  to  $\alpha_o$ ,  $S_{\alpha_o}$ , is given by:

$$S_{\alpha_o} = \frac{\partial K_c}{\partial \alpha_o} = \frac{-K_{\downarrow 24}}{(0.77K_{\downarrow 24} + L_{n24})} \quad [-] \quad (4.37)$$

Eq. (4.37) shows that  $S_{\alpha_o}$  is independent of  $\alpha_o$ , and it is determined by only the magnitudes of  $L_{n24}$  and  $K_{\downarrow 24}$ . This can also be seen from Table 4.8, which shows that a reduction of 25 % in  $\alpha_o$  and an increment of 25 % in  $\alpha_o$  result in equal sensitivity (regardless of the sign).

#### *Sensitivity of $K_c$ to $L_{n24}$*

The sensitivity of  $K_c$  to  $L_{n24}$ ,  $S_{L_{n24}}$ , is:

$$S_{L_{n24}} = \frac{\partial K_c}{\partial T_a} = \frac{(\alpha_o - 0.23)K_{\downarrow 24}}{(0.77K_{\downarrow 24} + L_{n24})^2} \quad [\text{W}^{-1} \text{m}^2] \quad (4.38)$$

The sensitivity is determined by  $L_{n24}$ ,  $K_{\downarrow 24}$ , and  $\alpha_o$ . For instance, if  $\alpha_o$  is greater than 0.23, higher  $\alpha_o$  value results in higher sensitivity than does lower  $\alpha_o$ .

#### 4.8 Comparison of $ET_{ref}$ equations (on a daily time scale): P-T vs. simplified empirical equations

Once  $K_c$  is solved, the next step to calculate  $ET_c$  is the computation of  $ET_{ref}$ . The P-T equation can be used to calculate  $ET_{ref}$ , however, the fact that the reference grass parameters are fixed may open the door for further simplification. This section examines the reliability of empirical equations, which use simple input data, to estimate  $ET_{ref}$ . The data used in this analysis are taken from the Ndabibi data set.

Equations to be tested for reliability:

(1) Modified Makkink:  $ET_{ref} = 0.65 \frac{\Delta}{\Delta + \gamma} K_{\downarrow 24}$  [W m<sup>-2</sup>] (4.41)

(2) Jensen-Haise:  $ET_{ref} = (0.025(T_{mean} - 273) + 0.08)K_{\downarrow 24}$  [W m<sup>-2</sup>] (4.42)

(3) Turc:  $ET_{ref} = 0.31 \frac{(T_{mean} - 273)}{(T_{mean} - 273) + 15} ((1 - 0.23)K_{\downarrow 24} + 2.09)$  [W m<sup>-2</sup>] (4.43)

(4) Hargreaves:  $ET_{ref} = 0.0023(T_{max} - T_{min})^{0.5} ((T_{mean} - 273) + 17.8)K_{\downarrow 24}^{TOA}$  [W m<sup>-2</sup>] (4.44)

The comparison between  $ET_{ref}$  estimates made using P-T equation and other simplified equations is presented in Fig. 4.5. The red line, in all the plots of Fig.4.5, represents the Priestley-Taylor  $ET_{ref}$  estimates. Table 4.9 shows the values of the statistical indicators of  $ET_{ref}$  values estimated using the simplified equations against Priestley-Taylor equation.

Table 4.9 Values of statistical indicators of  $ET_{ref}$  values estimated using P-T and other simplified equations. Note: 'RMSE' refers to Root Mean Square Error, and 'MBE' to Mean Bias Error.

Equation	MBE values (W m <sup>-2</sup> )		RMSE values (W m <sup>-2</sup> )	
	Equation	Regression between equation and P-T	Equation	Regression between equation and P-T
Modified Makkink	-13.35	0	13.41	2.62
Jensen-Haise	11.49	0	14.59	3.89
Turc	-45.06	0	42.02	3.47
Hargreaves	57.52	0	60.98	15.59

Examination of Fig. 4.5 and Table 4.9 reveals that the Modified Makkink and Jensen-Haise equations perform relatively better than Turc and Hargreaves equations, as judged from the lower RMSE and MBE values of the former two. Except for the Hargreaves equation, the  $ET_{ref}$  estimates made by P-T and the other equations deviate systematically, which is witnessed by the high  $R^2$  values.

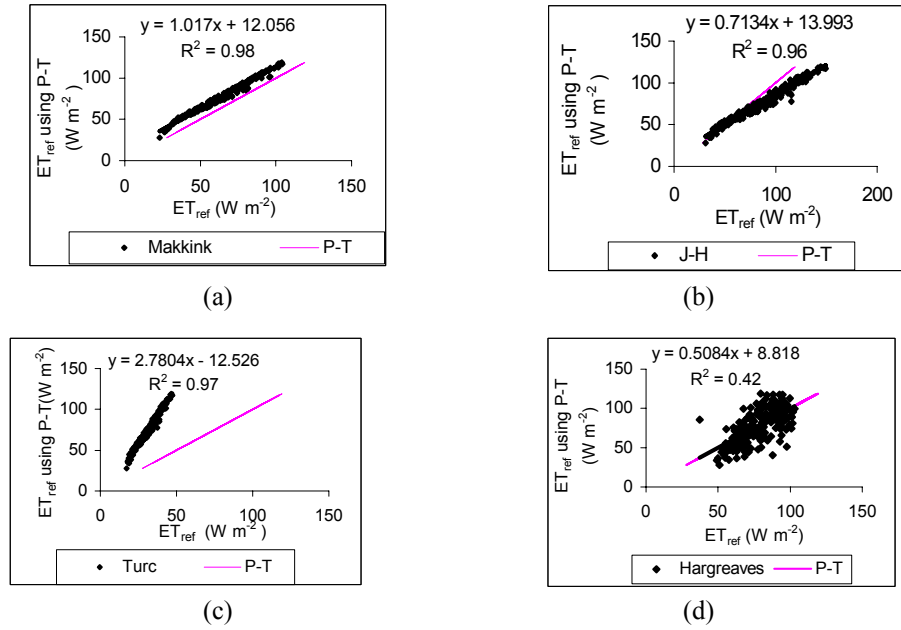


Fig. 4.5 Comparison between  $ET_{ref}$  estimates made using the Priestley-Taylor (P-T) and (a) Modified Makkink (b) Jensen-Haise, (c) Turc, and (d) Hargreaves equations. Number of data pairs used = 262.

### Further Simplification?

Using the daily air temperature data measured for 8 months, the corresponding mean and standard deviation of evaporative fraction are computed to be 0.863 and 0.0165, respectively. Using this mean value, the P-T equation is further reduced to:

$$ET_{ref} = 0.863R_{n24} \quad [W m^{-2}] \quad (4.45)$$

Fig. 4.6 demonstrates that  $ET_{ref}$  values estimated using the simplified equation are in excellent agreement with those estimated by full P-T equation.

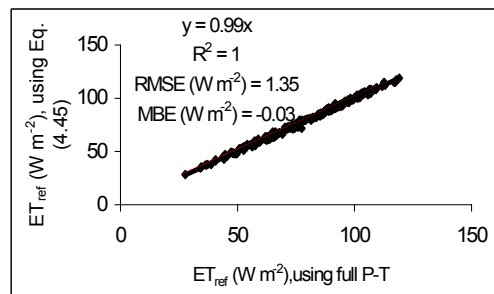


Fig. 4.6 Comparison between  $ET_{ref}$  estimates made using P-T and Eq. (4.45).

## 5.

### LANDSAT-TM and NOAA-AVHRR Applications

#### 5.1 LANDSAT-TM Application

##### 5.1.1 Data Acquisition

A LANDSAT-5 TM image, scene of Path 169 and Row 60, dated 21 January 1995 was acquired. The study area is covered in the lower quadrant of this scene. A subsection of this quadrant was selected for digital image analysis. This section is 44 km by 44 km in size. The preprocessing operations applied on this image are enumerated in Annex F.

##### 5.1.2 Delineating Irrigated Areas

A prerequisite to the application of the validated  $K_c$  and  $ET_c$  equations is that the relevant input data must be acquired from solely irrigated areas. Hence, delineation of irrigated areas is performed prior to the execution of the validated equations. Supervised classification, vegetation indices, and principal component methods have been widely used to detect irrigated areas. *Arai* (1992) and *Bastiaanssen* (1998) argue that the supervised classification method gives better accuracy than the rest. Hence, the supervised classification method is used here to discern irrigated areas from nonirrigated areas. A false color composite is made using TM bands 4, 3, and 2. The reason for selecting these bands is not because they result in the highest optimum index factor value than the rest combinations, rather it is because they are more suitable to detect irrigated areas. A training set is then made by carefully sampling pixels based on the spectral and spatial characteristics of the irrigated areas. Three units have been selected: irrigated areas, nonirrigated areas, and lake. The relevant spectral feature spaces are shown in Fig. 5.1.

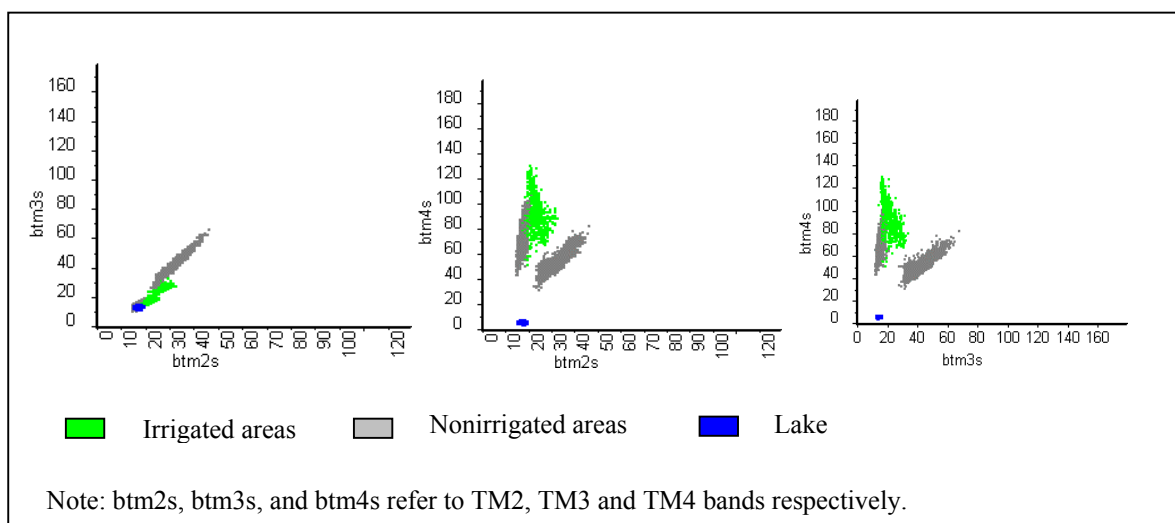


Fig. 5.1 Spectral feature space of multibands.

The Gaussian maximum likelihood classifier is then used to classify the image. To remove the “salt and pepper” appearance, a post classification 3 by 3 majority filter is run on the classified map. Visual inspection of the classified image shows that the swampy areas around the shore of the lake are not well identified. Therefore, two options of detecting the swampy areas have been considered. One is the use of temperature threshold limit (299 °C), and the other is screen digitizing of the shoreline. The application of both options yielded successful results.

To evaluate the accuracy of the classification result, random test pixels, which have not been used in the training phase, are selected. A kappa index is then applied to measure the accuracy. The kappa index (k) is formulated as (Fung and LeDrew, 1988):

$$k = \frac{P_0 - P_e}{1 - P_e} \quad [-] \quad (5.1)$$

Where,  $P_0$  is the proportion observed along the diagonal (in the error matrix),  $P_e$  is the proportion expected to have arisen by chance, and  $1 - P_e$  is the largest possible agreement for the given marginal totals.

Table 5.1 Error matrix of classification

Classified data \ “Ground truth” data	Irrigated pixels	Nonirrigated pixels	Total
Irrigated pixels	20104	265	20369
Nonirrigated pixels	124	17344	17468
Total	20228	17609	37837

$$p_0 = (20104 + 17344) / 37837 = 0.99, \quad p_e = 20228 * 20369 * 17609 * 17468 / 37837^4 = 0.06, \quad k = 0.99$$

The kappa index value,  $k = 0.99$ , shows that the result of the classification is acceptable. The delineated irrigated areas are depicted in Fig. 5.3. It should be noted here that since the classification is carried out mainly using spectral information, harvested areas are not classified as irrigated. The collection of time series image will improve the accuracy of the delineation. The total irrigated area delineated, as per Fig. 5.3, amounts to 35 Km<sup>2</sup>.

### 5.1.3 Estimating $K_c$ and $ET_c$ parameters, on an instantaneous time scale

#### Incoming shortwave radiation ( $K_{\downarrow}$ )

When the available data is only LANDSAT-TM, the estimation of  $K_{\downarrow}$  is possible through the calculation of atmospheric transmittance by a radiative transfer model. Two methods which utilize this concept are considered here.

Fig. 5.2 A False color composite image corresponding to the study area. Bands 4, 3, and 2 are displayed in red, green, and blue respectively.

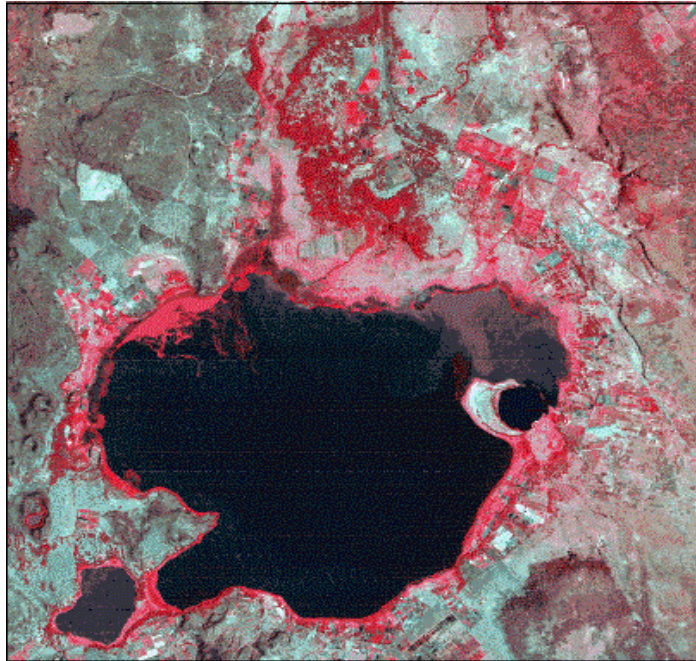
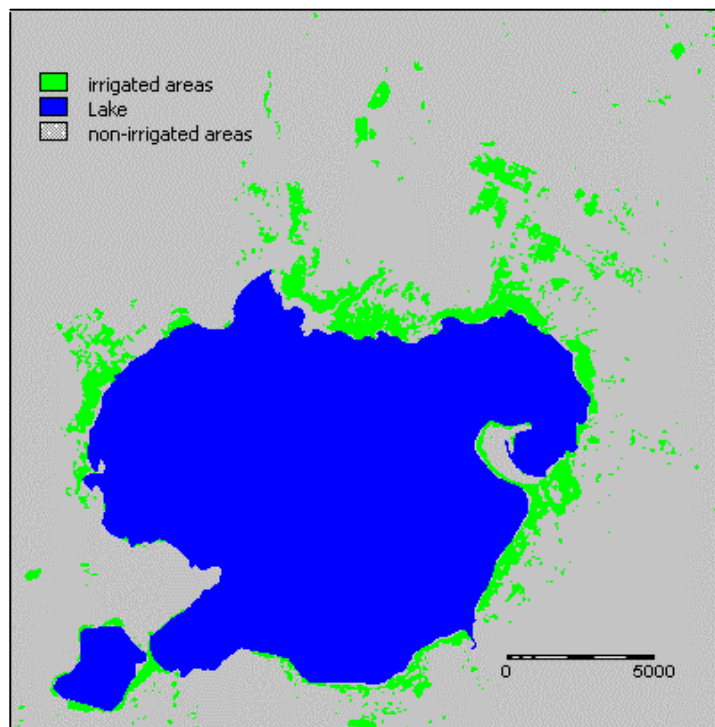


Fig. 5.3 Map showing the irrigated areas classified from the LANDSAT-TM imagery shown above.



(i) Slater's method

Slater (1980) suggested the following equation for estimating single-way transmittance in the shortwave range ( $\tau'_{sw}$ ):

$$\tau'_{sw} = e^{(-\tau'_{ext} \sec \theta_z)} \quad [-] \quad (5.2)$$

Where,  $\tau'_{ext}$  is the atmospheric vertical extinction optical depth, and  $\theta_z$  is the solar zenith angle. Using data collected in Botswana, Peters (1995) found an exponential relationship between  $\tau'_{ext}$  and percentage of cloud cover ( $\overline{\%CC}$ ):

$$\tau'_{ext} = 0.3545e^{\overline{\%CC}} \quad [-] \quad (5.3)$$

For the current image,  $\theta_z = 35.105^0$  (Annex E). Since the TM image was acquired under cloud free atmospheric condition,  $\overline{\%CC} \approx 100$ . Using these inputs in Eqs. (5.2) and (5.3) yields,  $\tau'_{sw} = 0.54$ .

(ii) Ahern's method

Ahern *et al.* (1977) extracted transmittance using the darkest object present in the scene in such a way:

$$\alpha_{inst} = \frac{r_p - r_{p \min}}{\tau''_{sw}} \quad [-] \quad (5.4)$$

Where,  $r_{p \min}$  is the lowest planetary albedo of all the pixels, being usually an area with a negligible small surface albedo and  $\tau''_{sw}$  is the two-way transmittance for broadband solar radiation. For the current image, the two-way transmittance has been estimated by assuming the surface albedo of lake Naivasha to be 0.06, which yields a calibration of  $\tau''_{sw} = 0.35$  at  $r_{p \min} = 0.01$ , implying that  $\tau'_{sw} = 0.59$ . The transmittance values calculated by the above two methods vary within 8 % from eachother.  $\tau'_{sw} = 0.59$  is used for further analysis.

The shortwave radiation reaching the earth's surface ( $K_{\downarrow}$ ) can be written as:

$$K_{\downarrow} = \tau'_{sw} K_{\downarrow}^{TOA} \quad [W \ m^{-2}] \quad (5.5)$$

Where,  $K_{\downarrow}^{TOA}$  is the extraterrestrial solar radiation. The formulation for  $K_{\downarrow}^{TOA}$  is described in Annex E. For date: 21 January, satellite overpass time: 9:45 a.m., and latitude:  $0^0 48' 19.22''$ , the calculated radiation parameters are given in Table 5.2. For  $\tau'_{sw} = 0.59$ , Eq. (5.5) yields:  $K_{\downarrow} = 677.35 \ W \ m^{-2}$ .

Table 5.2 Calculated radiation parameters for LANDSAT-TM image dated 21 Jan '95

Day angle [rad]	0.3443	Solar zenith angle [degree]	35.105
Equation of time [minutes]	15	Eccentricity correction factor [-]	1.033
Local apparent time [hour]	10:00	Declination [rad]	-0.351
Solar hour angle [degree]	30	$K_{\downarrow}^{TOA}$ [W m <sup>-2</sup> ]	1148.05

Surface albedo ( $\alpha_{inst}$ )

The derivation of crop surface broadband albedo ( $\alpha_{inst}$ ) is fully described in Annex F. Suffice is here to mention that  $\alpha_{inst}$  is calculated using the equation:

$$\alpha_{inst} = 2.86r_p - 0.03 \quad [-] \quad (5.6)$$

Where,  $r_p$  is the radiometrically corrected planetary broadband surface albedo. Using the above equation,  $\alpha_{inst}$  values have been calculated for the irrigated areas. It is learnt from the histogram that the mean and standard deviation of  $\alpha_{inst}$  are 0.20 and 0.05, respectively. Consultation of literature reveals that the range of calculated  $\alpha_{inst}$  values sounds reasonable.

NDVI

NDVI at the top of atmosphere ( $NDVI^{TOA}$ ) is expressed as:

$$NDVI^{TOA} = (r_p(4) - r_p(3)) / (r_p(4) + r_p(3)) \quad [-] \quad (5.7)$$

Here, the numbers in brackets indicate the TM band number. Despite the fact that it is called “normalized”, NDVI is affected by some factors. One of the factors that influence NDVI is the atmospheric interference. *Goward et al.* (1991) and *Carlson and Ripley* (1997) fitted a linear relationship between  $NDVI^{TOA}$  and NDVI at the surface, however, they reported different empirical coefficients:

$$NDVI = aNDVI^{TOA} + b \quad [-] \quad (5.8)$$

Table 5.3 NDVI atmospheric correction coefficients

Authors	Abbre.	a	b	Remarks
Goward et al. (1991)	G1	1.1	0.11	For atmosphere having low aerosol
Goward et al. (1991)	G2	1.2	0.12	For atmosphere having high aerosol
Carlson and Ripley (1997)	C&R	1.008	-0.043	

The coefficients suggested by C&R imply that  $NDVI < NDVI^{TOA}$ , while the reverse is obtained using the coefficients given by G1 and G2. This may dictate the necessity of local calibration. Moreover, it is also felt that the coefficients must take into account the viewing angle conditions. It therefore seems that there is still a problem of atmospheric correction for NDVI. The coefficients reported by C&R are used in this study.

*Surface emissivity ( $\epsilon_0$ )*

*Van de Griend and Owe* (1993) performed a large series of emissivity measurements together with spectral reflectance measurements in the red and near-infrared portion of the electromagnetic spectrum. They found a good statistical relationship between the measured emissivity and NDVI resulting in a correlation of  $r^2 = 0.92$  and a standard deviation of less than 0.007, using 59 observations.

$$\epsilon_{8-14} = 1.009 + 0.047 \ln(NDVI) \quad [-] \quad (5.9)$$

Here,  $\epsilon_{8-14}$  is the surface emissivity in the spectral range of 8 to 14 $\mu\text{m}$ . *Peters* (1995) applied Eq. (5.9) successfully to satellite NDVI images of various spatial resolutions in Botswana. Since the variation between  $\epsilon_{8-14}$  and  $\epsilon_0$  is insignificant within the order of magnitude of the net radiation estimation (*Llasat and Synder*, 1998), it is assumed that  $\epsilon_{8-14} = \epsilon_0$ . Water bodies with negative NDVI values are assumed to have a value of  $\epsilon_0 = 1$ .

*Atmospheric emissivity ( $\epsilon_a$ )*

For cloud free conditions, both theoretical (e.g. *Sugita and Brutsaert*, 1993) and empirical (e.g. *Idso*, 1983) expressions exist for the determination of  $\epsilon_a$ . *Hatfield et al.* (1983) used hourly data from 15 locations at various latitudes and heights above mean sea level to compare expressions from *Brunt* (1932), *Swinbank* (1963), *Brutsaert* (1975), *Idso and Jackson* (1969), and *Idso* (1983). They found that models that included vapor pressure performed best. However vapor pressure data at the time of satellite overpass was not available. In its absence, *Bastiaanssen* (1995) suggested the use of the following empirical equation which relates  $\epsilon_a$  to transmittance in the shortwave range:

$$\epsilon_a = 1.08(-\ln \tau'_{sw})^{0.265} \quad [-] \quad (5.10)$$

Substitution of  $\tau'_{sw} = 0.59$  in Eq. (5.10) yields,  $\epsilon_a = 0.91$ .

*Air temperature ( $T_a$ )*

Since  $T_a$  monitoring network is absent, the only remaining option is to derive it from surface temperature. In the field, it was observed that at about 10:00 local time,  $T_0 - T_a \approx 2 \text{ }^\circ\text{C}$ , over irrigated areas. Therefore, a geometrical gradient of constant temperature, i.e.  $1 \text{ }^\circ\text{C m}^{-1}$ , is assumed.

*Surface temperature ( $T_o$ )*

The radiance measured by the LANDSAT-TM thermal band 6 at the top of the atmosphere ( $L_6^{TOA}$ ) can be written as:

$$L_6^{TOA} = L_6^{surf} \tau_6 + L_{6\uparrow}^{atm} \quad [\text{W m}^{-2}] \quad (5.11)$$

Where,  $\tau_6$  is the atmospheric transmittance and  $L_6^{atm}$  is the upwelling atmospheric radiance, all in TM band 6 wavelength range.

$$L_6^{surf} = \varepsilon_6 B_6(T_0) + (1 - \varepsilon_6)L_{6\downarrow} \quad [W \text{ m}^{-2}] \quad (5.12)$$

Where,  $B_6(T_0)$  is the radiance computed using the Planck equation for a brightness temperature  $T_0$ , and  $L_{6\downarrow}$  is the downwelling atmospheric radiance, all in TM band 6 wavelength range.

An inversion of the Planck equation gives the following formulation for  $T_0$ :

$$T_0 = 1251.12 / \ln[(3720.38 / L_6^{suremi}) + 1] \quad [^{\circ}\text{C}] \quad (5.13)$$

Where,  $L_6^{suremi}$  is the emitted longwave radiation within the wavelength range of TM band 6. To compute  $T_0$  for each pixel,  $\tau_6$  and  $L_{6\uparrow}^{atm}$  must be solved. Usually  $\tau_6$  and  $L_{6\uparrow}^{atm}$  are determined from atmospheric radiation transfer models or from field measurements of  $T_0$  at the time of satellite overpass. Owing to the absence of field measured surface temperature data, a trial and error procedure, as suggested by *Farah and Bastiaanssen* (1998), has been applied to obtain reasonable  $T_0$  values. Results indicate that  $T_0$  ranges at a pixel scale from 24 to 40  $^{\circ}\text{C}$ , Lake Naivasha being 24.8  $^{\circ}\text{C}$ .

#### *Daily surface albedo, $\alpha_0$*

As the name implies,  $\alpha_0$  is the mean of representative daytime  $\alpha_{inst}$  values. Since  $\alpha_{inst}$  values are only available for one time in a day from LANDSAT-TM data, the extrapolation of  $\alpha_{inst}$  to  $\alpha_0$  remains necessary. *Farah and Bastiaanssen* (1998) suggest that  $\alpha_0 \approx 1.1\alpha_{inst}$  for LANDSAT-TM pass at 9:45 local time. However, *Llasat and Snyder* (1998) argue that the cloudiness condition must be taken into account while extrapolating. Because of lack of a better formulation, it is assumed that  $\alpha_0 = 1.1\alpha_{inst}$ .

#### *Mapping $K_c$ on an instantaneous time scale*

In the preceding sections,  $\varepsilon_a$ ,  $\varepsilon_o$ ,  $\alpha_{inst}$ ,  $\alpha_0$ ,  $T_0$ ,  $T_a$ ,  $K_{\downarrow}$ , and NDVI have been calculated. To solve  $K_c$  by means of Eq. (4.18), the required input data are:  $K_{\downarrow}$ ,  $K_n$ ,  $L_n$ , and  $G$ . The formulations required to solve these input parameters are indicated below:

$$K_n = f(K_{\downarrow}, \alpha_{inst}) \longrightarrow \text{Eqs. (2.5) and (4.5)}$$

$$L_n = f(\varepsilon_a, T_0, T_a) \longrightarrow \text{Eq. (4.23)}$$

$$G = f(T_0, \text{NDVI}, \alpha_0, \alpha_{inst}) \longrightarrow \text{Eq. (4.4)}$$

Applying Eq. (4.18), the resulting  $K_c$  map and its histogram are displayed in Figs. 5.4 and 5.6.

Fig. 5.4 Crop coefficient ( $K_c$ ) map corresponding to the area of study calculated by using Eq. (4.18). This map is obtained for the LANDSAT-TM image corresponding to the 9:45 hour local time of 21 January 1995. The white color corresponds to non-irrigated areas.

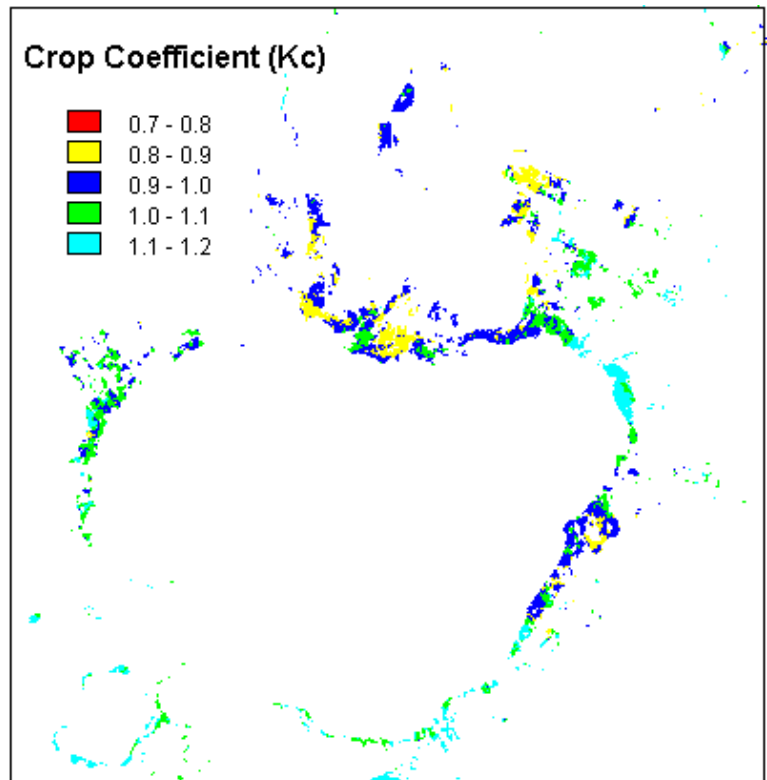
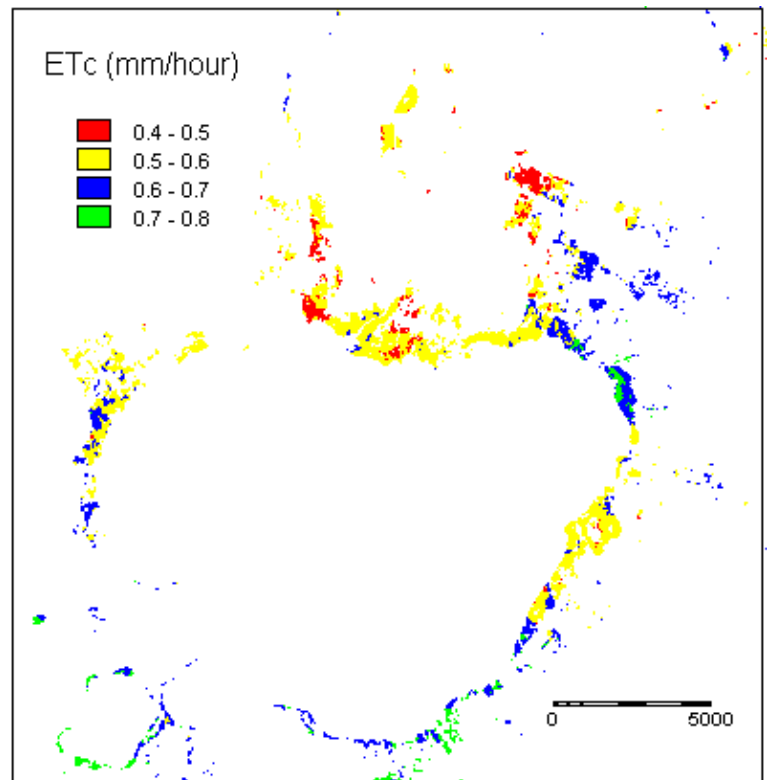


Fig. 5.5 Crop potential evapotranspiration ( $ET_c$ ) map corresponding to the area of study calculated by using P-T equation. This map is obtained for the LANDSAT-TM image corresponding to the 9:45 hour local time of 21 January 1995. The white color corresponds to non-irrigated areas.



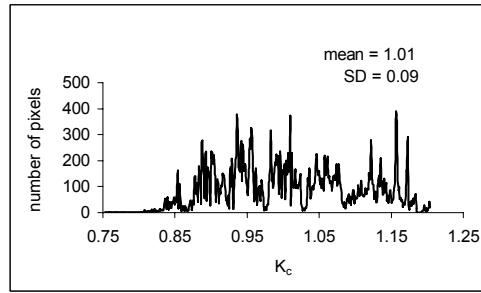


Fig. 5.6 Histogram of  $K_c$  on an instantaneous time scale, based on the LANDSAT-TM data of 9: 45 hour local time of 21 January 1995.

### Mapping $ET_c$ on an instantaneous time scale

Except the term ' $\Delta/(\Delta+\gamma)$ ', all the other parameters required to calculate  $ET_c$  as per Eq. (4.20) have been solved in the preceding sections. The term ' $\Delta/(\Delta+\gamma)$ ' is exclusively a function of air temperature, and it is solved using Eqs. (4.7) and (4.9). The unit of  $ET_c$  is converted from  $W\ m^{-2}$  to  $mm\ hr^{-1}$  using latent heat of vaporization (Eq. 4.10). The resulting  $ET_c$  map is depicted in Fig. 5.6. It is learnt from the histogram of  $ET_c$  that its mean and standard deviation are 0.58 mm/hour and 0.07 mm/hour, respectively.

### $K_c$ in relation to other state variables

Table 5.4 Correlation ( $r$ ) between  $K_c$  and other state variables

State variables	$r$
Crop albedo	-0.967
Surface temperature	-0.621
NDVI	-0.014

Table 5.4 shows that the spatial differences of  $K_c$  are strongly linked to crop albedo and surface temperature than to NDVI. Choudhury *et al.* (1994) explains that uncertainties in relating  $K_c$  to NDVI can arise from variabilities in soil, crop, and atmospheric characteristics, being confirmed from Table 5.4. In fact, it can also be inferred from Eq. (4.18) that  $K_c$  is a strong function of albedo and surface temperature. Some studies have reported that  $K_c$ , for a certain crop, is related to its NDVI (e.g. Neale *et al.*, 1996). The result of this study does not contradict such results for the simple reason that only spatial variation, not temporal variation, is considered in filling up Table 5.4.

Based on the produced maps, it is also attempted to develop an empirical equation relating  $K_c$  to albedo and surface temperature [ $^{\circ}C$ ], the resulting first order equation ( $R^2 = 0.91$ , RMSE = 0.038) reads:

$$K_c = -1.436\alpha_{inst} - 0.005T_0 + 1.459 \quad [-] \quad (5.14)$$

It can be seen in Eq. (5.14) that the signs of the coefficients  $\alpha_0$  and  $T_0$  are both negative, implying that  $K_c$  is inversely related to them.

### 5.1.4 Estimating $K_c$ and $ET_c$ parameters, on a daily time scale

Daily incoming shortwave radiation ( $K_{\downarrow 24}$ )

$K_{\downarrow 24}$  can be expressed as:

$$K_{\downarrow 24} = \tau'_{sw24} K_{\downarrow 24}^{TOA} \quad [W \text{ m}^{-2}] \quad (5.15)$$

Where,  $\tau'_{sw24}$  is the daily single-way transmittance in the shortwave range, and  $K_{\downarrow 24}^{TOA}$  is the daily extraterrestrial solar radiation. The formulation of  $K_{\downarrow 24}^{TOA}$  is outlined in Annex E. For date: 21 Jan. 1995, and latitude:  $0^{\circ} 48' 19.22''$ ,  $K_{\downarrow 24}^{TOA} = 431.02 \text{ W m}^{-2}$ . Since neither transmittance nor sunshine hour data is available, an attempt is made to see if it is possible to derive  $\tau'_{sw24}$  from  $\tau'_{sw}$ , since the latter is already known. The instantaneous transmittance values at the time of LANDSAT overpass are compared with the daily values, using the Ndabibi data set (which covered another period of time), in Fig. 5.7.

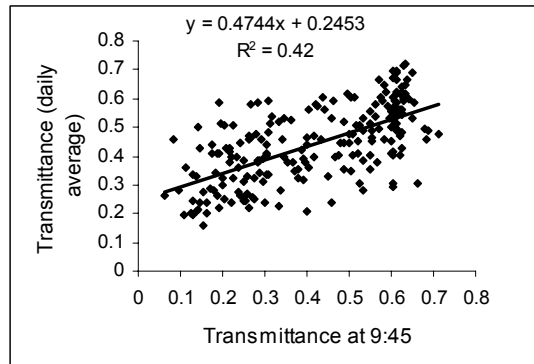


Fig. 5.7 Comparison of  $\tau'_{sw}$  at 9:45 and  $\tau'_{sw24}$

It can be seen from Fig. 5.7 that although  $\tau'_{sw}$  and  $\tau'_{sw24}$ , in general, follow similar trends, the relationship between the two is not adequate to predict values from one another. For instance, for  $\tau'_{sw} = 0.59$ , the figure shows that  $\tau'_{sw24}$  values can vary from 0.28 to 0.66. One way of reducing the scatter could be to segment the transmittance values using the cloudiness information obtained at 13:40. This specific time is chosen in light of the fact that the cloudiness information at this time can be obtained from public domain NOAA-AVHRR data. This technique could not be employed here in lack of NOAA-AVHRR data, for date 21 Jan. 1995, on Internet.

Another possible way of segmentation is by use of months. Since January has the least cloud cover (Fig. 3.2), the maximum value from the aforementioned  $\tau'_{sw24}$  range, i.e. 0.66, seems a plausible assumption. This yields,  $K_{\downarrow 24} = 284.473 \text{ W m}^{-2}$ .

Daily net shortwave radiation ( $K_{n24}$ )

$K_{n24}$  is given by:

$$K_{n24} = (1 - \alpha_0)K_{\downarrow 24} \quad [\text{W m}^{-2}] \quad (5.16)$$

The method of obtaining  $\alpha_0$  has been addressed in Section (5.1.3).

*Daily net longwave radiation ( $L_{n24}$ )*

$L_{n24}$  is solved using the modified Slob equation as depicted in Eq. (4.33). In this equation  $K_{\downarrow 24}$  and  $K_{\downarrow 24}^{TOA}$  are required as inputs. For  $K_{\downarrow 24} = 284.473 \text{ W m}^{-2}$ , and  $K_{\downarrow 24}^{TOA} = 431.02 \text{ W m}^{-2}$ ,  $L_{n24} = -90.33 \text{ W m}^{-2}$ .

*Mapping  $K_c$  on a daily time scale*

All the parameters required to solve Eq. (4.22) are computed in the preceding sections. The resulting  $K_c$  map is displayed in Fig. 5.8. The mean and standard deviation of  $K_c$  are computed to be 1.02 and 0.13, respectively. According to the  $K_c$  Table prepared by Doorenbos and Pruitt (1977), the obtained  $K_c$  range indicates “full-cover” crops.

*Mapping  $ET_c$  on a daily time scale*

All the parameters which are required to solve Eq. (4.20) have been worked out in the foregoing sections. The resulting  $ET_c$  map is displayed in Fig. 5.9. The mean and standard deviation of  $ET_c$  are computed to be 4.46 mm/day and 0.56 mm/day, respectively. The mean  $ET_c$  value is compared with the average pan evaporation data for January 21<sup>st</sup> collected in the Naivasha Meteorological station which is located about 3 km from the study area. The average pan evaporation for this date, for a duration of 1958 to 1991, is computed to be 5.46 mm/day, which results in a pan coefficient of 0.82 when compared to the  $ET_c$  computed from LANDSAT-TM. The obtained pan coefficient seems an acceptable value.

**5.1.5 Comparison of Instantaneous and Daily Estimates**

**Temporal variability of  $K_c$**

In the previous sections,  $K_c$  maps have been produced for two cases: (1) at 9:45 local time, and (2) on a daily basis. To be able to determine the variations of  $K_c$  in terms of ranges of percentages, the  $K_c$  values are sliced into classes having uniform widths of 0.05 and 0.10. The resulting sliced  $K_c$  maps are then crossed with the  $K_c$  map obtained for  $\tau'_{sw24} = 0.66$ , after which confusion matrices are calculated. The comparison of the two maps, which is depicted in Table 5.5, shows that in about 90 % of the cases, the difference between  $K_c$ 's at 9:45 and daily ones is within 10 %. It seems that  $K_c$  is not highly temporally unstable. From remote sensing perspective, this is another big advantage of  $K_c$  over the ‘Penman-Monteith’s resistance’ approach. Since the parameters involved in the latter approach are highly temporally unstable, even if all the required ground-based data are collected during the satellite overpass time, extrapolation of these parameters to daily totals is difficult.

Fig. 5.8 Crop Coefficient ( $K_c$ ) map on a daily basis calculated by using Eq. (4.22). This map is obtained for 21 January 1995. The white color corresponds to non-irrigated areas.

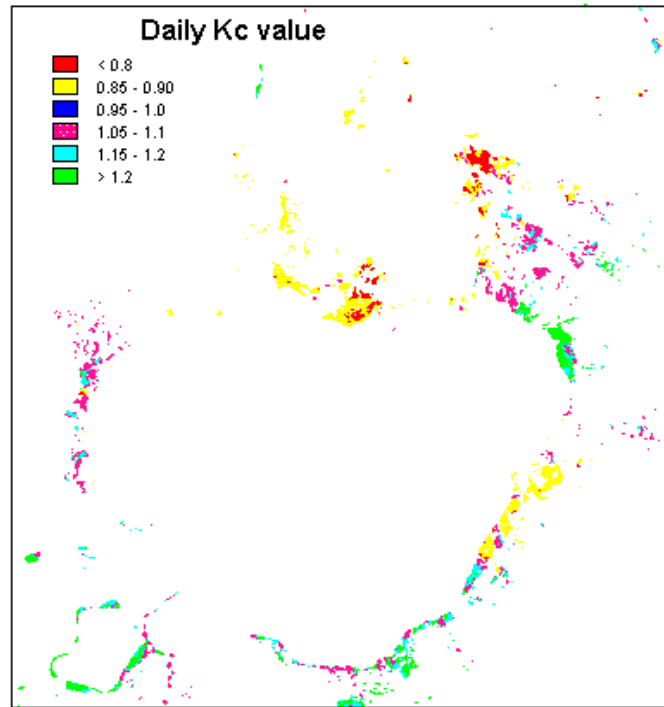


Fig. 5.9 Crop potential evapotranspiration ( $ET_c$ ) map for 21 January 1995. The white color corresponds to non-irrigated areas.

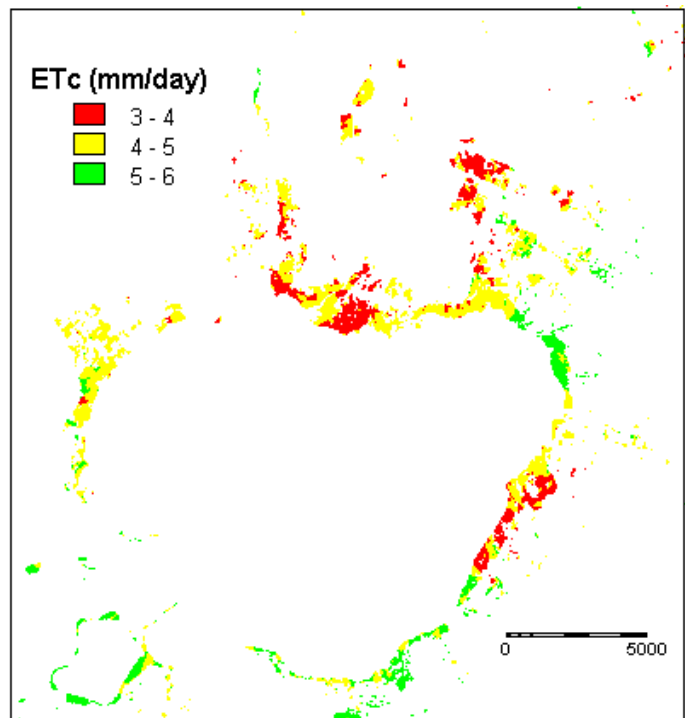


Table 5.5 Results of the confusion matrices comparing  $K_c$  at 9:45 with daily value for two cases of  $K_c$  class widths: (a) 0.05, and (b) 0.10

	$K_c$ class width	
	0.05	0.10
Average accuracy (%)	38.37	89.28
Average reliability (%)	35.79	79.79
Overall accuracy (%)	48.73	88.71

Average accuracy is calculated as the sum of the fraction of the correctly matching pixels for each  $K_c$  class (of  $K_c$  at 9:45) divided by the number of  $K_c$  classes, average reliability is calculated as the sum of the fraction of the correctly matching pixels for each  $K_c$  class (of  $K_c$  on a daily basis) divided by the number of  $K_c$  classes, and overall accuracy is calculated as the sum of all correctly matching pixels (diagonal elements) divided by the total number of pixels, but all are converted to percentages afterwards.

### ET<sub>c</sub>: Instantaneous vis-à-vis daily

Comparison of the instantaneous ET<sub>c</sub> with the daily ET<sub>c</sub> reveals that,

$$ET_{c(daily)} \cong 0.78ET_{c(inst)} \quad [\text{mm day}^{-1}] \quad (5.17)$$

The additional *inst* subscript represents characteristic values at instantaneous time (in this case at 9:45) and the additional *daily* subscript represents the same but for integrated daily. The formula from Jackson *et al.* (1983), which relates the temporal trend of solar radiation throughout the daylight period with the latent heat flux, reads as:

$$ET_{c(daily)} = ET_{c(inst)} \{2N / [\pi \sin(\pi t_i / N)]\} \quad [\text{mm day}^{-1}] \quad (5.18)$$

Where, N is the day length and  $t_i$  is the time starting at sunrise. For mid-morning and for this time of the year, the values of N and  $t_i$  yield:

$$ET_{c(daily)} = 0.90ET_{c(inst)} \quad [\text{mm day}^{-1}] \quad (5.19)$$

Eq. (5.19) assumes that the ratio between instantaneous- and daily solar radiation is equal to the ratio between instantaneous- and daily evapotranspiration. This assumption is proved to overestimate ET<sub>c(daily)</sub> by 15 %, when compared to Eq. (5.17).

#### Comments on the operational applicability of TM

One should be aware that the determination of time series  $K_c$  and ET<sub>c</sub> from LANDSAT-TM requires cloud-free images. However, such cloud-free images are not always available and this is especially true in the wet seasons. Moreover, the cost incurred in acquiring TM images is usually prohibitive.

## 5.2 NOAA-AVHRR Application

### 5.2.1 Introduction

High temporal resolution coupled with low cost of data acquisition make the NOAA-AVHRR data suitable for evapotranspiration studies at a sufficiently large scale.

When the size of the irrigation scheme considered is small, like that of the study area, the adequacy of the NOAA-AVHRR data is questioned. Especially, this problem becomes very serious when an attempt is made to map  $K_c$  and  $ET_c$  because the data demanded in either case must fully represent irrigated areas. In other words, the knowledge of the proportion of nonirrigated areas within the pixel size of NOAA-AVHRR can lead to a judgement whether the demands can fully be met by AVHRR.

#### Data Acquisition

NOAA-AVHRR data is available free of costs on Internet. This global data set consists of 10-day composites, for the period between April 1992 to October 1993 and February 1995 to May 1996. The available channels and the method of compositing are described in Annex G. The relevant channels (or bands) are downloaded for the period between February 1995 and January 1996.

### 5.2.2 Proportion of irrigated areas within the pixel size of NOAA-AVHRR

To determine the proportion of irrigated areas within the pixel size of NOAA-AVHRR, one of the considered options is the fractional vegetation cover approach. According to *Choudhury et al.* (1994), the fractional vegetation cover ( $V_c$ ) can be expressed as:

$$V_c = \frac{(SAVI - SAVI_s)}{(SAVI_d - SAVI_s)} \quad [-] \quad (5.20)$$

Where, the subscripts s and d refer to soil without vegetation and dense canopy, respectively.

$$SAVI = \frac{1.5(NIR - VIS)}{NIR + VIS + 0.5} \quad [-] \quad (5.21)$$

Here, VIS and NIR are the reflectance in the visible and near-infrared ranges, respectively. It is learnt from the SAVI map produced for one of the AVHRR images and the false color composite of the LANDSAT-TM image that the landuse/landcover in the vicinity of the irrigated plots is not mostly bare, rather it is rainfed agriculture or shrubs and trees. This implies that the fractional vegetation cover, if applied to AVHRR data, does not indicate the proportion of irrigated areas. Moreover, since different crop types are likely to be encompassed by a single AVHRR pixel, it is difficult to assign the appropriate values of  $SAVI_d$  and  $SAVI_s$ .

The other considered option is the blowing up of the pixel size of LANDSAT-TM imagery to that of NOAA-AVHRR. First, the map showing the irrigated areas classified using the LANDSAT-TM imagery is taken as the base map. All the irrigated pixels identified on this base map are given a DN value of 255, while all the rest pixels receive a DN value of 0. This map is then aggregated and resampled to a size of 1.1 km by 1.1 km, a spatial resolution that can be obtained from NOAA-AVHRR at nadir view. From this image, pixels that have high DN values are selected in such a way that their total area amounts to about 35 Km<sup>2</sup>, which is the size of the total irrigated area delineated on the base map. The resulting map shows that the DN

values observed over the irrigated areas vary from 79 to 118. The ratio of these DN values to 255, then, yields the proportion of irrigated areas within the pixel size of 1.1 km by 1.1 km. Applying this technique, the proportion of irrigated area within the pixel size of 1.1 km by 1.1 km is computed to be within the range of 31 % to 58 %. These values are the maximum that can be expected at nadir view condition. The actual proportion is, in fact, usually less than the computed one, due to the high possibilities of off-nadir viewing conditions. *Gutman* (1991) shows that close-to-nadir observations occur not more often than four times a month. Moreover, to be selected, these observations have to be cloud- and haze free. The off-nadir angle ( $\phi_{view}$ ) can be directly calculated from the satellite zenith angle (channel 7) using the following trigonometric relationship:

$$\sin \phi_{view} = \frac{\sin \phi_s}{[1 + H / R]} \quad [-] \quad (5.22)$$

Where,  $\phi_s$  is the satellite zenith angle, H is the satellite altitude ( $\approx 850$ km), and R is the radius of the earth ( $\approx 6370$  km). Table 5.6 shows that the possibility of having cloud-free near-nadir viewing conditions ( $\phi_{view} < 20^0$ ), in a 10-day-composite data set, is 1/12.

From the above discussion, it can be concluded that the proportion of nonirrigated areas within the pixel size of NOAA-AVHRR is so significant that the pixel can not be treated as a homogeneous irrigated area.

Table 5.6 The satellite-target geometry under clear sky conditions

Month	Average off-nadir angle [deg] during decades:			Month	Average off-nadir angle [deg] during decades:		
	1	2	3		1	2	3
February	-42,	-47	-25	August	31	-24	33
March	37	30	30	September	23	-15	-37
April	35	-46	-41	October	31	-37	-40
May	-33	-31	-43	November	48	37	40
June	24	-20	29	December	34	48	-43
July	-15	40	-29	January	-42	-8	-34

*Possible solutions?*

One of the prerequisite conditions to implement the validated  $K_c$  and  $ET_c$  equations is that the remote sensing input data must represent solely irrigated areas. However, the foregoing section proves that the pixel size of AVHRR contains largely nonirrigated areas. Is there any possible way of applying the validated equations to partly irrigated areas?

*(i) Spatial extrapolation of  $K_c$*

The famous  $K_c$  curve, developed by *Doorenbos and Pruitt* (1977), reveals that  $K_c$ , in time dimension, is mainly a function of the vegetal cover of irrigated plants. Can the same concept be extended to the space dimension? The first challenge stems from the difficulty in mapping the vegetal cover of irrigate plants ( $V_{c,irr}$ ) from AVHRR. Had the nonirrigated areas been mainly bare fields,  $V_{c,irr}$  would have been approximated as

$V_c$ , unfortunately, the presence of considerable nonirrigated vegetal cover poses difficulty in mapping  $V_{c,irr}$ . Another challenge is the setting of  $K_c$  values for extrapolation, namely,  $K_c$  for bare soil ( $K_s$ ), and  $K_c$  for dense canopy ( $K_d$ ).  $K_s$  can be assumed to be 0.05 (Allen *et al.*, 1996b), however, in the absence of a single pixel representing fully irrigated areas, the estimation of  $K_d$  becomes difficult. One may suggest that the  $K_d$  value obtained from the corresponding low resolution image (e.g. LANDSAT-TM) may be used. But in this case, the necessity of using AVHRR, if the low resolution image can serve the purpose, is questioned. Moreover, if there are different crop types in the area, it becomes even more difficult to assign appropriate  $K_d$ .

### (ii) The spatial decomposition approach

This deals with the generation of the relevant remote sensing input data required for  $K_c$  calculation, but on a subpixel basis. Over the past years, physical, mathematical, and geometrical models have been developed to decompose a mixed pixel to its pure subpixels (Boardman, 1993). The inputs of all these models consist of either the radiance values of some pure pixels or *a priori* knowledge on the proportion of subpixels for some of the pixels. The absence of lower resolution data on the same date coupled with the lack of homogeneous irrigated pixels in the NOAA-AVHRR data make the decomposition of NOAA-AVHRR pixels difficult. Moreover, in this approach individual signatures of components are assumed constant over the region, which is not true in heterogeneous command areas..

From the discussion raised in the preceding section, it can be concluded, unfortunately, that for small scale irrigated areas, like that of the study area, the application of NOAA-AVHRR image is not feasible to determine  $K_c$  and  $ET_c$ . The reason is attributed to the significant proportion of heterogeneous nonirrigated areas within the pixel size of NOAA-AVHRR.

### 5.2.3 NOAA-AVHRR Application to Large Scale Irrigation Schemes

To demonstrate the procedures which ought to be followed while applying the validated equations, part of the study area, 19 km by 27 km in size, is assumed to be fully irrigated excluding the Lake. The last dekadal image of May 1995 is downloaded from Internet for analysis. The preprocessing operations applied on this image are described in details in Annex G.

#### Estimating $K_c$ and $ET_c$ parameters, on a daily time scale

The formulations stated in Sections (5.1.3) and (5.1.4), except for albedo and surface temperature, are also applicable to AVHRR. This section discusses the methods for estimating albedo and surface temperature from NOAA-AVHRR.

#### *Surface albedo*

Daily average surface albedo ( $\alpha_0$ ) can be calculated using the following three steps: (i) atmospheric correction of narrow-band albedo, (ii) extension of narrow- to broadband albedo, and (iii) extension of instantaneous broadband albedo to daily. The

atmospheric correction of narrow-band albedo is carried out using the Paltridge and Mitchell model, as described in Annex G.

*Extension of Narrow- to Broadband albedo*

Because the AVHRR scanners measure reflectance in a few narrow-band channels, a conversion is needed so that these data may be used to estimate the broadband albedo. In previous work, linear relations between planetary narrow- and broadband albedo were developed (*Li and Leighton, 1992; Wydick et al. 1987*), however, for retrieving surface albedo, the same coefficients can not be used because the atmosphere attenuates the radiance in the visible- and infrared bands differently.

$$\alpha_{inst} = a_1VIS + a_2NIR + a_3 \quad [\%] \quad (5.23)$$

Here, *VIS* and *NIR* are expressed in percentages. Reported values for  $a_1, a_2,$  and  $a_3$  are tabulated in Table 5.7. It is noted from this Table that more weight is given to the visible reflectance than to the near-infrared reflectance at the surface, while the reverse is found at the top of the atmosphere.

Table 5.7 *Narrow- to broadband albedo conversion constants*

Parameter	Surface broadband albedo		Planetary broadband albedo	
	Valiente et al. (1995)	Stroeve et al. (1997)	Li and Leighton (1992)	Wydick et al. (1987)
$a_1$	0.545	0.655	0.389	0.347
$a_2$	0.320	0.216	0.452	0.650
$a_3$	0.035	4.123	4.530	0.746

For surface albedo computation, the two mentioned studies have reported different coefficients, which probably suggests that the constants could be site-specific. Both the Valiente and Stroeve algorithms have been applied on the current image, and the summary of the statistics of the resulting surface broadband albedo values is shown in Table 5.8. The Table indicates that the Stroeve algorithm tends to give higher values than the Valiente, but in general, both algorithms seem to yield lower albedo values than is expected (some doubts being casted to the assumptions involved while doing atmospheric correction). It appears that there is still difficulty in obtaining accurate broadband surface albedo from NOAA AVHRR reflectance.

Table 5.8 *A summary of the statistics of the resulting surface broadband albedo values computed using different algorithms*

Parameter	Valiente et al. (1995)	Stroeve et al. (1997)
Mean (%)	12.58	15.85
Median (%)	12.87	15.62

*Extension of instantaneous- to daily albedo*

The daily albedo ( $\alpha_0$ ) is usually computed as the arithmetic mean of the instantaneous albedo values covering a span of daytime, i.e. from sunrise to sunset, but only one instantaneous value is obtained from AVHRR image. *Larson and Barkstrom (1977)* suggest that if the instantaneous albedo value is known at any one point in time, then

it can be extrapolated to any other time during that day as a function of solar zenith angle.

$$\alpha_{inst} = 2.444\alpha'_{inst} (1 - \cos\theta_z) \ln\left(1 + \frac{1}{\cos\theta_z}\right) \quad [-] \quad (5.24)$$

Where,  $\alpha'_{inst}$  is the reference albedo. The solar zenith angle data is available in AVHRR channel 8.  $\alpha'_{inst}$  can be computed from  $\alpha_{inst}$  obtained using AVHRR, and it remains constant during the day. However, the following two points should be heeded:

(i) It seems more convincing to compute  $\alpha_0$  as a weighted mean of the instantaneous albedo values, rather than an arithmetic mean. The weights must be derived from the incoming solar radiation. However, there is still a problem of obtaining proper value of incoming solar radiation at each instant, mainly because the transmittance is changing each time. *Chen and Ohring (1984)* argue that for a clear sky day, if the transmittance at any one point in time is determined, then it can be extrapolated to any other time during that day as a function of solar zenith angle. However, field measured transmittance data reveal that during the average conditions of May, the problem of intermittent clouds is so significant that the change in transmittance can not be explained by only solar zenith angle variation (Fig. 5.10).

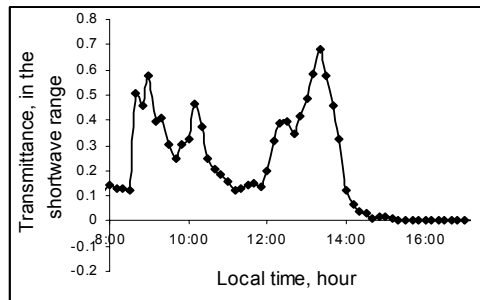


Fig. 5.10 Daytime variation of transmittance, for average condition of May.

(ii) Eq. (5.24) assumes that the relative change in the instantaneous albedo values within a day is a function of only solar zenith angle. However, it is known that the effects of diffuse- and direct sky radiation on instantaneous albedo are quite different. In other words, Eq. (5.24) should be improved to encompass the cloudiness condition of the sky. What about the effect of land cover? It is evident from directional reflectance model theories that different types of surface cover are not equally affected by the change in solar zenith angle.

#### Land surface temperature ( $T_0$ )

Since NOAA-AVHRR acquires data in two spectral bands within the thermal infrared window region, the split-window correction technique can be used to determine surface temperature. This technique corrects for atmospheric effects based on the differential absorption properties of water vapor in two spectral bands (*Becker and Li, 1995*). Most split-window algorithms give the surface temperature,  $T_0$ , as a linear

combination of the brightness temperatures measured in channels 4 and 5, i.e.  $T_4$  and  $T_5$ :

$$T_o = A_0 + A_1T_4 + A_2T_5 \quad [\text{K}] \quad (5.25)$$

Where  $A_0$ ,  $A_1$ , and  $A_2$  are local coefficients which depend on the atmosphere state and spectral emissivities of the surface (Vazquez *et al.*, 1997). Since the local coefficients are not available for the study area, reported local coefficients have been consulted. Table 5.9 summarizes some of the relevant split-window algorithms. Intercomparison of the different algorithms may be one of the possible indications of the relative value of these algorithms. The algorithms listed in Table 5.9 are applied to the last dekadal image of May 1995, and the summary of the statistics of the resulting surface temperature values is given in Table 5.10.

Table 5.9 Summary of Split-Window Algorithms

Reference(s)	Algorithms
Price (1984)	$T_o = [T_4 + 3.33(T_4 - T_5)] \left[ \frac{5.5 - \epsilon_4}{4.5} \right] + 0.75T_5(\epsilon_4 - \epsilon_5)$
Ulivieri and Cannizzaro (1985)	$T_o = T_4 + 3(T_4 - T_5) + 51.57 - 52.45\epsilon$
Vidal (1991)	$T_o = T_4 + 2.78(T_4 - T_5) + 50 \frac{1 - \epsilon}{\epsilon} - 300 \frac{\epsilon_4 - \epsilon_5}{\epsilon}$
Prata and Platt (1991)	$T_o = 3.45 \frac{T_4 - 273.15}{\epsilon_4} - 2.45 \frac{T_5 - 273.15}{\epsilon_5} + 40 \frac{1 - \epsilon_4}{\epsilon_4} + 273.15$
Sobrino <i>et al.</i> (1993)	$T_o = T_4 + 1.06(T_4 - T_5) + 0.46(T_4 - T_5)^2 + 53(1 - \epsilon_4) - 53(\epsilon_4 - \epsilon_5)$
Ulivieri <i>et al.</i> (1994)	$T_o = T_4 + 1.8(T_4 - T_5) + 48(1 - \epsilon) - 75(\epsilon_4 - \epsilon_5)$
Coll <i>et al.</i> (1994)	$T_o = T_4 + 2.13(T_4 - T_5) + 0.18 + 50(1 - \epsilon_4) - 200(\epsilon_4 - \epsilon_5)$
Malik (1998)	$T_o = \frac{1}{\epsilon^{0.25}} (T_4 + 1.5(T_4 - T_5) + 1)$
Caselles <i>et al.</i> (1998)	$T_o = T_4 + 2.25(T_4 - T_5) + 0.9 + 40(1 - \epsilon) - 120(\epsilon_4 - \epsilon_5)$
$\epsilon_4 = 1.619\epsilon - 0.608$ , $\epsilon_5 = 1.467\epsilon - 0.458$ (for vegetation) (Source:- Coll <i>et al.</i> , 1994)	

The results of the intercomparison indicate that:

- (i) The difference between some algorithms can reach up to 6.5 K, therefore indiscriminate use of the algorithms is not advocated;
- (ii) P, V, PP, and S algorithms give higher but comparable results (within 1 K, on an average), U, and M give lower but comparable results (within 1 K), UC, C1 and C2 give systematic overestimation of about 4 K with respect to UC.

*Table 5.10 Summary of statistics of surface temperature, computed using various split window algorithms*

Method	Abbrev.	Mean (K)	Median (K)
Price (1984)	P	307.2	308.5
Ulivieri et al. (1985)	UC	304.2	305.5
Vidal (1991)	V	306.7	308.2
Prata and Platt (1991)	PP	306.2	307.3
Sobrino et al. (1993)	S	306.9	307.8
Coll et al. (1994)	C1	304.6	305.6
Ulivieri et al. (1994)	U	300.7	301.8
Malik (1998)	M	301.7	302.6
Caselles et al. (1998)	C2	304.1	304.4

## 6.

### Conclusions and Recommendations

#### 6.1 Conclusions

The main objective of this study, as stated in Chapter 1, is to test a methodology to determine regional scale crop coefficients analytically using remote sensing. By using field-validated Priestley-Taylor equation for  $ET_c$  and  $ET_{ref}$ , this study has come up with  $K_c$  equations both on instantaneous and daily temporal scales. To execute the  $K_c$  equations, remote sensing data and limited ground-based data are required. The comprehensive analysis of this study demonstrates that satellite data, which have suitable spatial resolution, in combination with limited ground-based data can be utilized to determine regional scale crop coefficients analytically without the prior knowledge of crop type and stage of growth.

#### ***$K_c$ Equations***

- The derived  $K_c$  equations, on instantaneous and daily temporal scales are stated in Eqs. (4.18) and (4.22), respectively;
- To execute the  $K_c$  equations, the required input data must be collected from irrigated areas which satisfy the following two conditions: (i) irrigated areas must be large enough to minimize the effect of advection, and (ii) irrigated areas must bear crops which are not suffering from water-deficit;
- To calculate instantaneous  $K_c$ , the required ground data are: atmospheric shortwave transmittance, air temperature at screen height, and surface temperature;
- To calculate  $K_c$  on a daily scale, the necessity of ground data is reduced to a minimum: only atmospheric shortwave transmittance is required.

#### ***Application of $K_c$ Equations to satellite data***

##### *(a) LANDSAT-TM data*

- For small scale irrigated areas, like that of the study area, the spatial resolution of LANDSAT-TM data is suitable; however, its temporal frequency and the cost associated in procuring the data might be prohibitive;
- Analysis of a single LANDSAT-TM data shows that  $K_c$ , on an instantaneous time scale, can be written as a first order function of surface albedo and surface temperature.

##### *(b) NOAA-AVHRR data*

- High temporal resolution coupled with low cost of data acquisition make the NOAA-AVHRR data operationally applicable for the calculation of  $K_c$  over large scale irrigated areas. However, for small scale irrigated areas, like that of the study area, the spatial resolution of NOAA-AVHRR is not sufficient for the calculation of  $K_c$ . The reason is mainly attributed to the significant proportion of heterogeneous nonirrigated areas within the pixel size of NOAA-AVHRR;

- The adequacy of NOAA-AVHRR to calculate  $K_c$  is determined by the proportion of irrigated areas within the pixel size of NOAA-AVHRR. To determine the proportion of nonirrigated areas within the pixelsize of NOAA-AVHRR, this study suggests the following two step-procedure: (i) the blowing up of the pixel size of LANDSAT-TM to that of NOAA-AVHRR at nadir, and (ii) the calculation of off-nadir angle using Eq. (5.22).

## **6.2 Recommendations**

For the first time, this study has tested the methodology of analytically determining  $K_c$  from remote sensing by using suitable mathematical expressions for  $ET_c$  and  $ET_{ref}$ . As stated in Section (6.1), the method described makes it possible to calculate  $K_c$  from remote sensing, as given in this study. However, since this study has been carried out with a limited data set under a particular set of environmental conditions, further study is necessary to extend this approach to broader set of environmental conditions.

## References

- Ahern, F.J., D.G. Goodenough, S.C. Jain, V.R. Rao and G. Rochon 1977. "Use of clear lakes as standard reflectors for atmospheric measurements." Proc. 11<sup>th</sup> Int. Symp. on *Rem. Sens. of Env.*, 731-755.
- Allen, R.G., M. Smith, W.O. Pruitt and L.S. Pereira 1996b. "Modifications of the FAO crop coefficient approach." In: C.R. Camp, E.J. Sadler and R.E. Yoder (Ed.), *Evapotranspiration and Irrigation Scheduling* (Proc. of the International Conference November 1996), *ASAE*, 124-132.
- Allen, R.G., W.O. Pruitt, J.A. Businger, L.J. Fritschen, M.E. Jensen and F.H. Quinn 1996a. "Evaporation and Transpiration." Chapt. 4. In: *Hydrology Handbook*, *ASCE*, **28**, 125-252.
- Allen, R.G., W.O. Pruitt, J.A. Businger, L.J. Fritschen, M.E. Jensen and F.H. Quinn 1996b. "Evaporation and Transpiration." Chapt. 4. In: *Hydrology Handbook*, *ASCE*, **28**, 125-252.
- Arai, K. 1992. "A supervised Thematic Mapper classification with a purification of training samples." *Int. J. Rem. Sens.*, **13**(11), 2039-2049.
- Ashfaque, A. 1999. "Estimating Lake evaporation using meteodata & remote sensing: A case study of Lake Naivasha, Central Rift Valley, Kenya." M.Sc. thesis, International Institute for Aerospace Survey and Earth Sciences (ITC).
- Bakker, W.H., G.N. Parodi and W.J. Timmermans 1997. "NOAA AVHRR preprocessing: an application of a cloud-detection technique." *ITC Journal*, **1**, 64-73.
- Bastiaanssen, W.G.M. 1995. "Regionalization of surface flux densities and moisture indicators in composite terrain." PhD thesis, Agricultural University of Wageningen, The Netherlands, pp. 273.
- Bastiaanssen, W.G.M. 1998. "Remote sensing in water resources management: The state of the art." International Water Management Institute, Colombo, Sri Lanka, pp. 118.
- Bastiaanssen, W.G.M. and R.A. Roebeling 1993. "Analysis of land surface exchange processes in two agricultural regions in Spain using Thematic Mapper simulator data." In: Bolle, Feddes and Kalma (Ed.), *Exchange processes at the land surface for a range of space and time scales*, *IAHS Publ.*, **212**, 407-416.
- Bausch, W.C. 1995. "Remote sensing of crop coefficients for improving the irrigation scheduling of corn." *Agri. Water Manag.*, **27**, 55-68.
- Bausch, W.C. and C.M.U. Neale 1987. "Crop coefficients derived from reflected canopy radiation: A concept." *Transactions, ASAE*, **30**(3), 703-709.
- Becker, F. and Z.L. Li 1995. "Surface temperature and emissivity at various scales: Definition, Measurement and related problems." *Rem. Sens. Reviews*, **12**, 225-253.
- Blyth, E.M. and A.J. Dolman 1995. "The roughness length for heat of sparse vegetation." *J. of Applied Met.*, **34**, 583-585.
- Boardman, J.W. 1993. "Automated spectral unmixing of AVIRIS data using convex geometry concepts." In: *Summaries, Fourth JPL airborne Geoscience workshop, JPL publication 93-26*, **1**, 11-14.
- Bos, M.G., J. Vos and R.A. Feddes 1996. "CRIWAR 2. A simulation model on crop irrigation water requirements." *ILRI Publ.*, **46**, pp.117.
- Brunt, D. 1932. "Notes on radiation in the atmosphere." *Q.J.R. Meteorol. Soc.*, **58**, 389-420.
- Brutsaert, W. 1975. "On a derivable formula for long-wave radiation from clear skies." *Water Resour. Res.*, **11**, 742-744.
- Brutsaert, W. 1982. "Evaporation into the atmosphere." Reidel, Dordrecht, pp. 299.
- Carlson, T.N. and D.A. Ripley 1997. "On the relation between NDVI, fractional vegetation cover and Leaf area index." *Rem. Sens. Environ.*, **62**, 241-252.
- Caselles, V. and J. Delegido 1987. "A simple model to estimate the daily value of the regional maximum evapotranspiration from satellite temperature and albedo images." *Int. J. Rem. Sens.*, **8**(8), 1151-1162.

- Caselles, V., M.M. Artigao, E. Hurtado, C. Coll and A. Brasa 1998. "Mapping actual evapotranspiration by combining LANDSAT TM and NOAA-AVHRR images: Application to the Barrax Area, Albacete, Spain." *Rem. Sens. Environ.*, **63**, 1-10.
- Chen, T. and G. Ohring 1984. "On the relationship between clear-sky planetary and surface albedos." *J. of The Atmos. Sci.*, **41** (1).
- Chiew, F.H.S., N.N. Kamaladasa, H.M. Malano and T.A. McMahon 1995. "Penman-Monteith, FAO-24 reference crop evapotranspiration and class-A pan data in Australia." *Agri. Water Manag.*, **28**, 9-21.
- Choudhury, B.J. 1989. "Estimating evaporation and carbon assimilation using infrared temperature data: vistas in modeling." In: G.Asrar (Ed.), *Theory and applications of optical remote sensing*, John Wiley, New York, 628-690.
- Choudhury, B.J. 1991. "Multispectral satellite data in the context of land surface heat balance." *Reviews of Geophysics*, **29**, 217-236.
- Choudhury, B.J. 1994. "Synergism of multispectral satellite observations for estimating regional land surface evaporation." *Reviews of Geophysics*, 264-274.
- Clothier, B.E., K.L. Clawson, P.J. Pinter, M.S. Moran, R.J. Reginato and R.D. Jackson 1986. "Estimation of soil heat flux from net radiation during growth of alfalfa." *Agri. and Forest Met.*, **37**, 319-329.
- Coll, C., V. Caselles, J.A. Sobrino and E. Valor 1994. "On the atmospheric dependence of the split-window equation for land surface temperature." *Int. J. Rem. Sens.*, **15**, 105-122.
- De Bruin, H.A.R. 1983. "Evaporation in humid tropical regions." In: *Hydrology of humid tropical regions with particular reference to hydrological effects of agriculture and forestry practice (Proc. of Hamburg Symposium August 1983)*, IAHS Publ., **140**, 299-311.
- De Bruin, H.A.R. 1987. "From Penman to Makkink." In: J.C. Hooghart (Ed.), *Evaporation and Weather Proceedings and information No. 39*. Comm. Hydrological Research TNO, The Hague, 5-30.
- Derrien, M., B. Farki, L. Harang, H. LeGleau, A. Noyalet, D. Pochic and A. Sairourni 1993. "Automatic cloud detection applied to NOAA-11/AVHRR imagery." *Rem. Sens. of Env.*, **46**, 246-267.
- Dingman, S.L. 1994. "Physical Hydrology." Prentice-Hall, Inc., Simon & Schuster / A Viacom Company, New Jersey, pp. 575.
- Doorenbos, J. and A.H. Kassam 1986. "Yield response to water." *FAO Irrigation and Drainage paper*, FAO, Rome, **33**, pp. 193.
- Doorenbos, J. and W.O. Pruitt 1977. "Guidelines for predicting crop water requirements." *FAO Irrigation and Drainage Paper*, FAO, Rome, **24**, pp. 144.
- Duffie, J.A. and W.A. Beckman 1991. "Solar Engineering of Thermal Processes." A Wiley-Interscience Publication, John Wiley & Sons, pp. 917.
- Faizoun, C.A., A. Podaire and G. Dedieu 1994. "Monitoring of sahelian aerosol and atmospheric water vapor content characteristics from sunphotometer measurements." *J. of Applied Meteo.*, **33**, 1291-1303.
- Farah, H.O. and W.G.M. Bastiaanssen 1998. "Spatial variations of surface parameters and evaporation in the Lake Naivasha Basin estimated from remote sensing measurements without ground data." In Press.
- Fung, T. and E. LeDrew 1988. "The determination of optimal threshold levels for change detection using various accuracy indices." *Photogr. Eng. and Rem. Sens.*, **54**(10), 1449-1454.
- Garrat, J.R. 1978. "Transfer characteristics for a heterogeneous surface of large aerodynamic roughness." *Q.J.R. Meteorol. Soc.*, **104**, 491-502.
- Goward, S.N., B. Markham, D.G. Dye, W. Dulanut and J. Yang 1991. "Normalized difference vegetation index measurements from the advanced very high resolution radiometer." *Rem. Sens. of Env.*, **35**, 257-277.

- Gutman, C.G. 1990. "Review of the workshop on the use of satellite-derived vegetation indices on weather and climate prediction models." *Bull. Am. Meteor. Soc.*, **71**(10), 1458-1463.
- Gutman, C.G. 1991. "Vegetation indices from AVHRR: An update and future prospects." *NOAA/NESDIS/ERA*, **12**, 121-135.
- Hargreaves, G.L., G.H. Hargreaves and J.P. Riley 1985. "Irrigation water requirement for Senegal river basin." *ASCE*, **111**, 265-275.
- Hatfield, J.L. 1988. "Large scale evapotranspiration from remotely sensed surface temperature." Proc. On planning, now for irrigation and drainage IR Div/ASCE, Lincoln, NE, July 18-21, 502-509.
- Hatfield, J.L., R.J. Reginato and S.B. Idso 1983. "Comparison of long-wave radiation calculation methods over the United States." *Water Resour. Res.*, **19**, 285-288.
- Heilman, J.L., W.E. Heilman and D.G. Moore 1982. "Evaluating the crop coefficient using spectral reflectance." *Agronomy Journal*, **74**, 967-971.
- Hla, A.K., E.C. Martin, P. Waller and D.C. Slack 1996. "Heat unit-based crop coefficients for grapefruit trees." In: C.R. Camp, E.J. Sadler and R.E. Yoder (Ed.), *Evapotranspiration and Irrigation Scheduling* (Proc. of the International Conference November 1996), *ASAE*, 429-434.
- Holben, B.N. 1986. "Characteristics of maximum-value composite images from temporal AVHRR data." *Int. J. Rem. Sens.*, **7**(11), 1417-1434.
- Idso, S.B. 1983. "On calculating thermal radiation from cloudless skies." *Arch. Met. Geoph. Biocl., Ser. B*, **32**, 53-57.
- Idso, S.B. and R.D. Jackson 1969. "Thermal radiation from the atmosphere." *J. Geophys. Res.*, **74**, 5379-5403.
- Iqbal, M. 1983. "An introduction to solar radiation." Academic Press, Toronto, pp. 390.
- Jackson, R.D., J.L. Hatfield, R.J. Reginato, R.J. Idso and P.J. Pinter 1983. "Estimation of daily evapotranspiration from one time-of-day measurements." *Agri. Water Manag.*, **7**, 351-362.
- Jackson, R.D., M.S. Moran, L.W. Gay and L.H. Raymond 1987. "Evaluating evaporation from field crops using airborne radiometry and ground-based meteorological data." *Irrig. Sci.*, **8**, 81-90.
- Jackson, R.D., S.B. Idso, R.J. Reginato and P.J. Pinter 1980. "Remotely sensed crop temperatures and reflectances as inputs to irrigation scheduling." In: Proceedings: *ASCE*, Irrigation and Drainage division, Specialty Conference, Boise, Idaho New York, 390-397.
- Jacobsen, A. and B.U. Hansen 1999. "Estimation of the soil heat flux/net radiation ratio based on spectral vegetation indexes in high-latitude Arctic areas." *Int. J. Rem. Sens.*, **20**, 2, 445-461.
- Jacovides, C.P. and H. Kontoyianais 1995. "Statistical procedures for the evaluation of evapotranspiration computing models." *Agri. Water Manag.*, **27**, 365-371.
- Jensen, M.E. 1968. "Water consumption of agricultural plants." *Water deficits and plant growth*, Academic press, New York, **2**, 1-22.
- Kim, C.P. and D. Entekhabi 1997. "Examination of two methods for estimating regional evaporation using a coupled mixed layer and land surface model." *Water Resour. Res.*, **33**, 2109-2116.
- Koshiek, W., H.A.R. De Bruin, H. The and B. Van den Hurk 1993. "Estimation of the sensible heat flux of a semi-arid area using surface radiative temperature measurements." *Boundary Layer Meteorol.*, **63**, 213-230.
- Kustas, W.P. and C.S.T. Daughtry 1990. "Estimation of the soil heat flux/net radiation from spectral data." *Agri. and Forest Met.*, **49**, 205-223.
- Kustas, W.P. and J.M. Norman 1996. "Use of remote sensing for evapotranspiration monitoring over land surfaces." *IAHS Publ.*, **41**(4), 495-511.
- Larson, J.C. and B.R. Barkstrom 1977. "Effects of realistic angular reflection laws for the earth's surface upon calculations of the earth-atmosphere albedo." Proc. Symp. On radiation in the atmosphere, 19-23 August 1976, Science Press, Princeton, New York, 451-453.
- Li, Z. and H.G. Leighton 1992. "Narrowband to broadband conversion with spatially autocorrelated reflectance measurements." *J. of Applied Meteorol.*, **31**, 421-431.

- Llasat, M.C. and R.L. Synder 1998. "Data error on net radiation and evapotranspiration estimation." *Agri. and Forest Met.*, **91**, 209-221.
- Malik, Z.H. 1998. "NOAA-measurements for identifying agro-ecological zones in the province of Sindh, Pakistanm (A remote sensing approach)." M.Sc. Thesis, International Institute for Aerospace Survey and Earth Sciences (ITC), pp. 44.
- Markham, B.L. and J.L. Barker 1987. "Thematic Mapper bandpass solar exoatmospherical irradiances." *Int. J. Rem. Sens.*, **8**(3), 517-523.
- Meijerink, A.M.J., H.A.M. De Brouwer, C.M. Mannaerts and C.R. Valenzuela 1994. "Introduction to the use of Geographic Information Systems for practical hydrology." ITC, The Netherlands, pp. 243.
- Molina, M.D.M. 1996. "A method to calculate evapotranspiration considering soil temperature." In: C.R. Camp, E.J. Sadler and R.E. Yoder (Ed.), *Evapotranspiration and Irrigation Scheduling (Proc. of the International Conference November 1996)*, *ASAE*, 402-406.
- Moore, D.S. 1997. "The active practice of statistics: a textbook for multimedia learning." W.H. Freeman and Company, NY, pp. 432.
- Moran, M.S. 1990. "A satellite-based approach for evaluation of the spatial distribution of evapotranspiration from agricultural lands." PhD thesis, Univ. of Arizona, Tucson (Diss. Abstr.).
- Moran, M.S. and R.D. Jackson 1991. "Assessing the spatial distribution of evapotranspiration using remotely sensed inputs." *J. Environ. Qual.*, **20**, 725:737.
- Neale, C.M.U., R.H. Ahmed, M.S. Moran, P.J. Pinter, J. Qi and T.R. Clarke 1996. "Estimating seasonal cotton evapotranspiration using canopy reflectance." In: C.R. Camp, E.J. Sadler and R.E. Yoder (Ed.), *Evapotranspiration and Irrigation Scheduling (Proc. of the International Conference November 1996)*, *ASAE*, pp. 173-181.
- Neale, C.M.U., W.C. Bausch and D.F. Heermann 1989. "Development of reflectance-based crop coefficients for corn." *Transactions, ASAE*, **32**(6), 1891-1899.
- Paltridge, G.W. and R.M. Mitchell 1990. "Atmospheric and viewing angle correction of vegetation indices and grassland fuel moisture content derived from NOAA/AVHRR." *Rem. Sens. Environ.*, **31**, 121-135.
- Penman, H.L. 1948. "Natural evapo-transpiration from open water, bare soil and grass." *Proc. Royal Soc. of London*, **193**, 120-145.
- Pereira, L.S. A. Perrier, R.G. Allen and I. Alves 1996. "Evapotranspiration: Review of concepts and future trends." In: C.R. Camp, E.J. Sadler and R.E. Yoder (Ed.), *Evapotranspiration and Irrigation Scheduling (Proc. of the International Conference November 1996)*, *ASAE*, pp. 109-115.
- Peters, S.W.M. 1995. "Energy- and Water balance modelling of a semi-arid area using remote sensing." PhD. Thesis, Free University of Amsterdam, pp. 256.
- Phulpin, T., J.P. Jullien and D. Lasselin 1989. "AVHRR data processing to study the surface canopies in temperate regions." *Int. J. Rem. Sens.*, **10**(4and 5), 869-884.
- Prata, A.J. and C.M.R. Platt 1991. "Land surface temperature measurements from the AVHRR." *Proc. of the 5<sup>th</sup> AVHRR data users meeting in Tomso, Norway, June 25-28, Eutmestat report EUM P09*, 433-438.
- Price, J.C. 1984. "Land surface temperature from the split window channels of the NOAA-7 advanced very high resolution radiometer." *J. Geophys. Res.*, **89**, 7231-7237.
- Priestley, C.H.B. and R.J. Taylor 1972. "On the assessment of surface heat flux and evaporation using large scale parameters." *Mon. Wea. Rev.*, **100**, 81-92.
- Rahman, H 1996. "Atmospheric optical depth and water vapour effects on the angular characteristics of surface reflectance in NOAA AVHRR." *Int. J. Rem. Sens.*, **17**(15), 2981-2999.
- Reginato, R., R. D. Jackson and P. Pinter 1985. "Evapotranspiration calculated from multispectral and ground station meteorological data." *Rem. Sens. Environ.*, **18**, 75-89.
- Saunders, R.W. 1986. "An automated scheme for the removal of cloud contamination from AVHRR radiances over western Europe." *IJRS*, **7**(7), 867-886.

- Saunders, R.W. and K.T. Kriebel 1988. "An improved method for detecting clear sky and cloudy radiances from AVHRR data." *IJRS*, **9**(1), 123-150.
- Saxton, K.E. and McGuinness 1982. "Evapotranspiration." Chapt. 6. In: C.T. Haan, H.P. Johnson and D.L. Brakensiek (Ed.), Hydrologic modelling of small watersheds, *ASAE*, 229-276.
- Shuttleworth, W.J. 1993. "Evaporation." Chapt. 4. In: Maidment (Ed.), Handbook of Hyrdrology, McGraw-Hill Inc., New York, NY.
- Shuttleworth, W.J., R.J. Gurney, A.Y. Hsu and J.P. Ormsby 1989. "FIFE: The variation in energy partition at surface flux sites." *IAHS Publ.*, **186**, 67-74.
- Slack, D.C., E.C. Martin, A.E. Sheta, F. Fox, L.J. Clark and R.O. Ashley 1996. "Crop coefficients normalized for climatic variability with Growing-Degree-Days." In: C.R. Camp, E.J. Sadler and R.E. Yoder (Ed.), Evapotranspiration and Irrigation Scheduling (Proc. of the International Conference November 1996), *ASAE*, pp. 892-898.
- Slater, P.N. 1980. "Remote sensing; Optics and Optical systems." Addison-Wesley Publ. Comp.
- Smith, M., R.J. Allen and L.Pereira 1996. "Revised FAO methodolgy for crop water requirements." In: C.R. Camp, E.J. Sadler and R.E. Yoder (Ed.), Evapotranspiration and Irrigation Scheduling (Proc. of the International Conference November 1996), *ASAE*, pp. 116-123.
- Sobrino, J.A., V. Caselles and C. Coll 1993. "Theoretical split window algorithms for determining the actual surface temperature." *IL Nuovo Cimento*, **16**(3), 219-236.
- Stewart, J.B. 1996. "Extrapolation of evaporation at time of satellite overpass to daily totals." In: J.B. Stewart, E.T Engman, R.A. Feddes and Y. Kerr (Ed.), *Scaling up in hydrology using remote sensing*, 245-255.
- Stroeve, J., A. Nolin and K. Steffen 1997. "Comparison of AVHRR-derived and in situ surface albedo over the Greenland ice sheet." *Rem. Sens. Environ.*, **62**, 262-276.
- Sugita, M. and W. Brutsaert 1993. "Cloud effect in the estimation of instantaneous downward longwave radiation." *Water Resour. Res.*, **29**, 599-605.
- Swinbank, W.C. 1963. "Long-wave radiation from clear skies." *Q.J.R. Meteorol. Soc.*, **89**, 339-348.
- Tanner, C.B. and W.A. Jury 1976. "Estimating evaporation and transpiration from a row crop during incomplete cover." *Agron. J.*, **68**, 239-243.
- Thornthwaite, C.W. 1948. "An approach toward a rational classification of climate." *The Geographical Review*, **38** (1), 55-94.
- Ulivieri, C. and G. Cannizzaro 1985. "Land surface temperature retrievals from satellite measurements." *Acta Astronautica*, **12**(12), 985-997.
- Ulivieri, C., M.M. Castronuovo, R. Francioni and A. Cardillo 1994. "A split window algorithm for estimating land surface temperature from satellites." *Adv. Space Res.*, **14**(3), 59-65.
- Valiente, J.A., M. Nunez and E. Lopez-Baeza 1995. "Narrow-band to broad-band conversion for meteosat visible channel and broad-band albedo using both AVHRR-1 and -2 channels." *Int. J. Rem. Sens.*, **16**(6), 1147-1166.
- Van de Griend, A.D. and M. Owe 1993. "On the relationship between thermal emissivity and the normalized difference vegetation index for natural surfaces." *Int. J. Rem. Sens.*, **14**(6), 1119-1131.
- Vazquez, D.P., F.J. Olmo Reyes and L.A. Arboledas 1997. "A comparative study of algorithms for estimating land surface temperature from AVHRR data." *Rem. Sens. Environ.*, **62**, 215-222.
- Vidal, A. 1991. "Atmospheric and emissivity correction of land surface temperature measured from satellite using ground measurements or satellite data." *Int. J. Rem. Sens.*, **12**(12), 2449-2460.
- Wright, J.L. 1996. "Derivation of alfalfa and grass reference evapotranspiration." In: C.R. Camp, E.J. Sadler and R.E. Yoder (Ed.), Evapotranspiration and Irrigation Scheduling (Proc. of the International Conference November 1996), *ASAE*, pp. 133-140.
- Wyduck , J.E., P.A. Davis and A. Gruber 1987. "Estimation of broadband albedo from operational narrowband satellite measurements." NOAA Technical Report No. *NESDIS 27*, April 1987.

Zhang, L. and R. Lemeur 1995. "Evaluation of daily evapotranspiration estimates from instantaneous measurements." *Agri. and Forest Met.*, **74**, 139-154.

**ANNEX A Statistical Methods used for Assessing Association**

$$E = \frac{\sum d_i^2 - \sum d_i^2}{\sum d_i^2} \quad (\text{Chiew et al., 1995}) \quad [-] \quad (\text{A.1})$$

$$RMSE = \left( \frac{1}{Z} \sum_{i=1}^Z d_i^2 \right)^{1/2} \quad [\text{W m}^{-2}] \quad (\text{A.2})$$

$$MBE = \frac{1}{Z} \sum_{i=1}^Z d_i \quad [\text{W m}^{-2}] \quad (\text{A.3})$$

$$t = \left[ \frac{(Z-1)MBE^2}{RMSE^2 - MBE^2} \right]^{1/2} \quad (\text{Jacovides and Kontoyiannis, 1995}) \quad [-] \quad (\text{A.4})$$

Where, Z is the number of data pairs,  $d_i$  is the difference between the values estimated using two methods, and  $d_i$  is the difference between the mean and the other values calculated by the reference method.

The coefficient of determination ( $R_o^2$ ) is the regression coefficient of the equation that is forced to pass through the origin,  $Y = aX_1$ . Thus, it provides an indication of the closeness of the data points to the line of best fit forced to pass through the origin. Whereas, the efficiency factor (E) gives an indication of the closeness of the data points to the 1:1 line in the X-Y plot. A value of  $R^2$ ,  $R_o^2$ , and E close to unity indicates a high degree of association between the two variables. The RMSE provides information on the short-term performance of a model by allowing a term by term comparison of the actual difference between the predicted value and the measured value, while the MBE provides information on the long-term performance of a model.

Although the above indicators provide generally a reasonable procedure for model comparison, they do not indicate objectively whether model performances are statistically significant. Thus, this analysis involves an additional statistical indicator: the *t*-statistic. The *t*-statistic is especially used here because of its less sensitivity to different types of distributions (Moore, 1997). The smaller the value of *t*, the better the model's performance is. The critical *t* value, *t-critical*, is obtained from standard statistical tables, for a certain level of significance ( $\nabla$ ) and degrees of freedom (Z-1). In order for the model's estimates to be judged statistically significant at the 1- $\nabla$  confidence level, the calculated *t* value must be less than the critical *t* value. The level of significance can vary between 0 and 1, but is usually 0.005 or 0.01 (Jacovides and Kontoyiannis, 1995). In the present study, the level of significance is chosen to be  $\nabla = 0.005$ .

## **Annex B Derivation of a simplified empirical equation for estimating crop potential evapotranspiration**

To simplify crop potential evapotranspiration (ET<sub>c</sub>) equation, the possibility of relating ET<sub>c</sub> to only T<sub>o</sub> and K<sub>↓</sub> has been considered. The first trial was to establish linear regression equations between these parameters, and then these equations were tested on another data set. The resulting values were not acceptable. Hence, another way of approaching this problem is considered in the following way:

*Caselles and Delegido (1987)* related ET<sub>ref</sub> to K<sub>↓</sub> and T<sub>a</sub> in such a form:

$$ET_{ref} = a T_a K_{\downarrow} + b K_{\downarrow} + c \quad [W \text{ m}^{-2}] \text{ (B.1)}$$

A possible extension of this equation for estimating ET<sub>c</sub> has been attempted. In the above equation, the empirical coefficients which express the influence of K<sub>↓</sub> on ET<sub>ref</sub> can be retained in ET<sub>c</sub>, since K<sub>↓</sub> is independent of the type of crop. However, the expression for the influence of T<sub>a</sub> on ET<sub>ref</sub> should be modified when it is applied to ET<sub>c</sub> (because of differences in albedo). Hence, the correction for the effect of T<sub>a</sub> on ET<sub>c</sub> (due to change in albedo) has been incorporated in c. Thus Eq. (B.1) becomes:

$$ET_c = a T_a K_{\downarrow} + b K_{\downarrow} + f(T_a) \quad [W \text{ m}^{-2}] \text{ (B.2)}$$

The formulation for f(T<sub>a</sub>) has been carried out in such a way: the Priestley-Taylor equation for estimating ET<sub>c</sub> reads as a product of Δ/(Δ+γ), which is a first order equation of temperature, and some other variables including temperature itself. This implies that, the effect of temperature on ET<sub>c</sub> may be expressed in an equation which has more than one order. It is assumed that f(T<sub>a</sub>) is a second-order equation:

$$f(T_a) = cT_a^2 + dT_a + e \quad [W \text{ m}^{-2}] \text{ (B.3)}$$

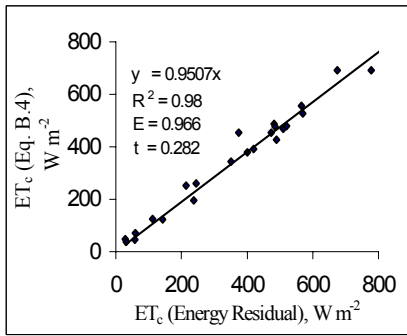
Combining Eqs. (B.2) and (B.3), substituting the air temperature by surface temperature, and introducing new empirical coefficients results in:

$$ET_c = AT_o^2 + BT_oK_{\downarrow} + CT_o + DK_{\downarrow} + E \quad [W \text{ m}^{-2}] \text{ (B.4)}$$

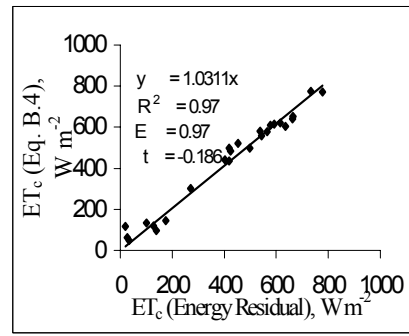
Using the data collected in the chilli field, the corresponding ET<sub>c</sub> values are calculated by means of E-R equation and then these values are used to calibrate the empirical coefficients involved in Eq. (B.4). The resulting coefficients read:

$$A = 0.04, B = -0.0052, C = -8.65, D = 0.882, \text{ and } E = 123.571.$$

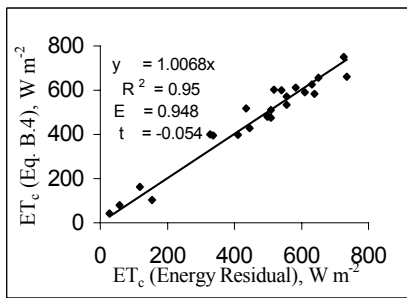
Eq. (B.4), with the above empirical coefficients, has then been applied to squash and bean fields. The obtained results are then compared with those estimates made using E-R equation, as shown in Fig. B.1. The mentioned statistical indicators reveal that there is a very good agreement between the two estimates.



(a) Squash



(b) Bean



(c) Chilli

Fig. B.1 Comparison of instantaneous  $ET_c$  estimates made by Energy Residual equation and Eq. (B.4) over (a) Squash, (b) Bean, and (c) Chilli fields. The value of  $t$ -critical in all plots is about 2.8.

## ANNEX C Testing Transmittance Models

The reliable transmittance data, which are used to test the applicability of different models, are calculated using the following equation:

$$\tau'_{sw} = \frac{K_{\downarrow}}{K_{\downarrow}^{TOA}} \quad [-] \quad (C.1)$$

Data on  $K_{\downarrow}$  are taken from the measurements performed at Ndabibi, while the corresponding  $K_{\downarrow}^{TOA}$  are calculated using Eq. (E.8).

*The Hottel's model.* This model is well described by *Duffie and Beckman* (1991). The atmospheric transmittance is given in the form:

$$\tau'_{sw} = a_0 + a_1 \exp(-k / \cos \theta_z) \quad [-] \quad (C.2)$$

For tropical climate, the constants  $a_0, a_1$ , and  $k$  are given as:

$$a_0 = 0.4025 - 0.0078(6 - A)^2 \quad [-] \quad (C.3)$$

$$a_1 = 0.4954 + 0.0058(6.5 - A)^2 \quad [-] \quad (C.4)$$

$$k = 0.2765 + 0.0190(2.5 - A)^2 \quad [-] \quad (C.5)$$

Where, A is the altitude in km.

For the period covered by the Ndabibi data set, the atmospheric transmittance values are modelled using Eq. (C.2) through Eq. (C.5), and compared with the calculated ones from Eq. (C.1), as shown in Fig. C.1a. This figure shows that there is no good agreement between the measured and calculated transmittance values.

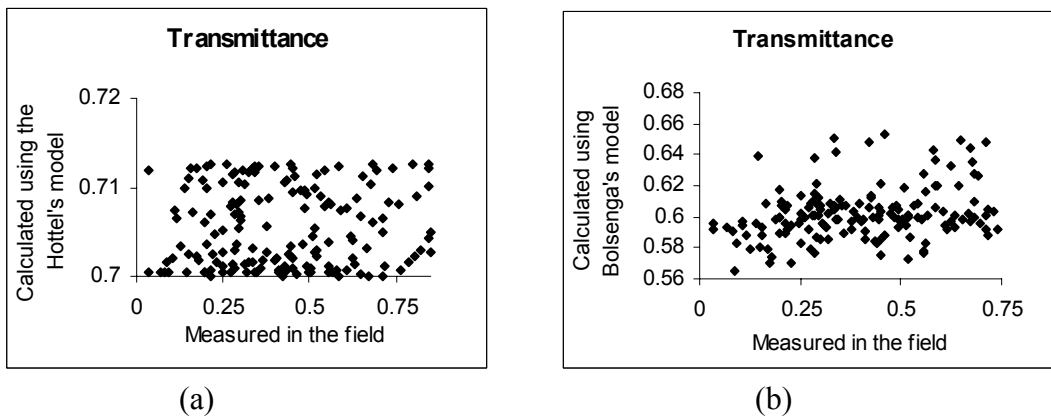


Fig. C.1 Comparison of transmittance values calculated from Eq. (C.1) and modelled using (a) Hottel's model, and (b) Bolsenga's model.

The *Bolsenga's model*. This model is well described by *Dingman* (1994). For clear sky conditions, the atmospheric transmittance is estimated as:

$$\tau'_{sw} = \tau_{sa} - \gamma_{dust} \quad [-] \quad (C.6)$$

Where,  $\tau_{sa}$  is the transmittance due to scattering and absorption by water vapor and the constant atmospheric gases, and  $\gamma_{dust}$  is the attenuation due to dust. The following empirical equations are used to estimate  $\tau_{sa}$ :

$$\tau_{sa} = \exp(a_{sa} + b_{sa} M_{opt}) \quad [-] \quad (C.7)$$

$$a_{sa} = -0.124 - 0.0207W_p \quad [\text{cm}] \quad (C.8)$$

$$b_{sa} = -0.0682 - 0.0248W_p \quad [\text{cm}] \quad (C.9)$$

$$W_p = 1.12 \exp(0.0641T_d) \quad [\text{cm}] \quad (C.10)$$

$$T_d = \frac{\ln(e_a) - 1.810}{0.0805 - 0.00421 \ln(e_a)} \quad [^{\circ}\text{C}] \quad (C.11)$$

Where  $T_d$  is the surface dew point,  $W_p$  is the precipitable water content, and  $M_{opt}$  is the optical air mass.  $M_{opt}$  can be found as a function of latitude and declination from the figure provided by *Dingman* (1994).  $\gamma_{dust}$  values for remote stations are suggested to be from 0.0 to 0.05. Using Eq. (C.7) through Eq. (C.11), transmittance values are modelled, and compared with the calculated ones from Eq. (C.1). Fig. C.1b depicts the result of the comparison. As can be seen from this figure, the *Bolsenga's model* is not suitable to model transmittance properly. One reason for the failure of the *Hottel's* and *Bolsenga's* models to yield reasonable estimates of transmittance can be ascribed to the unpredictable nature of water vapor and aerosols. Thus, few parameters like zenith angle and air temperature data alone can not explain the differences in transmittance.

## ANNEX D Derivation of an empirical equation for estimating daily net longwave radiation ( $L_{n24}$ )

$L_{n24}$  can be represented by the following radiation law:

$$L_{n24} = -f\varepsilon'\sigma(T_a)^4 \quad [\text{W m}^{-2} \text{ day}^{-1}] \quad (\text{D.1})$$

Where  $f$  = adjustment for cloud cover, and  $\varepsilon'$  is the net emissivity between the atmosphere and the ground.

The net emissivity ( $\varepsilon'$ ) can be estimated from *Brunt* (1932):

$$\varepsilon' = a_e + b_e \sqrt{e_d} \quad [\text{k Pa}] \quad (\text{D.2})$$

Where  $a_e$  and  $b_e$  are correlation coefficients, and  $e_d$  is the actual vapor pressure. *Doorenbos and Pruitt* (1977) suggested the following values for average conditions:

$$a_e = 0.34 \quad \text{and} \quad b_e = -0.14$$

The cloudiness factor ( $f$ ) in Eq. (D.1) can be estimated using solar radiation data from

$$f = a_c \frac{K_{\downarrow 24}}{K_{\downarrow 24o}} + b_c \quad [-] \quad (\text{D.3})$$

Where  $a_c$  and  $b_c$  are longwave radiation coefficients for clear skies (sum=1), and  $K_{\downarrow 24o}$  is the solar radiation for clear skies with  $n/N=1$ .

*Doorenbos and Pruitt* (1977) recommended the following values for  $a_c$  and  $b_c$ : For arid areas,  $a_c = 1.35$ , and  $b_c = -0.35$ ; for humid areas,  $a_c = 1.00$ , and  $b_c = 0.00$ .

Since the study area lies between the two climatological conditions, average values of  $a_c$  and  $b_c$  have been taken, i.e.,  $a_c = 1.175$ , and  $b_c = -0.175$ .

$f$  can further be written as (*Shuttleworth*, 1993):

$$f = \left( a_c \frac{b_s}{a_s + b_s} \right) \frac{n}{N} + \left( b_c + \frac{a_s}{a_s + b_s} a_c \right) \quad [-] \quad (\text{D.4})$$

Where  $n$  is bright sunshine hours per day,  $N$  is total day length,  $a_s$  is fraction of extraterrestrial radiation on overcast days ( $n = 0$ ), and  $a_s + b_s$  is fraction of extraterrestrial radiation on clear days. The following values are recommended for Kenya,  $a_s = 0.24$  and  $b_s = 0.59$  (*Doorenbos and Pruitt*, 1977).

For  $a_c = 1.175$ ,  $b_c = -0.175$ ,  $a_s = 0.24$ , and  $b_s = 0.59$ , Eq. (D.4) reduces to:

$$f = 0.165 + 0.835n/N \quad [-] \quad (\text{D.5})$$

## ANNEX E Extraterrestrial Solar Radiation

The formulations required to solve extraterrestrial solar radiation ( $K_{\downarrow}^{TOA}$ ), which are taken from *Iqbal* (1983) and *Duffie and Beckman* (1991), are given in this section.

*Day angle ( $\Gamma$ )*

$$\Gamma = 2\pi(d_n - 1)/365 \quad [\text{rad}] \quad (\text{E.1})$$

Where,  $d_n$  is the day number of the year, ranging from 1 on 1 January to 365 on 31 December.

*Eccentricity correction factor ( $E_0$ )*

$$E_0 = 1.000110 + 0.034221 \cos\Gamma + 0.001280 \sin\Gamma \\ + 0.000719 \cos 2\Gamma + 0.000077 \sin 2\Gamma \quad [-] \quad (\text{E.2})$$

*Solar declination ( $\delta$ )*

$$\delta = (0.006918 - 0.399912 \cos 2\Gamma + 0.070257 \sin\Gamma \\ - 0.006758 \cos 2\Gamma + 0.000907 \sin 2\Gamma \\ - 0.002697 \cos 3\Gamma + 0.00148 \sin 3\Gamma)(180/\pi) \quad [\text{deg}] \quad (\text{E.3})$$

*Equation of time ( $E_t$ )*

$$E_t = (0.000075 + 0.001868 \cos\Gamma - 0.032077 \sin\Gamma \\ - 0.014615 \cos 2\Gamma - 0.04089 \sin 2\Gamma)(229.18) \quad [\text{min}] \quad (\text{E.4})$$

*Solar time*

$$\text{Solar time} = 4(L_{\text{st}} - L_{\text{loc}}) + E_t + \text{standard time} \quad [\text{min}] \quad (\text{E.5})$$

Where,  $L_{\text{st}}$  and  $L_{\text{loc}}$  are the standard- and the observer's longitudes.

*Solar zenith angle ( $\theta_z$ )*

$$\cos \theta_z = \sin \delta \sin \phi + \cos \delta \cos \phi \cos \omega \quad [-] \quad (\text{E.6})$$

Where,  $\omega$  is the hour angle, and  $\phi$  is the geographic latitude.

*The hour angle,  $\omega$ .* It is the angular displacement of the sun east or west of the local meridian due to rotation of the earth on its axis at  $15^\circ$  per hour, morning negative, afternoon positive.

*Sunrise hour angle ( $\omega_s$ )*

$$\omega_s = \cos^{-1}(-\tan \phi \tan \delta) \quad [\text{deg}] \quad (\text{E.7})$$

Extraterrestrial solar radiation on an Instantaneous time scale

$$K_{\downarrow}^{TOA} = I_{sc} E_0 (\sin \delta \sin \phi + \cos \delta \cos \phi \cos \omega) \quad [\text{W m}^{-2}] \quad (\text{E.8})$$

Where,  $I_{sc}$  is the solar constant ( $I_{sc} = 1367 \text{ W m}^{-2}$ , with an uncertainty of the order of 1%).

Extraterrestrial solar radiation on a daily time scale

$$K_{\downarrow 24}^{TOA} = (24/\pi) I_{sc} E_0 \sin \phi \sin \delta [(\pi/180)\omega_s - \tan \omega_s] \quad [\text{W m}^{-2}] \quad (\text{E.9})$$

Or

$$K_{\downarrow 24}^{TOA} = (24/\pi) I_{sc} E_0 \cos \phi \cos \delta [\sin \omega_s - (\pi/180)\omega_s \cos \omega_s] \quad [\text{W m}^{-2}] \quad (\text{E.10})$$

Extraterrestrial solar radiation on a daily time scale on a monthly mean daily time scale

The monthly mean daily extraterrestrial radiation can be calculated with Eq. (E.9) using  $\delta$  for the mean day of the month given in Table E.1. The calculated  $K_{\downarrow 24}^{TOA}$  values, for the study area, are shown in Table E.2.

Table E.1 Recommended average days for months and values of  $J$  by months (Adapted from Duffie and Beckman (1991))

Month	$d_n$ for ith Day of month	For the average Day of the Month		
		Date	$d_n$ , Day of year	$\delta$ , declination
January	i	17	17	-20.9
February	31 + i	16	47	-13.0
March	59 + i	16	75	-2.4
April	90 + i	15	105	9.4
May	120 + i	15	135	18.8
June	151 + i	11	162	23.1
July	181 + i	17	198	21.2
August	212 + i	16	228	13.5
September	243 + i	15	258	2.2
October	273 + i	15	288	-9.6
November	304 + i	14	318	-18.9
December	334 + i	10	344	-23.0

Table E.2 Monthly average daily extraterrestrial radiation,  $\text{W m}^{-2}$

Jan	Feb	Mar	Apr	May	Jun	Jul	Aug	Sep	Oct	Nov	Dec
362	374	378	367	348	335	340	357	372	373	363	357

## ANNEX F LANDSAT-TM Image Preprocessing

### F.1 Characteristics of the LANDSAT system

LANDSAT-5 carries both the Multispectral Scanner Systems (MSS) and the Thematic Mapper (TM) sensors; however, routine collection of MSS data was terminated in late 1992. The LANDSAT-5 platform operates from a sun-synchronous, near-polar orbit, imaging the same 185 km ground swath every 16 days. A LANDSAT-5 TM scene has an instantaneous field of view (IFOV) of 30 m by 30 m in bands 1 through 5 and band 7, and an IFOV of 120 m by 120 m on the ground in band 6. The TM sensor has 7 bands, of which the wavelength range is from the visible, through the mid-IR, into the thermal-IR portion of the electromagnetic spectrum.

Table F.1 LANDSAT 5 characteristics

Spacecraft	LANDSAT-5, operational since March 1, 1984
Orbit	Approximately 705 km, sun-synchronous
Equatorial crossing time	0945 LST southbound
Scan rate	420 lines per minute
Data	8 bit binary
Sensor	TM

### F.2 Radiometric correction

Radiometric correction deals with the conversion of raw digital numbers to radiance values.

Individual TM channels are characterized by linear radiometric response function, which can be written as:

$$L_{\lambda(i)} = B + G(DN) \quad [\text{mW cm}^{-2} \text{ Sr}^{-1}] \quad (\text{F.1})$$

B = Minimum radiance

G = (Maximum radiance / 254) – (Minimum radiance / 255)

Where  $L_{\lambda(i)}$  is the in-band spectral radiance value at the top of the atmosphere, B is the Bias, and G is the Gain.

The Bias and the Gain values are calculated using the maximum and minimum radiance values, which are given in the header format of each TM image. For the current image, the radiance values are given in Table F.2.

Table F.2 Radiance values in  $\text{mW cm}^{-2} \text{ Sr}^{-1}$  (for date 21 January, 1995)

Band	Maximum radiance	Minimum radiance
1	1.059	-0.017
2	2.612	-0.042
3	1.640	-0.026
4	2.950	-0.059
5	0.684	-0.017
6	1.524	0.124
7	0.425	-0.009

The in-band spectral radiance value at the top of the atmosphere in unit of  $\text{mW cm}^{-2} \text{Sr}^{-1} \text{micron}^{-1}$  can be calculated from the following equation:

$$L_{\lambda_i} = \frac{L_{\lambda(i)}}{\beta} \quad [\text{mW cm}^{-2} \text{Sr}^{-1} \text{micron}^{-1}] \quad (\text{F.2})$$

Where  $\beta$  is the detector band width. The band widths of the TM detectors are also available in the header format of each TM image. For the current image, the values are shown in Table F.3.

Table F.3 Bandwidths in micron

Band 1	Band 2	Band 3	Band 4	Band 5	Band 6	Band 7
0.066	0.082	0.067	0.128	0.217	1.0	0.252

### F.3 Atmospheric correction, Visible and Infrared

*Computation of broadband surface albedo ( $\alpha_{inst}$ )*

*Step 1:* Computation of the incoming in-band spectral radiance values at the top of the atmosphere ( $K_{\lambda_i}$ ).  $K_{\lambda_i}$  is given by:

$$K_{\lambda_i} = \frac{E_0 E_{sun} \lambda_i \cos \theta_z}{\pi} \quad [\text{mW cm}^{-2} \text{Sr}^{-1}] \quad (\text{F.3})$$

Where  $E_{sun} \lambda_i$  is the incoming in-band spectral radiance at the top of the atmosphere at mean sun-earth distance,  $\theta_z$  is the solar zenith angle, and  $E_0$  is the eccentricity correction factor. The equations required to solve the state variables involved in Eq. (F.3) are fully described in Annex E.

For TM bands, the following values of  $E_{sun} \lambda_i$  have been given by *Markham and Barker* (1987):

Table F.4  $E_{sun} \lambda_i$  values in  $\text{mW cm}^{-2} \text{Sr}^{-1}$

Band 1	Band 2	Band 3	Band 4	Band 5	Band 7
195.8	182.8	155.9	104.5	21.9	7.5

*Step 2:* Computation of broadband planetary reflectance at the top of the atmosphere ( $r_p$ ).

The spectral planetary reflectance at the top of the atmosphere,  $r_{p\lambda_i}$ , can be written as:

$$r_{p\lambda_i} = \frac{L_{\lambda_i}}{K_{\lambda_i}} \quad [-] \quad (\text{F.4})$$

$r_p$  is, therefore, formulated as:

$$r_p = \sum W_i r_{p\lambda_i} \quad [-] \quad (\text{F.5})$$

The weights,  $W_i$ 's, are assigned as per the relative proportion of  $E_{sun\lambda_i}$ . The calculated weights for each band are shown in Table J.5.

Table F.5 Weights of TM bands as per  $E_{sun\lambda_i}$

Band 1	Band 2	Band 3	Band 4	Band 5	Band 7
0.293	0.274	0.233	0.156	0.033	0.011

*Step 3:* The conversion of broadband planetary reflectance at the top of the atmosphere to broadband surface reflectance.

The computation of broadband surface albedo ( $\alpha_{inst}$ ) from the corresponding planetary reflectance at the top of the atmosphere requires the removal of the effect of the atmosphere. When data on atmospheric optical depth on the day and time of satellite overpass is not available, simple atmospheric correction procedures can be used. Two atmospheric correction methods have been considered here.

*The Knowledge-based method.* In this method, surface albedos of known surfaces are taken from literatures, and compared with the corresponding planetary albedos. The chosen surface types and their albedos are shown in Table F.6.

Table F.6 Albedos of known surfaces

Surface type	Surface albedo from literature	Planetary albedo from image
Lake	0.06	0.03
Cyprus	0.14	0.06

A linear relation is assumed between the surface and planetary albedos in such a form:

$$\alpha_{inst} = ar_p + b \quad [-] \text{ (F.6)}$$

Substitution of the tabulated values in the above equation yields the following values for a and b,

$$a = 2.67, \quad b = -0.02$$

$$\Rightarrow \alpha_{inst} = 2.67r_p - 0.02 \quad [-] \text{ (F.7)}$$

*The Ahern's method.* The form suggested by Ahern *et al.* (1977), which makes use of the darkest object present in the scene, is given in Eq. (5.4). For  $\tau_{sw}'' = 0.35$ , and  $r_{pmin} = 0.01$ , it yields the following expression for  $\alpha_{inst}$ :

$$\alpha_{inst} = 2.86r_p - 0.03 \quad [-] \text{ (F.8)}$$

Comparison of Eqs. (F.7) and (F.8) shows that both equations yield approximately closer results, especially within the  $r_p$  range of 0.03 to 0.06. Eq. (F.8) has been used for further analysis.

## ANNEX G NOAA-AVHRR Image Preprocessing

### G.1 Characteristics of the NOAA System

The NOAA series satellites were designed to operate in a near-polar, sun-synchronous orbit. Germane to this discussion is the NOAA-14 mission, which remains operational to date. The satellite system contains AVHRR (Advanced Very High Resolution Radiometer). Table G.1 lists the basic characteristics of the mission and the AVHRR instrument. NOAA receives AVHRR data at full resolution and archives them in two different forms. Selected data are recorded at full resolution, referred to as local area coverage (LAC) data. All of the data are sampled down to a nominal resolution of 4 km, referred to as global area coverage (GAC) data.

Table G.1 NOAA-14 Characteristics

Spacecraft	NOAA-14, operational since December 30, 1994
Orbits per day	14.1
Period of orbit (min)	102
Afternoon pass	1340 LST ascending node, 0140 LST descending node
IFOV, at nadir (km)	1.1
Scan angle from nadir (deg)	$\pm 55.4$
AVHRR spectral channels ( $\mu\text{m}$ )	
1	0.58 – 0.68
2	0.725 – 1.10
3	3.55 – 3.93
4	10.3 – 11.3
5	11.5 – 12.5

### G.2 AVHRR Data

The AVHRR data set is made up of 5-channel, 10-bit, raw AVHRR data from each daily afternoon pass of NOAA. The 10-days composite image, one of the available AVHRR products, includes the following bands or channels:

Table G.2 AVHRR data description

Band	Description	Band	Description
1	AVHRR channel 1	6	NDVI
2	AVHRR channel 2	7	Satellite zenith
3	AVHRR channel 3	8	Solar zenith
4	AVHRR channel 4	9	Relative azimuth
5	AVHRR channel 5	10	Data index

Since the data in the channels are scaled, the following describes the method for unscaling the data:

$$Actual = \frac{(Scaled - offset)}{scale} - shift \quad (G.1)$$

Table G.3 Parameters required for unscaling AVHRR data

Channel	Units	Offset	Scale	Shift	Channel	Units	Offset	Scale	Shift
1	%	10	10	0	6	-	10	1	0
2	%	10	10	0	7	degrees	10	1	90
3	Kelvin	10	5.602	-160	8	degrees	10	1	0
4	Kelvin	10	5.602	-160	9	degrees	10	1	180
5	Kelvin	10	5.602	-160					

The 10-days composite image is produced using the maximum NDVI compositing method. The NDVI is examined pixel by pixel for each observation during 10 days to determine the maximum value. The retention of the highest NDVI values minimizes cloud contamination, reduces directional reflectance and off-nadir viewing effects, minimizes sun-angle and shadow effects, and minimizes aerosol and water vapor effects (*Holben, 1986*).

Currently, the data set can be downloaded from the following websites, free of costs:

- (i) <http://edcwww.cr.usgs.gov/landdac/1KM/comp10d.html>
- (ii) <http://shark1.esrin.esa.it/>

### G.3 Cloud Detection

Clouds are, obviously, an obstacle to sensing the surface features. Therefore, cloudy and cloud-free pixels must be carefully distinguished. Dealing with a 10-day maximum value composite alleviates the problem of cloud contamination to some extent; however, to totally mask cloudy pixels, cloud screening algorithms should be used. Various cloud detection algorithms have already been developed for NOAA-AVHRR data, and can be divided into three main categories (*Bakker et al., 1997*): statistical methods (relying on histogram analysis), threshold techniques (applied to each pixel), and pattern recognition methods (based on the analysis of large-scale texture). In light of a relatively fast (semi-) automatic cloud-detection algorithms, most widely used cloud detection methods use threshold techniques. The Saunders algorithm (After *Saunders, 1986*) is the prominent among threshold techniques. This algorithm is used here, but only after some modifications as discussed in the following section. The Saunders algorithm is based on five cloud detection tests (Fig. G.1). Only if all tests are negative is a pixel identified as cloud-free. The last dekadal image of May 1995 is presented here as a case study.

#### *Gross cloud check*

This test uses the brightness temperature threshold for channel 5. In contrast to channel 4, the channel 5 brightness temperature is more suitable to detect clouds because clouds have a greater optical depth at the wavelength range of channel 5. If the channel 5 temperature of a pixel is below a certain threshold, then the pixel is identified as cloud contaminated. How can the threshold be set? *Saunders (1986)* suggests the following procedure. First, the channel 5 image is displayed on the screen and then, cloud-free areas which are likely to be the coldest in the image are selected. The brightness temperatures over the selected areas are then read out and lowered by 2 K to obtain the threshold. Following the same procedure, the threshold for the current image is found out to be 284 K. Every pixel obtaining a channel 5

temperature lower than this threshold is identified as cloud contaminated. The resulting image after this test is depicted in the top left part of Fig. G.2.

### *Spatial coherence test*

This test relies on the assumption that the mean and standard deviation values of brightness temperatures in an array of several pixels can be used to test for the presence of clouds in the box. Unfortunately, this test is not very suitable for use over land areas, especially where there are heterogeneous land management practices, because the variation of brightness temperature, during the afternoon AVHRR passes, can be relatively high. This test is not therefore used in this study.

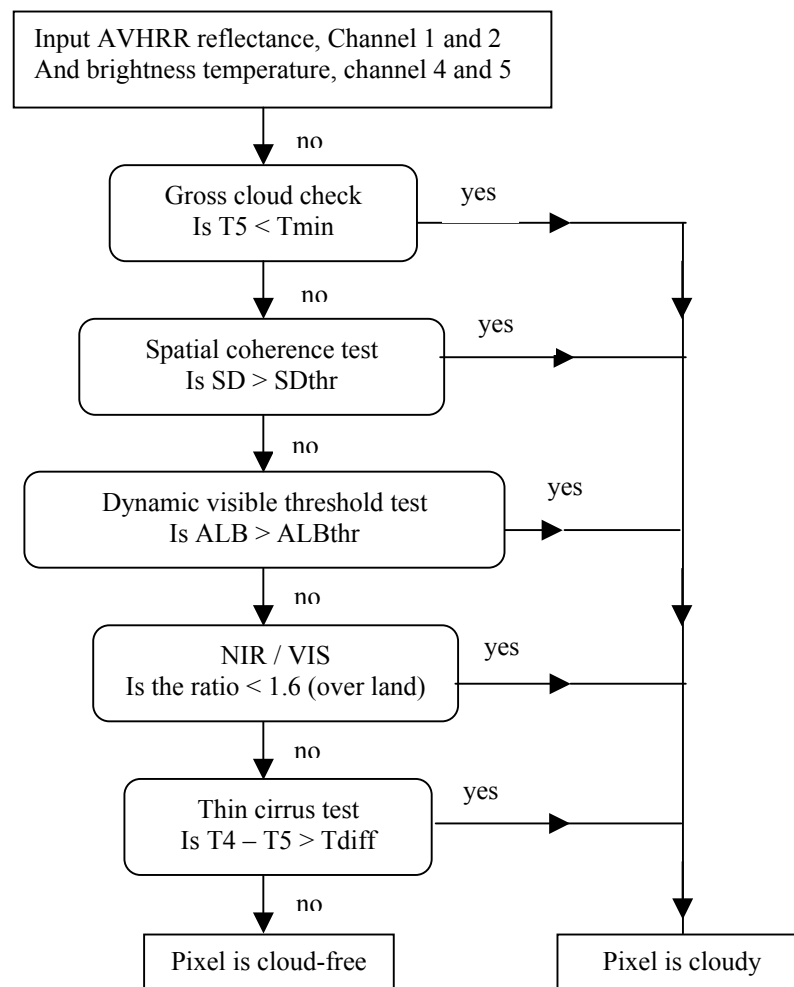


Fig. G.1 The Saunders cloud detection algorithm.

### *Dynamic visible threshold test*

In channel 1, clouds have a higher reflectance than the land surface, a threshold value can therefore be set to discriminate clouds. However, care should be taken here because this technique is not valid for areas of specular reflection, which might occur over water bodies. The threshold is determined dynamically from the histogram of normalized visible radiances (i.e. between 0 and 1) in a two step procedure. First, the

cloud-free modal value is taken from the histogram, and then an offset is added to this value to determine the threshold. After analyzing many histograms of different NOAA-AVHRR images acquired at different times of the year over Europe, *Saunders and Kriebel* (1988) found out that the offset over land surface is 0.017. However, *Derrien et al.* (1993) argue that the offset must be a function of the solar zenith angle, and in any way the threshold value must not exceed 0.20. A threshold value of 0.20 is considered in this study.

#### *NIR / VIS test*

This test makes use of the ratio between near infrared reflectance (NIR) and visible (VIS) reflectance:

$$Q = NIR / VIS \quad [-] \quad (G.2)$$

As the reflectances of clouds are rather similar in both channels, Q is close to unity for cloud contaminated pixels. Over land surfaces under clear sky condition, Q is high. The threshold Q value can be fixed after analyzing the histogram of Q; however, when cloud free modal values are absent, *Saunders and Kriebel* (1988) suggest a threshold value of 1.60 over land surface, and *Gutman* (1990) suggests 1.30. After studying the histogram, a threshold value of 1.4 is selected for the current image.

#### *Thin cirrus test*

The difference, Channel 4 – Channel 5, (*Holben, 1986; Phulpin et al., 1989*) is very useful in screening the pixels contaminated by semi-transparent clouds (thin cirrus clouds). Since clouds have different emissivities at different wavelength ranges, they give different temperatures in channel 5 and channel 4. Over clouds, brightness temperature differences can reach 6 K, while land surfaces under clear sky condition yield much smaller differences (often less than one). The maximum expected difference between channel 5 and channel 4 over land surfaces under clear sky condition is a function of the total amount of water vapor in the atmosphere and the solar zenith angle. After analyzing many different atmospheric and solar zenith angle conditions, *Saunders and Kriebel* (1988) determined the threshold values for various conditions (Table G.4). *Derrien et al.* (1993) also confirmed the values listed in Table G.4.

*Table G.4 Temperature thresholds  $T_{diff}$  (K) for, Channel 4 – Channel 5, cloud Detection test at mid-latitudes (after Saunders and Kriebel, 1988)*

	Sec ( $\theta_z$ ) values				
Channel 4 (K)	1.00	1.25	1.50	1.75	2.00
260	0.55	0.60	0.65	0.90	1.10
270	0.58	0.63	0.81	1.03	1.13
280	1.30	1.61	1.88	2.14	2.30
290	3.06	3.72	3.95	4.27	4.73
300	5.77	6.92	7.00	7.42	8.43
310	9.41	11.22	11.03	11.60	13.39

Using this Table and Channel 8 (Solar zenith angle), in combination with Channel 4, a threshold map is prepared. The resulting image after each and all cloud tests is displayed in Fig. G.2.

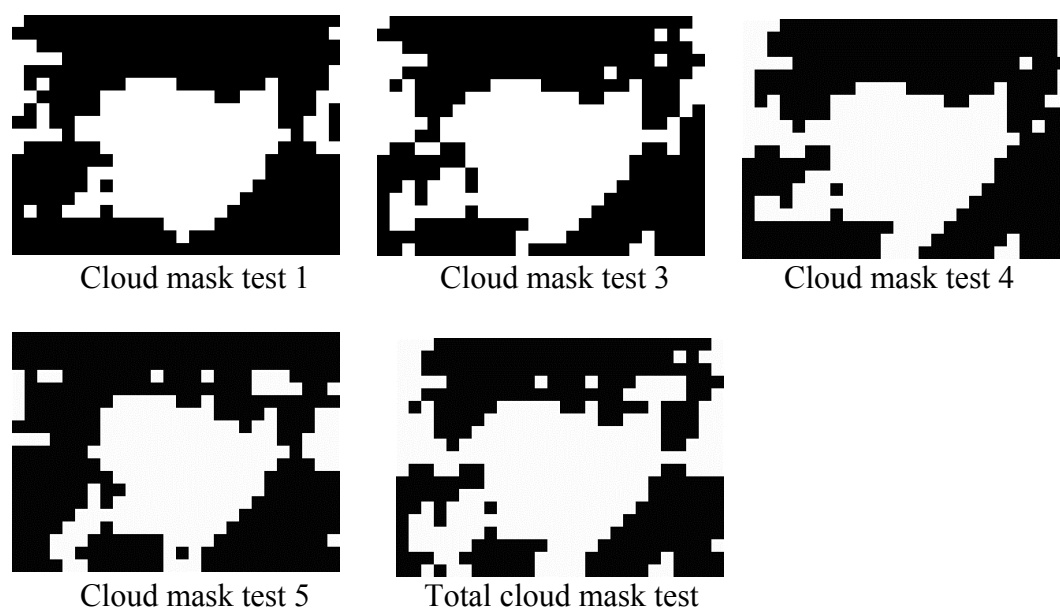


Fig. G.2 Results of the cloud detection scheme applied on the imagery of the last decade of May 1995. The area displayed in white is either lake or cloud masked.

#### G.4 Atmospheric correction, visible and near infrared

##### Background

Atmospheric scattering due to molecules and aerosols, and absorption due to water vapor and ozone are the two main mechanisms principally responsible for the modification in the visible and near-infrared region of the solar spectrum (Rahman, 1996), and their influence depends not only on instantaneous composition of the atmosphere but also on relative position of sun, satellite, and viewed point. The 10-days maximum value compositing technique (Holben, 1986) is believed to take care of most of the atmospheric effects. The available data set is also corrected for ozone and rayleigh scattering by the data set providers. The necessity for further atmospheric correction is dictated not only by the different geometry of observations but also by the varying distribution of water vapor and aerosols. To envisage the effect of viewing angle on the reflectances of channel 1 and 2, one pixel is selected from the image under study, and its corresponding channels 1, 2, and 7 covering a one-year period are acquired. After routine cloud screening procedures, Fig. G.3 displays the cloud screened data, as a function of the satellite zenith angle.

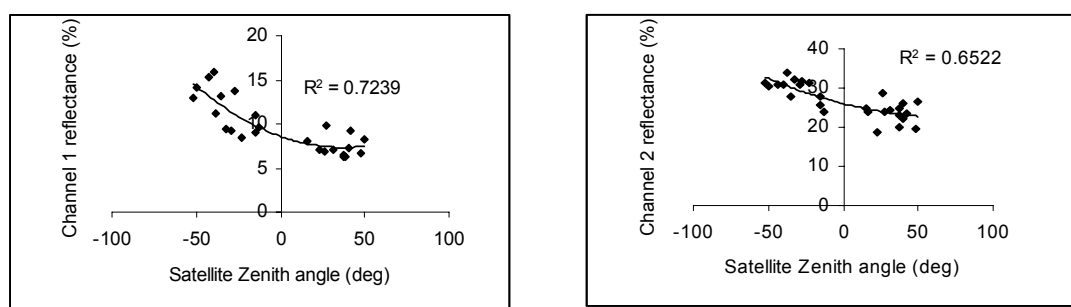


Fig.G.3 Channel 1 and channel 2 reflectances as a function of satellite zenith angle.

## Atmospheric correction

The complex radiative transfer calculations required for evaluation of the atmospheric effects are prohibitive for routine use, and there is still no agreement on a feasible method. The simplified operational model developed by *Paltridge and Mitchell* (1990) is used here. This model uses simplified parameterizations of atmospheric attenuation of reflectances of channels 1 and 2, derived using LOWTRAN-6 atmospheric transmittance code for a U.S. Standard Atmosphere. The angular effects and aerosol scattering are included explicitly. The model has been successfully applied in Australia (*Paltridge and mitchell*, 1990). The formulations used in the model are stated below:

$$R = \frac{k(1-M) - \sec \phi_{\text{view}} \sum_{j=0}^1 \Phi_j Q_j(m)}{4 \cos \theta_z g(m) e^{-m\tau} (1 + m\tau)} \quad [-] \quad (\text{G.2})$$

$$m = \sec \theta_z + \sec \phi_{\text{view}} \quad [-] \quad (\text{G.3})$$

$$\sin \phi_{\text{view}} = \sin \phi_s [1 + H / R] \quad [-] \quad (\text{G.4})$$

$$Q_1(m) = (1 - e^{-m\tau}) g(m) / m \quad [-] \quad (\text{G.5})$$

$$\Theta = \pi - (\theta_z + \phi_{\text{view}}) \quad [\text{deg}] \quad (\text{G.6})$$

$$\Phi_0 = 0.75(1 + \cos^2 \Theta) \quad [-] \quad (\text{G.7})$$

M for channel 1 (i.e., M1) = 0.1, and M2 = 0.05.

Where  $k$  is channel reflectance,  $\theta_z$  is solar zenith angle,  $\phi_{\text{view}}$  is satellite viewing angle,  $\phi_z$  is satellite zenith angle,  $\tau$  is aerosol vertical optical depth,  $\Phi$  is scattering phase function,  $H$  is the satellite altitude ( $\approx 850\text{km}$ ),  $R$  is the radius of the earth ( $\approx 6370\text{km}$ ), and the subscripts 0 and 1 refer to molecular scatter and aerosol scatter respectively.

Table G.5  $Q_1$  as a function of  $\Theta$

$\Theta$	$Q_1$
0	8.030
20	8.495
40	8.162
60	8.062
80	8.027
100	8.015
120	8.010
140	8.012
160	8.024
180	8.037

Table G.6 Functions  $g(m)$  and  $Q_0(m)$

m	Channel 1		Channel 2	
	g	$Q_0$	g	$Q_0$
1	0.229005	0.013709	0.221244	0.004733
2	0.209898	0.013098	0.201840	0.004523
3	0.192496	0.012526	0.187174	0.004348
4	0.176639	0.011989	0.175166	0.004197
5	0.162182	0.011485	0.164829	0.004062
6	0.148993	0.011012	0.155661	0.003939
7	0.136955	0.010567	0.147385	0.003287
8	0.125961	0.010148	0.139832	0.003732
9	0.115915	0.009754	0.132891	0.003623
10	0.106729	0.009383	0.126481	0.003531

Inputs for the model consist of satellite- and sun zenith and azimuth angles, channel reflectances, and aerosol optical depths for channel 1 and 2. The aerosol optical depths are not available for the study area. Had the lake not been masked by the data

set providers, it would have been simple to work out the aerosol optical depth for channel 2 by using the darkest object subtraction method. Because of lack of data on atmospheric turbidity, the aerosol optical depth for channel 1 is assumed to be 0.15, which corresponds to the less turbid days in the Sahelian regions (10 % of the days) (Faizoun *et al.*, 1994). It can also be assumed that the aerosol optical properties are constant with each of the channels, and the ratio between the aerosol optical depths for channel 1 and 2 is constant and equal to 1.36 (Saunders, 1988). Using the mentioned inputs, the atmospheric correction for channels 1 and 2 has been carried out using equations stated in Eqs. (G.2) through (G.7) The mean values of the resulting reflectances for the two channels are tabulated in Table G.7.

*Table G.7 Mean reflectance values before- and after atmospheric correction using the paltridge and mitchell model, in percentages*

	Before atmospheric correction	After atmospheric correction
Channel 1	10.24	10.35
Channel 2	18.63	19.23

## ANNEX H Temporal Variability and Interrelationships between Variables

### H.1 Temporal Variation of Micro-meteorological Variables

Field data collected on October 8, 1998 have been selected to discuss the daytime variation of some variables. Fig H.1 depicts the typical daytime change in the incoming shortwave radiation, windspeed, surface radiant temperature, and the difference between surface radiant and air temperature.

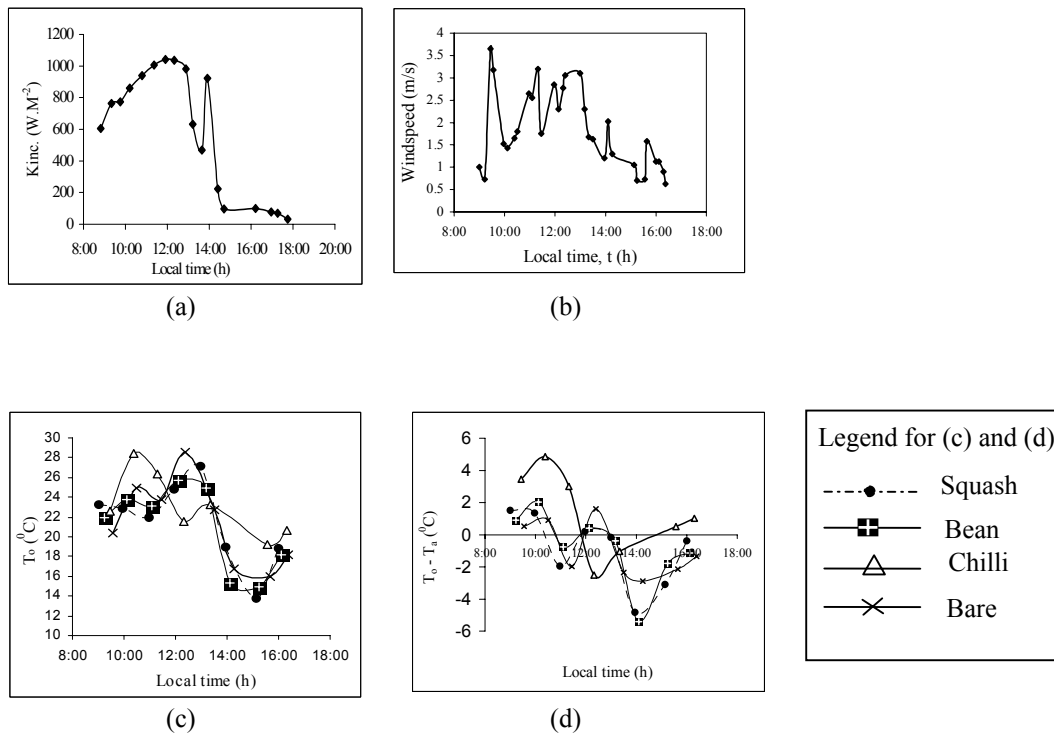


Fig. H.1 Typical daytime variation of (a) incoming shortwave radiation  $K_{\downarrow}$  (Kinc.), (b) windspeed  $u$ , (c) surface radiant temperature  $T_o$ , and (d)  $T_o - T_a$ , measured on October 8, 1998.

Fig. H.1a shows that the incoming shortwave radiation falls rapidly at about 14:00, and since then it becomes low. This pattern reveals the presence of clouds since 14:00, which had been a usual phenomenon during the fieldwork period. The windspeed graph, which is depicted in Fig. H.1b, is shown to have a high amplitude and frequency, and  $\left| \frac{\partial u}{\partial t} \right| \gg 0$ , in most cases. This reflects the highly erratic nature of the windspeed, and consequently the difficulties in extrapolating this variable from instantaneous readings. Fig. H.1c shows that the surface temperatures of the irrigated crops are close to each other and they exhibit the same pattern. However, the surface temperature of the bare soil is higher than that of the crops except at about noontime. At about noontime, a sag curve is observed in the surface temperature of the bare soil that indicates lower temperature even than those of the irrigated crops. The reason for this could be attributed to the sudden presence of clouds during the time the surface temperature over bare soil was measured. Fig. H.1d shows that for most hours of the daytime, the canopy surface temperatures are lower than the respective air temperatures. The difference between the two temperatures is also shown to be a function of the vegetation density (v.d.), the squash field (v.d.= 76%) being cooler

than the chilli field (v.d.=35%). Over the bare field, the air temperature is mostly higher than the surface temperature. Figs. H.1c and H.1d demonstrate that, over the cropped areas,  $T_o-T_a$  is in phase with  $T_o$ . The field data collected in Niger and Egypt (Bastiaanssen, 1995) and Botswana (Peters, 1995) also revealed the same relationship.

## H.2 Soil Moisture Profile

Soil moisture profile measurements were performed by inserting the TDR horizontally. The measurements were conducted for two scenarios. The first scenario refers to an event when there was a little rain prior to measurements, while the second refers to an event when there was no rain shortly before measurements. The first scenario is presented in Table H.1 and Fig. H.2, while the second in Fig. H.3.

Table H.1 Soil moisture profile data ( $\theta_d$ ) for 4 samplepoints in different landcovers. Scenario: there was little rain prior to measurements.

Soil Depth, d (cm)	$\theta_d$ (expressed as percentage of volume) in the fields						Bare
	Squash		Bean		Chilli		
	Crop	Weed	Crop	Soil between crop	Crop	Soil between crop	
5	32.4	36.8	26	23.7	25.7	24.5	34.3
10	31.4	30.3	24.5	20.7	24.3	24.1	33.5
20	28.7	31.7	23.9	18.2	24.0	26.6	34.4
30	30.2	29	28.2	25.9	28.4	30.8	31.6
45	29.6	33.7	32	34.8	24.5	26.6	22.6
60	31.9	33.9	34.2	37.7	24.7	26.1	23.4
100	35.2	51.1	47.7	41.1	28.1	28.3	27.3
120	32.2	32.2	40.8	45.3	29.8	29.5	29.8
140	31.4	34.3					
150							30

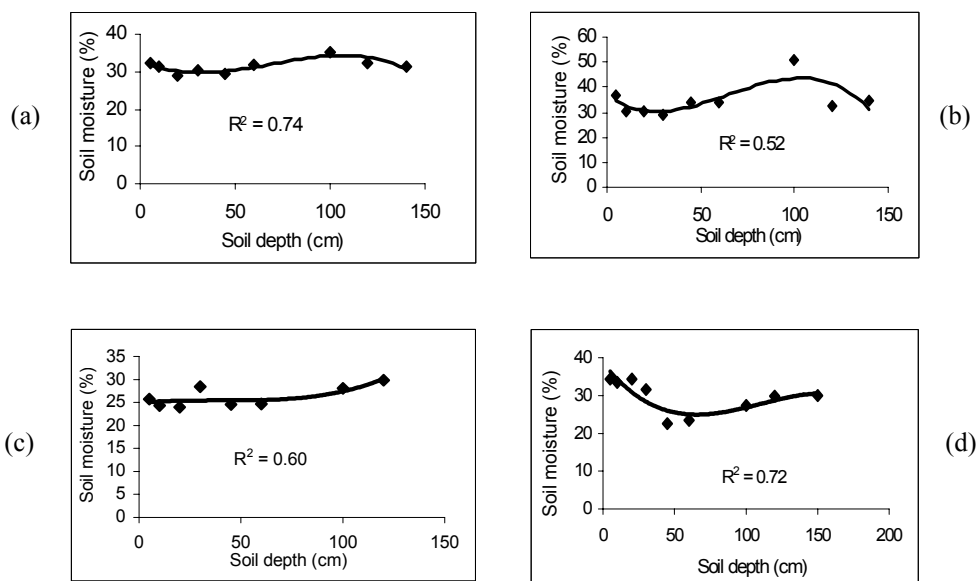


Fig. H.2 Soil moisture profile at (a) Squash, (b) Bean, (c) Chilli, and (d) bare sites after little rain (expressed as percentage of volume).

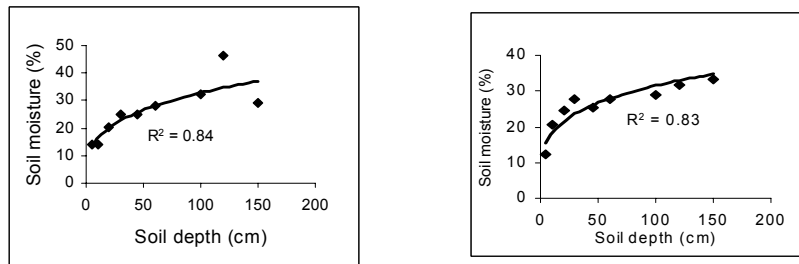


Fig. H.3 Soil moisture profile at (a) Bean, and (b) Chilli sites in the absence of rain (expressed as percentage of volume).

Investigation of Table H.1 and Fig. H.3 reveals the following points.  $\theta_5$  and  $\theta_{10}$  in the squash and bare fields are higher than those in the bean and chilli fields. The reason for this is that dense vegetation & high biotic (microorganisms) activity in the squash field, and recently ploughed soil in the bare field tend to increase the water retention capacity of the soils. In all cases,  $\theta_5 > \theta_{10}$  as it is expected due to the rain. However, the large difference between  $\theta_5$  and  $\theta_{10}$  in the weed area can be explained by the growing of weeds in the furrows (small depressions) between the squash crops. For all the data points, a third order polynomial curve seems to fit well. Two crests and a single dip are typically observed in all the curves. The first crest, which occurs at 5 cm depth, can be explained by the rain that took place a few hours ago before the measurement. Whereas the second crest, which is found at about 100-120 cm, may indicate the presence of a highly porous soil layer at this depth. The dip occurs at about 20 cm for the cropped (weeded) areas and at 45 cm for the bare soil. The former depth can be explained by the root zone while the latter by the ploughing depth.

As shown in Fig. H.3, for the soil moisture profile data obtained in the absence of rain (i.e. the second scenario), a power function seems to fit well. The curve of this function rises rapidly at the beginning and then it goes on gradually. The rapidly rising segment can be explained by the rapid depletion of soil moisture in the first 10cms of the soil profile. The highly porous soil, which was mentioned earlier, can also be seen in the bean field at a depth of 120 cm.

### H.3 Empirical Relationships between Soil Moisture and Land Surface Properties

The interrelationships between soil moisture and land surface parameters are studied using the field data that have been collected over bare soil surface. The bare soil unit has been selected for this purpose in view of the fact that it encompasses a wide range of conditions. The weather condition, during the measurement of the state variables, was partly cloudy.

#### *The $\alpha_{inst} - \theta_d$ relationship*

Although  $R^2$  is low (about 0.4), Fig. H.4a and b depict an inverse relationship between  $\alpha_{inst}$  &  $\theta_1$ , and  $\alpha_{inst}$  &  $\theta_5$ , as expected. The wide scatter around the regression lines can be partly attributed to response differences between  $\alpha_{inst}$  &  $\theta_d$  to instantaneous

changes in atmospheric energy flux. The presence of persistent cloud passing problem in the study area can, therefore, partly explain the wide scatter observed in Fig. H.4. Bastiaanssen (1995) tried to minimize this problem by comparing daily average surface albedo values with surface soil moisture, and he found a better association ( $R^2 = 0.67$ ) between the two state variables.

Fig. H.4c shows that  $\theta_{16}$  is poorly correlated to  $\alpha_{inst}$ , as expected. It is reasoned that evaporation from bare soil occurs over the first few centimeters of soil thickness, and thus, integrated soil moisture over a range of 16cm has a weak influence on variables that are associated with evaporation. The correlation between  $\theta_{16}$  and  $\alpha_{inst}$  is expected to improve over cropped areas, since the soil moisture within 16cm-soil depth is more or less available to evapotranspiration.

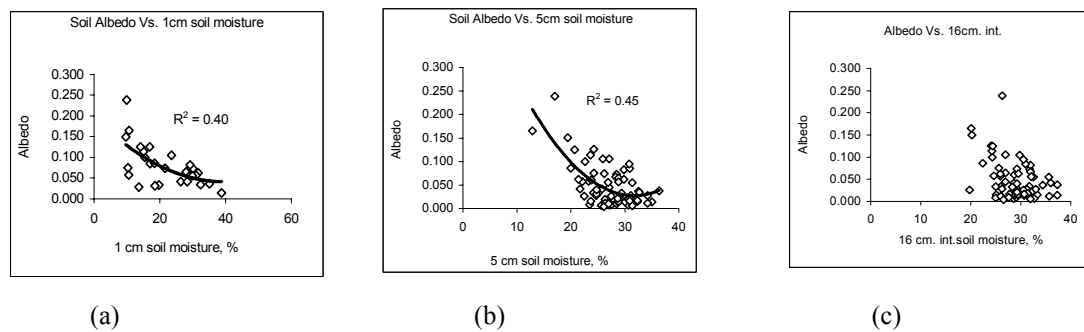


Fig. H.4 Relations between soil surface albedo and soil moisture (expressed as percentage of volume) at (a) 1cm depth, (b) 5cm depth, and (c) integrated 16cm.

The  $\theta_5 - T_o$  relationship

As demonstrated in Fig. H.5 (a), the effect of  $\theta_5$  on  $T_o$  is more entangled. The reason for this is explained by various other factors which affect  $T_o$  besides  $\theta_5$ .  $T_o$  responds more quickly to the atmosphere energy flux change than does  $\theta_5$ . The lack of good correlation between  $T_o$  and  $\theta_5$  has also been shown by Bastiaanssen (1995), who reached at the same conclusion after analyzing the data set collected in the Qattara depression.

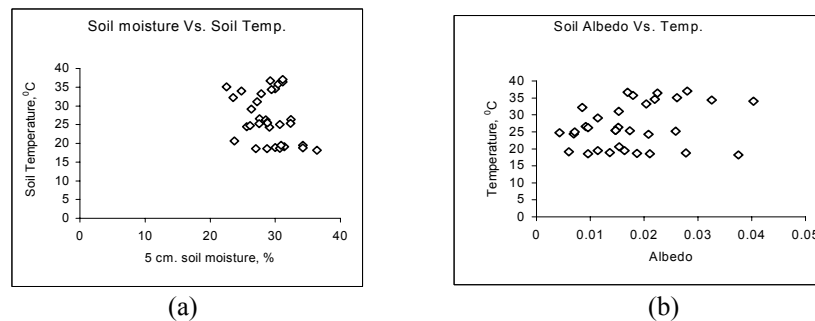


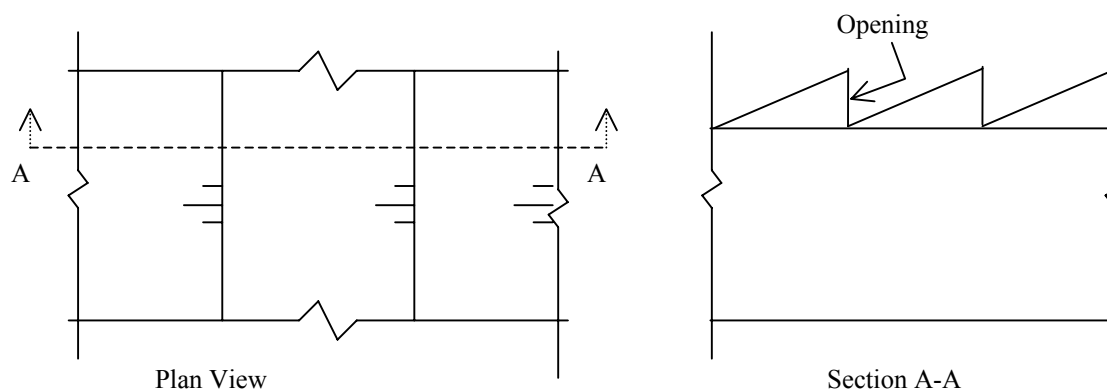
Fig. H.5 Relation between soil infrared temperature and (a) 5cm soil moisture (b) soil surface albedo.

*The  $\alpha_{inst}$  -  $T_o$  relationship*

As shown in Fig. H.5 (b), the plotted  $\alpha_{inst}$  values lie within the range of 0.005 to 0.04. They are so low because of the high moisture content of the soil (due to the heavy rainfall which occurred a day before the measurement took place). It has been observed in the same graph that for the surface albedo values lying within the mentioned ranges, there is no good correlation between  $\alpha_{inst}$  and  $T_o$ . The reason for this can be partly explained by the very low values of  $\alpha_{inst}$  values. If  $\alpha_{inst}$  values, for instance, change from 0.005 to 0.04 (the two extremes used in the graph), the change in net radiation is only 3.5 %, which is too small to cause a significant change in  $T_o$ . In such a case,  $T_o$  is more controlled by some other factors. *Choudhury* (1991) argues that high  $\alpha_{inst}$  values are likely to give a higher correlation than low  $\alpha_{inst}$  values. For  $\alpha_{inst}$  values which cover a wider range, like between 0.10 to 0.35, *Bastiaanssen* (1995) found a third-order polynomial relation between  $T_o$  and  $\alpha_{inst}$ , with  $\frac{\partial T_o}{\partial \alpha_{inst}} = 0$  at  $\alpha_{inst} = 0.24$ .

## ANNEX I Openfield vs. Greenhouse

On 14<sup>th</sup> of October 1998, an intensive field measurement of micro-meteorological variables was conducted simultaneously inside- and outside greenhouse. The greenhouse, where the measurements were performed, is located at  $0^{\circ} 49' 25.97''$  S,  $36^{\circ} 22' 6.92''$  E. The greenhouse setup, and the site characteristics are shown in Fig I.1 and Table I.1.



Note:- Drawings are not to scale.

Fig. I.1 Plan and side views of the greenhouse setup.

Table I.1 Site characteristics

Parameter	Characteristics
<b>Plant parameters</b>	
Type of plant	Rose flower
Variety	Frisw, (yellow in color)
Root depth (cm)	40
Crop height (cm)	150
Canopy width (cm)	130
Distance between plants (cm)	40
LAI	7 - 8
<b>Greenhouse properties</b>	
Roofing type	White Polyethene
Side walls	White Polyethene
Other properties	Air opening is provided
<b>Irrigation practice</b>	
Irrigation type	Drip
Irrigation interval (days)	1
Duty ( $l \cdot sec^{-1} \cdot ha^{-1}$ )	Unknown
Crop yield (# of flowers. $m^{-2} \cdot Yr^{-1}$ )	600

### Analyses of results

It is obvious from Fig. I.2 that the incoming shortwave radiation ( $K_{\downarrow}$ ) inside the greenhouse is about 36 % lower than that of  $K_{\downarrow}$  outside of the greenhouse. This does not necessarily imply that the incoming total radiation inside greenhouse is correspondingly so low. The reason for this is that the reduction in  $K_{\downarrow}$  is counterbalanced by the increment in the incoming longwave radiation ( $L_{\downarrow}$ ). However, the total net radiation inside greenhouse remains so low because of high value  $L_{\uparrow}$ .

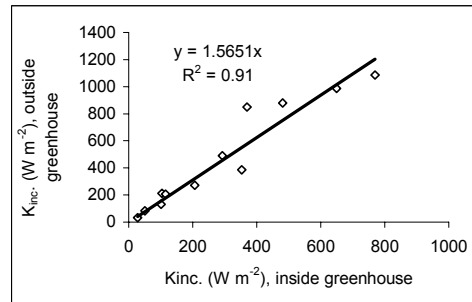


Fig. I.2 Comparison of incoming shortwave radiation inside- and outside greenhouse.

## ANNEX J File Locations

Note: 'NA' refers to 'Not Applicable'

Description	Input Data Location			Output Data Location		
	File Name	Sheet	Column(s)	File Name	Sheet	Column(s)
<b>Table</b>						
2.1	NA	NA	NA	Thesis.doc	NA	NA
2.2	NA	NA	NA	Thesis.doc	NA	NA
2.3	NA	NA	NA	Thesis.doc	NA	NA
3.1	NA	NA	NA	Thesis.doc	NA	NA
3.2	NA	NA	NA	Thesis.doc	NA	NA
3.3	Ndabibi.xls	1	C - E	Thesis.doc	NA	NA
4.1	NA	NA	NA	Thesis.doc	NA	NA
4.2	NA	NA	NA	Thesis.doc	NA	NA
4.3	NA	NA	NA	Thesis.doc	NA	NA
4.4	InstantaneousETC.xls	1	B - L, X, AG	InstantaneousETC.xls	1	BA, BB
	InstantaneousETC.xls	2	B - L, X, AG	InstantaneousETC.xls	2	BA, BB
	InstantaneousETC.xls	3	B - L, X, AG	InstantaneousETC.xls	3	BA, BB
4.5	InstantaneousETC.xls	1	B - L, X, AG	Thesis.doc	NA	NA
	InstantaneousETC.xls	2	B - L, X, AG	Thesis.doc	NA	NA
	InstantaneousETC.xls	3	B - L, X, AG	Thesis.doc	NA	NA
4.6	Ndabibi.xls	1	A - E	Ndabibi.xls	1	Q, U
4.7	InstantaneousETC.xls	1	B - L, X, AG	Thesis.doc	NA	NA
	InstantaneousETC.xls	2	B - L, X, AG	Thesis.doc	NA	NA
	InstantaneousETC.xls	3	B - L, X, AG	Thesis.doc	NA	NA
4.8	NA	NA	NA	Thesis.doc	NA	NA
4.9	Ndabibi.xls	1	C - E, AI - AK	Ndabibi.xls	1	AE-AH, AL
5.1	ILWISdata\lrrmaj.mpr	NA	NA	Thesis.doc	NA	NA
5.2	NA	NA	NA	Thesis.doc	NA	NA
5.3	NA	NA	NA	Thesis.doc	NA	NA
5.4	ILWISdata\albedo.mpr, ILWISdata\surtemp.mpr, ILWISdata\Kcinst.mpr	NA	NA	Thesis.doc	NA	NA
5.5	ILWISdata\kcinstdy.tbt	NA	NA	Thesis.doc	NA	NA
5.6	<a href="http://edcwww.cr.usgs.gov/landdac/1KM/com p10d.html">http://edcwww.cr.usgs.gov/landdac/1KM/com p10d.html</a>	NA	NA	Thesis.doc	NA	NA
5.7	NA	NA	NA	Thesis.doc	NA	NA
5.8	<a href="http://edcwww.cr.usgs.gov/landdac/1KM/com p10d.html">http://edcwww.cr.usgs.gov/landdac/1KM/com p10d.html</a>	NA	NA	Thesis.doc	NA	NA
5.9	NA	NA	NA	Thesis.doc	NA	NA
5.10	<a href="http://edcwww.cr.usgs.gov/landdac/1KM/com p10d.html">http://edcwww.cr.usgs.gov/landdac/1KM/com p10d.html</a>	NA	NA	Thesis.doc	NA	NA
E.1	NA	NA	NA	Thesis.doc	NA	NA
E.2	NA	NA	NA	Thesis.doc	NA	NA
F.1	NA	NA	NA	Thesis.doc	NA	NA
F.2	NA	NA	NA	Thesis.doc	NA	NA
F.3	NA	NA	NA	Thesis.doc	NA	NA
F.4	NA	NA	NA	Thesis.doc	NA	NA
F.5	NA	NA	NA	Thesis.doc	NA	NA

File Locations

Description	Input Data Location			Output Data Location		
	File Name	Sheet	Column(s)	File Name	Sheet	Column(s)
F.6	NA	NA	NA	Thesis.doc	NA	NA
G.1	<a href="http://edcwww.cr.usgs.gov/landdac/1KM/com p10d.html">http://edcwww.cr.usgs.gov/landdac/1KM/com p10d.html</a>	NA	NA	Thesis.doc	NA	NA
G.2	<a href="http://edcwww.cr.usgs.gov/landdac/1KM/com p10d.html">http://edcwww.cr.usgs.gov/landdac/1KM/com p10d.html</a>	NA	NA	Thesis.doc	NA	NA
G.3	<a href="http://edcwww.cr.usgs.gov/landdac/1KM/com p10d.html">http://edcwww.cr.usgs.gov/landdac/1KM/com p10d.html</a>	NA	NA	Thesis.doc	NA	NA
G.4	NA	NA	NA	Thesis.doc	NA	NA
G.5	NA	NA	NA	Thesis.doc	NA	NA
G.6	NA	NA	NA	Thesis.doc	NA	NA
G.7	<a href="http://edcwww.cr.usgs.gov/landdac/1KM/com p10d.html">http://edcwww.cr.usgs.gov/landdac/1KM/com p10d.html</a>	NA	NA	Thesis.doc	NA	NA
H.1	General field data.xls	5	G – I	General field data.xls	5	G – I
I.1	NA	NA	NA	Thesis.doc	NA	NA
<b>Figure</b>						
3.1	NA	NA	NA	Thesis.doc	NA	NA
3.2	CropWat 4 Windows	NA	NA	Thesis.doc	NA	NA
3.3	NA	NA	NA	Thesis.doc	NA	NA
3.4	Ndabibi.xls	1	C, AI, AJ	Ndabibi.xls	Chart 1	NA
3.5	Ndabibi.xls	1	C – E	Thesis.doc	NA	NA
4.1	InstantaneousETC.xls	1	B – L, X, AG	InstantaneousETC.xls	Chart 1	NA
	InstantaneousETC.xls	2	B – L, X, AG	InstantaneousETC.xls	Chart 2	NA
	InstantaneousETC.xls	3	B – L, X, AG	InstantaneousETC.xls	Chart 3	NA
4.2	Instantaneous longwave.xls	1	A – E	Instantaneous longwave.xls	Chart 1	NA
4.3	Atmospheric emissivity.xls	1	A – C	Atmospheric emissivity.xls	Chart 1, 2	NA
4.4a	Ndabibi.xls	1	A – E	Ndabibi.xls	Chart 2	NA
4.4b	Ndabibi.xls	1	A – E	Ndabibi.xls	Chart 3	NA
4.5	Ndabibi.xls	1	C – E, AI – AK	Ndabibi.xls	Charts 4, 5, 6, 7	NA
5.1	ILWISdata\sample.sms	NA	NA	Thesis.doc	NA	NA
5.2	ILWISdata\fcc.mpl	NA	NA	ILWISdata\fcc.mpv	NA	NA
5.3	ILWISdata\**	NA	NA	ILWISdata\irrig.mpv	NA	NA
5.4	ILWISdata\**	NA	NA	ILWISdata\kcinstant.mpv	NA	NA
5.5	ILWISdata\**	NA	NA	ILWISdata\etcinst.mpv	NA	NA
5.6	ILWISdata\**	NA	NA	ILWISdata\kcinstant.his	NA	NA
5.7	Transmittance.xls	1	A – C	Transmittance.xls	Chart 1	NA
5.8	ILWISdata\**	NA	NA	ILWISdata\kcdaily.mpv	NA	NA
5.9	ILWISdata\**	NA	NA	ILWISdata\etcdaily.mpv	NA	NA
5.10	Ndabibi.xls	1	C – E	Ndabibi.xls	Chart 8	NA
B.1	InstantaneousETC.xls	1	B – L, X, AG	InstantaneousETC.xls	Chart 4	NA
	InstantaneousETC.xls	2	B – L, X, AG	InstantaneousETC.xls	Chart 5	NA
	InstantaneousETC.xls	3	B – L, X, AG	InstantaneousETC.xls	Chart 6	NA
C.1	Transmittance modelling.xls	1	A – E	Transmittance modelling.xls	Chart 1	NA
G.1	NA	NA	NA	Thesis.doc	NA	NA

Description	Input Data Location			Output Data Location		
	File Name	Sheet	Column(s)	File Name	Sheet	Column(s)
G.2	<a href="http://edcwww.cr.usgs.gov/landdac/1KM/comp10d.html">http://edcwww.cr.usgs.gov/landdac/1KM/comp10d.html</a>	NA	NA	Thesis.doc	NA	NA
G.3	<a href="http://edcwww.cr.usgs.gov/landdac/1KM/comp10d.html">http://edcwww.cr.usgs.gov/landdac/1KM/comp10d.html</a>	NA	NA	Thesis.doc	NA	NA
H.1	Daytime variation.xls	1	A - T	Daytime variation.xls	Chart 1,2,3,4	NA
H.2	General field data.xls	5	J - I	General field data.xls	Chart 1,2,3,4	NA
H.3	General field data.xls	7	A - C	General field data.xls	Chart 1,2	NA
H.4	Interrelationships between variables.xls	1	A - G	Interrelationships between variables.xls	Chart 1, 2, 3	NA
H.5	Interrelationships between variables.xls	1	A - G	Interrelationships between variables.xls	Chart 4,5	NA
I.1	NA	NA	NA	Thesis.doc	NA	NA
I.2	Greenhouse dataset.xls	1	G - I	Thesis.doc	NA	NA

### Raw Input Data

- Lake Naivasha Vineyard Data Set

FILE NAME = **General Field Data.xls**

Sheets:

Date(s) in Oct. 1998	3-4	5	6	7	8	9	10	12	15	16
Sheet	1	2	3	4	5	6	7	8	9	10

- Greenhouse Data Set

FILE NAME = **Greenhouse dataset.xls**

Sheet: 1

- Ndabibi Data Set

FILE NAME = **Ndabibi.xls**

Sheet: 1

- Internet Data

WEBSITE ADDRESS : <http://edcwww.cr.usgs.gov/landdac/1KM/comp10d.html>

- Meteorological Data

DATABASE: **CropWat 4 Windows**

## **Annex K      Field Data**

This data set is organized and presented in three parts. The first two parts present data collected in the Lake Naivasha Vineyard Farm, while the third inside Greenhouse Farm. The Ndabibi data set is not listed here.

### Part 1: General data

This part consists of all the data collected in the field (except solar radiation data dated from 7 to 10<sup>th</sup> of October, 1998). Part of this data are not used in the analysis mainly because the corresponding solar radiation data were not measured in the field.

### Part 2: Data used in the calculation of crop potential evapotranspiration

This part presents radiation and other meteorological data used to calculate crop potential evapotranspiration, on an instantaneous time scale, as described in Section (4.2).

### Part 3: The Greenhouse Data Set